UNIVERSITY OF CALIFORNIA
RIVERSIDE

A Study of the Morphology Dependence of Singlet Fission in Organic Materials Using Magnetic Field Effects and Time Resolved Photoluminescence

A Dissertation submitted in partial satisfaction
of the requirements for the degree of

Doctor of Philosophy

in

Chemistry

by

Geoffrey Piland

August 2016

Dissertation Committee:

Professor Christopher Bardeen, Chairperson
Professor Yadong Yin
Professor David Bocian

The Dissertation of Geoffrey Piland is approved:

Committee Chairperson

University of California, Riverside

ABSTRACT OF THE DISSERTATION

A Study of the Morphology Dependence of Singlet Fission in Organic Materials Using Magnetic Field Effects and Time Resolved Photoluminescence

by

Geoffrey Piland

Doctor of Philosophy, Graduate Program in Chemistry
University of California, Riverside, August 2016
Professor Christopher Bardeen, Chairperson

To further enhance photovoltaic efficiencies, singlet fission (SF) has been studied as a possible avenue to exceed the Shockley-Quiesser limit which prohibits single junction solar cells from going beyond 34% efficiency. SF occurs in organic materials when an excited singlet exciton within the organic material splits into two triplet excitons. This process, being spin allowed, occurs rapidly and the resultant triplets have the benefits of longer lifetimes (∼ms) and longer diffusion lengths than their singlet counterparts. In order to better utilize this process for applications such as photovoltaics, there must be a better understanding of what systems give rise to high yields of triplets and how to harvest these triplets to do work. This work uses time-resolved fluorescence techniques along with magnetic fields to study how morphology plays a role in the singlet fission process. In order to do this, studies were done on the molecular systems of tetracene, rubrene, and diphenylhexatriene. Expanded versions of the Merrifield kinetic model were created to model the dynamics of these

systems and better understand how spin and triplet-triplet annihilation affect the dynamics of the system. We find that amorphous rubrene has a slower singlet fission lifetime than tetracene at 2 ns. Using our expanded model, diphenylhexatriene was found to have a fission lifetime of 290 ps in the monoclinic form while having a 435 ps lifetime in the orthorombic form. Also, differences in fluorescence behavior between thin polycrystalline films and single crystals of tetracene are explored to reduce discrepancies in the literature as to tetracene's singlet fission rate and whether or not its activated by temperature. We find here that single crystal's of tetracene have an average singlet fission lifetime of 170 ps while the polycrystalline films have a lifetime of 70 ps, which we attribute to differences in the number of defects due to grain boundaries and sample preparation. This study also studies the integration of tetracene films with n-type silicon in order to harvest the generated triplets for photovoltaic applications, but evidence was only seen for singlet transfer to the silicon.

Contents

List of Figures viii

List of Tables x

1 Introduction 1
- 1.1 Energy Consumption and Production . . . 1
- 1.2 Singlet Fission in the Literature . . . 4
- 1.3 This Work . . . 10

2 Experimental Details 14
- 2.1 Sample preparation . . . 14
  - 2.1.1 Tetracene . . . 14
  - 2.1.2 Rubrene . . . 18
- 2.2 Laser Systems . . . 19
  - 2.2.1 40kHz Ti:Sapphire Laser system . . . 19
  - 2.2.2 80 MHz MaiTai Oscillator . . . 22
- 2.3 Experimental apparatus . . . 23
  - 2.3.1 Vacuum Pump Setup . . . 23
  - 2.3.2 Temperature Dependent Experiments . . . 23
  - 2.3.3 Magnetic Field Stage . . . 25
  - 2.3.4 Polarized light microscopy . . . 26
- 2.4 Time Resolved Fluorescence Experiments . . . 27
  - 2.4.1 Solid State Samples . . . 28
  - 2.4.2 Samples in Solution . . . 30
- 2.5 Steady State Spectroscopic Measurements . . . 31
  - 2.5.1 Absorption . . . 31
  - 2.5.2 Fluorescence . . . 31

3 Magnetic Field Effects 33
- 3.1 Two Electron System . . . 33
- 3.2 Four Electron System . . . 35

3.3 Magnetic Field Effects . . . 38
3.3.1 Quantum Mechanical Model . . . 38
3.3.2 Merrifield Kinetic Model . . . 40
3.3.3 Expanded Merrifield Kinetic Model . . . 44

4 Applications **54**
4.1 General Approach . . . 55
4.2 Tetracene . . . 56
4.2.1 Magnetic field effects on energy levels and quantum beats . . . 56
4.2.2 Kinetic modeling of the magnetic field effects . . . 62
4.3 Rubrene . . . 71
4.3.1 Introduction . . . 71
4.3.2 Results . . . 73
4.3.3 Conclusions . . . 95
4.4 Diphenylhexatriene . . . 96
4.4.1 Kinetic modeling of the magnetic field effects . . . 100

5 How Crystal Morphology Influences Singlet Fission Dynamics **103**
5.1 Introduction . . . 103
5.2 Results and Discussion . . . 105
5.2.1 Polarized Light Microscopy . . . 105
5.2.2 Time-Resolved Fluorescence . . . 106
5.3 Conclusion . . . 117

6 Studying Energy Transfer into Si from Tetracene Using Fluorescence Quenching **118**
6.1 Introduction . . . 118
6.2 Results and Discussion . . . 120
6.3 Conclusion . . . 131

7 Conclusions **133**
7.1 Summary and conclusions . . . 133

Bibliography **139**

List of Figures

1.1 Solar spectrum . . . 3
1.2 Illustration of singlet fission . . . 5
1.3 Illustrations of photovoltaic devices . . . 9
1.4 Molecular structures . . . 11

2.1 Tetracene/Si sample . . . 17
2.2 Diagram of the 40 kHz laser setup . . . 21
2.3 Diagram of the MaiTai laser setup . . . 24
2.4 Magnetic Field Stage . . . 26
2.5 Streak camera diagram . . . 29

3.1 Kinetic schematic for tetracene . . . 45
3.2 Kinetic schematic for rubrene . . . 48

4.1 Tetracene molecular and crystal axes . . . 57
4.2 Extracted quantum beats from tetracene . . . 60
4.3 Oscillation frequency vs B-field angle . . . 61
4.4 Histogram of singlet character for tetracene . . . 63
4.5 Magnetic field effect 20 ns: tetracene . . . 65
4.6 Magnetic field effect 100ns: tetracene . . . 67
4.7 Temperature dependent fluorescence decay of rubrene . . . 73
4.8 Illustration of axes used for magnetic field effect calculations . . . 77
4.9 Singlet projections for rubrene . . . 78
4.10 Simulated fluorescence decays . . . 80
4.11 Magnetic field effect: rubrene . . . 82
4.12 Power dependence: rubrene . . . 84
4.13 Simulated magnetic field effect 20 ns: rubrene . . . 86
4.14 Simulated magnetic field effect 200 ns: rubrene . . . 87
4.15 Crystal packing structure of diphenylhexatriene . . . 97
4.16 Fluorescence decay: diphenylhexatriene . . . 99
4.17 Magnetic field effect: diphenylhexatriene . . . 102

5.1 Polarized light microscopy 106
5.2 Fluorescence decay comparison for various tetracene morphologys . . 107
5.3 Temperature dependence of single crystal and polycrystalline tetracene 109
5.4 Arrhenius plot: tetracene 110
5.5 Quantum beats for different tetracene morphologies 112
5.6 Fluorescence spectra of tetracene 114

6.1 AFM images of tetracene/Si samples 121
6.2 Steady state fluorescence of tetracene/Si with LiF blocker 122
6.3 Fluorescence intensity vs LiF thickness for tetracene/Si samples . . . 123
6.4 Simulated fluoresence decays for tetracene/Si samples 125
6.5 Angular dependence of the fluoresence for various LiF thicknesses . . 128
6.6 Lifetime vs tetracene thickness 130

List of Tables

4.1 Parameters used for simulated tetracene fluorescence decay 66
4.2 Parameters from the biexponential fit of rubrene fluorescence decay . 74
4.3 Parameters from the triexponential fit of rubrene fluorescence decay . 83
4.4 Parameters for simulated rubrene fluorescence 87
4.5 Kinetic rates for diphenylhexatriene crystal fluorescence 100

Chapter 1

Introduction

1.1 Energy Consumption and Production

The energy consumption rate of humanity is at an all time high and the demand for energy increases with each passing year. Renewable energy resources have recently come into favor as they have a low environmental impact, are effectively infinite resources, and are becoming more efficient as more time and money is being invested into researching their possibilities. One such renewable energy resource, solar energy, has the potential to generate large amounts of energy for the planet. A quick calculation using the flux of radiation coming from the sun will show that the total energy we receive from the sun each year is $\sim 2.75x10^{24}$ J even if we only assume 50% of the radiation hits the surface. This is a reasonable assumption as on average, much of the light is either absorbed or scattered due to the atmosphere before reaching the

surface.[1] If this value is compared to the amount of energy consumed by the human population in 2013, $5.68x10^{20}$ J,[2] we can see that there is easily enough power coming from the sun to power the entire planet.

To collect the energy from the sun in the amounts needed for humanity today, we need photovoltaic devices that can perform efficiently. The theoretical limit for a single p-n junction solar cell is 34% as calculated by Shockley and Quiesser.[3] While this limit includes many factors such as the possibility of charge recombination and fill factor, the largest reason for this limit is due to spectral losses. Consider a single junction silicon solar cell with a band gap of 1.1 eV. Photons that have an energy below this band gap will not be absorbed by the photovoltaic material, which leads to a loss of approximately 19% if the spectrum of sunlight is considered. Photons higher in energy will be absorbed and generate excitons, but these excitons will energetically relax to the level of the band gap, releasing the excess energy as heat. From spectral losses alone, there is approximately a 56% efficiency loss in these single junction silicon solar cells.[3] To overcome these spectral losses, we can consider upconversion and downconversion schemes. Upconversion transforms two lower energy photons into a higher energy photon so absorption still occurs at wavelengths higher than the band gap. Downconversion transforms a high energy photon by splitting it into multiple lower energy photons which would ideally closely match the band gap of the material, negating losses due to heat. One example of upconversion is triplet-triplet annihilation where low energy triplet states are generated in nanocrystals and subsequently

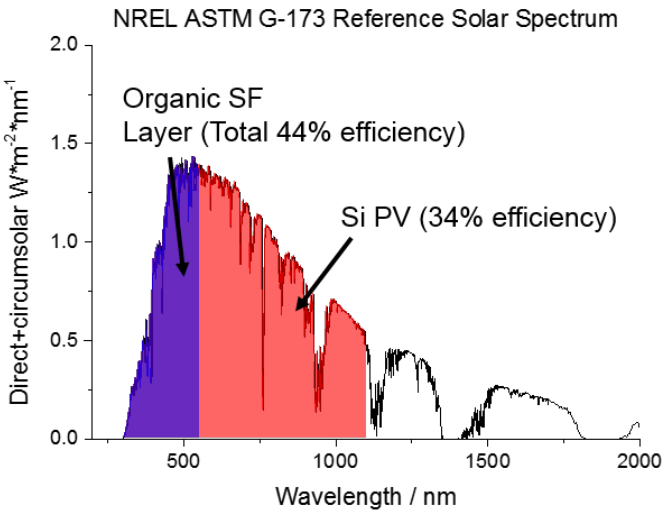

Figure 1.1: ASTM G173-03 solar spectrum take from NREL illustrating the solar irradiation on the Earth's surface. Overlaid in red is the region which Si can absorb with the right edge being the band gap of Si at 1.1 eV. The blue region illustrates the absorption range for a typical singlet fission organic material. The Si photovoltaic device alone would yield a maximum of 34% efficiency, but adding an organic sensitizer capable of singlet fission could increase the efficiency to 44%.

transfered to organic molecules where annihilation occurs to produce higher energy singlets.[4–7] There are many different downconversion schemes that can be used. One of them, called quantum cutting, involves rare earth ions absorbing one high energy photon and emitting two lower energy photons.[8,9] Another involves quantum dots of inorganic semiconductors in which the absorbed photon is used to create multiple excitonic species in a process known as multiple exciton generation.[10] Analogous to this process is singlet fission, in which a singlet excited state of an organic semiconductor is split into two triplet excited states.[11,12]

To better utilize the solar spectrum, we propose using the singlet fission (SF) process to efficiently harvest light. As previously mentioned, SF is a multi-exciton

generating process in which two triplet excitons are generated in the SF material per one photon input. The idea is that SF materials can be used to collect higher energy photons and instead of these excitons relaxing down to the band gap generating waste heat in the process, the excess energy will be utilized to create an additional exciton which can then be used to generate higher currents in the photovoltaic device. Figure 1.1 illustrates this concept. It has been found that for single junction solar cells that utilize SF, the maximum theoretical efficiency increases from 34% to 44%.[13] One advantage SF materials have over other multiexciton generating materials is that they generate triplets which tend to have long lifetimes (∼ms) due to the forbidden triplet to ground state singlet transition, which should allow for higher efficiencies as longer lifetimes would allow for longer diffusion lengths which would make the triplets easier to harvest. This dissertation will focus on the downconversion scheme of singlet fission and how the process occurs, with an emphasis on spin characteristics of the resultant triplet states and morphology of the systems in which singlet fission occurs.

1.2 Singlet Fission in the Literature

As mentioned in the previous section, singlet fission (SF) is a multiexciton generating process which generates two excitons per photon. The process was first discovered in 1965 by Singh et al. when studying the fluorescence properties of anthracene single crystals.[14] SF occurs by exciting a material from its ground state singlet (S_0) to its

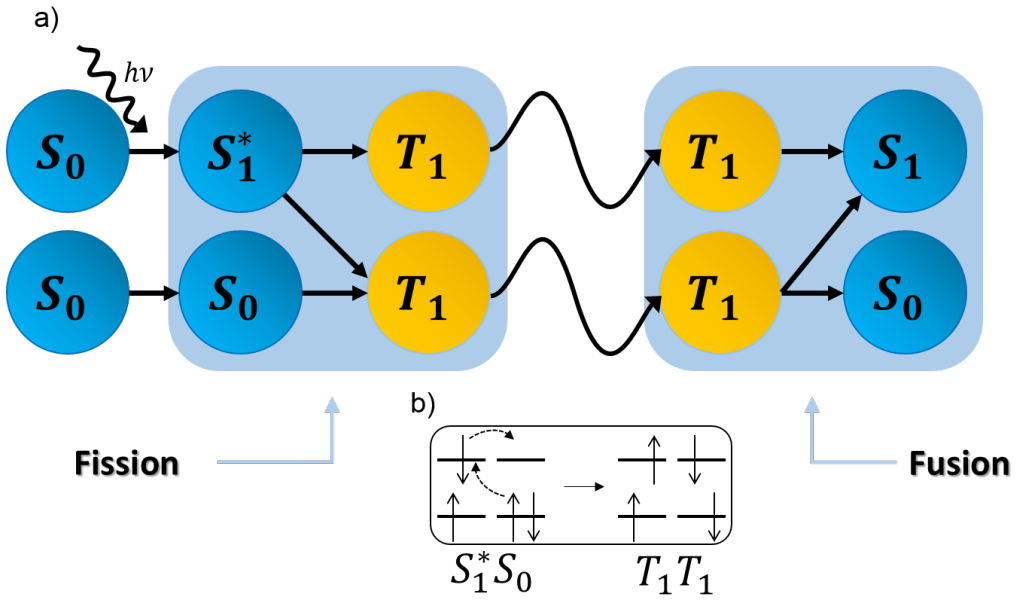

Figure 1.2: a) A cartoon showing the transition from one singlet excited state to two triplet states, subsequent diffusion, and then triplet-triplet annihilation or triplet fusion to form a singlet excited state again. b) An illustration of the HOMO and LUMO of the two chromophores for the singlet excited state and the triplet pair state. This shows how singlet fission can occur without flipping an electron spin.

excited singlet state (S_1) to yield one singlet exciton. This singlet exciton then splits into two triplet excitons which correspond to the first excited triplet state (T_1). It should be noted that the reverse process of triplet fusion, two triplet excitons coming together to form one singlet exciton, can also occur. These processes are illustrated in Figure 1.2. SF requires a few major requirements to occur efficiently. One of these is that E_{S_1} must be greater than or approximately equal to $2E_{T_1}$. This is simply for energy conservation. Also, the excited molecule must be able to couple to a nearby chromophore. This leads to a large geometry dependence between the two molecules which are performing SF. According to previous theoretical work, a slip-stacked cofa-

cial arrangement of the chromophores promotes SF most efficiently.[11,12] In the search for molecules to perform SF efficiently, it is also preferable to find systems with high quantum yields so that SF does not have to compete with internal conversion and intersystem crossing.

There are many systems that have been surveyed for efficient SF. Anthracene was the first system in which SF was discovered by Singh et al.[14] They found that anthracene could produce triplets in different ways when excited by different wavelengths of laser light from a Ruby laser. Two photon excitation from a 694 nm source lead to excitation to an excited singlet state which then decayed non-radiatively to the lowest excited singlet state which then underwent intersystem crossing to form triplet excitons. They also found that by using the second harmonic of their light source, that they were able to excite to a singlet state which produced two triplets directly. They were able to see two major contributors to the fluorescence intensity which they termed the "prompt" fluorescence which was due to the decay of the singlets after excitation, but before a large population of triplets had been created, and the "delayed" fluorescence which was due to triplet-triplet annihilation forming singlets which then radiatively decayed. This conclusion would be later supported by research done by Johnson et al. where magnetic fields were found to decrease the delayed fluorescence intensity by altering the spin character of the triplet pair states.[15] A detailed theoretical analysis of these magnetic field effects was then explored by Johnson and Merrifield in 1970.[16] They showed that there are three triplet pair states

with singlet character without an applied magnetic field due to the zero-field splitting and that there are two triplet pair states with singlet character at high magnetic fields when the Zeeman effect dominates. It was concluded that this transition from 3 to 2 states was responsible for the magnetic field effects seen in the previous experiments. Johnson and Merrifield's kinetic theory explaining magnetic field effects will be discussed in further detail in Chapter 3 of this dissertation. These experiments paved the way for further research into singlet fission in another member of the acene family, tetracene.

Tetracene was found to perform the SF process even more efficiently.[17–19] As with anthracene, this was also confirmed using photoluminescence and magnetic field effects as seen by Geacintov et al.[18] The energies of the singlet and triplet states in tetracene match up very closely to give very efficient SF and triplet fusion with $E_{S_1} = 18600 cm^{-1}$ and $2E_{T_1} = 20200 cm^{-1}$.[20] Pope et al. saw a SF rate of $5\,\mathrm{ns}^{-1}$, much faster than the radiative lifetime of tetracene.[21] Triplet fusion allowed for the system to be studied using time resolved fluorescence as even though over 99% of singlets would fission into the dark triplet states over the course of 1 ns, the triplet fusion process allowed for triplets to recombine into bright singlet states. After research into SF was revived as a means to enhance solar cell efficiencies,[11,13] this molecule was extensively studied as a possible solar cell sensitizer and elucidate the mechanism of singlet fission to exploit its properties for higher device efficiencies.[22–27]

Since the revival of singlet fission research, many compounds have been found to produce triplet yields well over 100%. In the acene family, pentacene was found to undergo singlet fission, but on a timescale of femtoseconds. This was difficult to prove early on in singlet fission's history as solid-state pentacene does not fluoresce as the shorter linear polyacenes do.[28,29] Interestingly, it was noted that heterofission could occur within pentacene-doped tetracene where an excited singlet on a pentacene molecule could fission into a triplet state on a nearby tetracene molecule and a triplet state on itself.[30] Acene derivatives with phenyl groups attached to the main polyacene backbone were also studied in the form of diphenyltetracene and rubrene.[31–34] The phenyl rings attached to the polyacene backbone helped to distort the crystal structure and allowed the study of how structure affects singlet fission while largely keeping the photophysics intact. These molecules in their amorphous phases proved to have comparable fission rates to the linear polyacenes with diphenyltetracene and rubrene reported to have fission time constants of 0.8 ps and 0.5 ns respectively.[32,33] SF was also discovered within the polyene family and in particular zeaxanthin.[35–37] There are many other classes of molecules that exhibit singlet fission such as polymers, isobenzofurans, and perylenediimides.[38–40] Singlet fission shows up in a broad spectrum of compounds so long as all the requirements are met.

In recent years, researchers have begun to study how singlet fission photovoltaics can be made. In one approach, the singlet fission material can be included within the circuit as a donor. Baldo and researchers have found that organic photovoltaics using

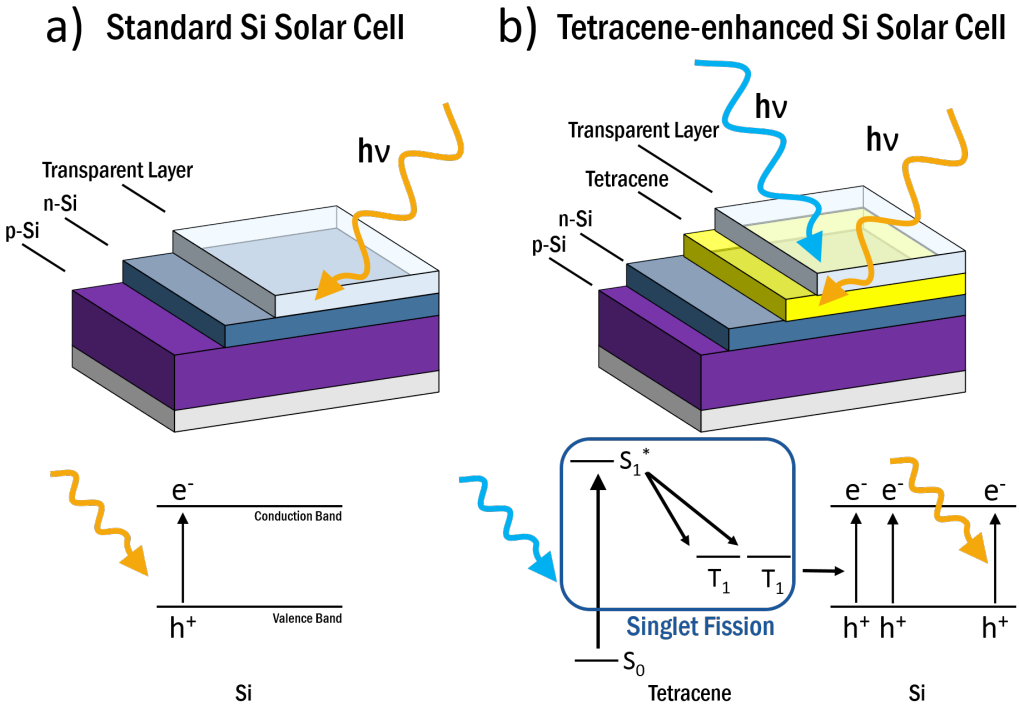

Figure 1.3: An illustration showing the differences between a) a conventional solar cell where one electron hole-pair is generated per absorbed photon, regardless of wavelength and b) a singlet fission sensitized solar cell where the higher energy photons which the organic layer can absorb will generate two electron hole pairs per photon while still retaining the normal electron hole pair generation from the Si layer.

a tetracene donor and C_60 acceptor have internal quantum efficiency of 127%.[41] A second approach is to use singlet fission materials as sensitizers,in which the triplet excitons from our organic material are transfered into a photovoltaic device which is typically an inorganic semiconductor. Efforts have been made to take members of the acene family and pair them with PbS and PbSe nanoparticles to achieve high triplet transfer efficiencies.[42,43] In the study by Tabachnyk et al., they found that for every photon absorbed by pentacene, 1.9 triplets were transfered to PbSe, noting that once the triplets have produced excitons in the nanoparticles, these excitons can

re-emit light or be converted into electron-hole pairs.[42] The study by Thompson et al. showed a comparable triplet transfer efficiency for the system of tetracene and PbS nanocrystals with ~ 1.8 triplets being transfered for each photon being absorbed by tetracene.[43] These studies show that singlet fission is a promising technology as it has been proven that the triplets can be extracted efficiently into inorganic semiconductors where they can be put to use.

1.3 This Work

This work will concern itself with improving our understanding of the basic properties of SF in well-characterized molecular systems. For example, we know tetracene's herringbone packing structure gives high triplet yields, but tetracene has its own problems with photostability. To search for molecules with better properties while still retaining high singlet fission yields, it is necessary to understand how crystal structure plays a role in determining the singlet fission rate. To do this, we not only look at various forms of tetracene, but also the tetracene derivative rubrene and diphenylhexatriene. The structures of these molecules are shown in Figure 1.4. To elucidate the properties of these molecules, the tried and true methods of magnetic field effects and time resolved fluorescence will be employed. In Chapter 3, we will discuss how magnetic field effects will manifest themselves differently based on the crystal packing structure of the system and in Chapter 4, the theory will be applied

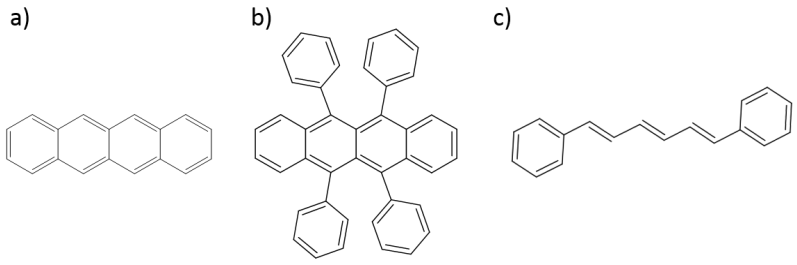

Figure 1.4: a) Tetracene b) Rubrene c) Diphenylhexatriene

to the aforementioned systems.

Tetracene will be the main subject of this dissertation, comprising Chapters 4, 5, and 6. In Chapter 4, magnetic field effects will be discussed in the context of single crystals of tetracene and polycrystalline films of tetracene. In the single crystal, theory will be presented to explain the angle dependence of the magnetic field in the **ab** plane of the crystal. To explain this, we will look at oscillations in the fluorescence decay, first seen by Chabr et al. and then later studied in our research group by Jon Burdett.[25,44] These quantum beats are caused by the existence of a triplet pair superposition state and the frequencies are defined by the energy spacings between the states involved in the superposition. We calculate how these energy spacings change as a magnetic field is rotated in the **ab** plane of a tetracene single crystal and quantitatively match the oscillation frequencies seen in experiment. For a polycrystalline film, we study how the magnetic field affects the dynamics of the system using a modified Merrifield approach.[15,16] This involves using a quantum mechanical description to determine the singlet character of the triplet pair states, of the system and then using these to determine rates in kinetic equations.

After discussing the magnetic field effects in the polycrystalline system of tetracene, rubrene will then be studied. This system is very similar to tetracene, containing the same four ringed polyacene backbone but with four attached phenyl rings which allow a meta-stable amorphous phase at room temperature. The film keeps relatively the same photophysics for the monomer, which allows us to study how the singlet fission dynamics and magnetic field effects change in an amorphous film. Again, magnetic field effects and time resolved fluorescence will be employed. The magnetic field effect model and kinetic model will be altered to fit the amorphous system.

Lastly, diphenylhexatriene will be discussed. While not a polyacene and therefore very different from the previous two molecules, this molecule has the advantage in that it has two stable single crystal polymorphs where the intermolecular distances and orientations change. Here the two different crystal polymorphs are compared and again magnetic field effects and time resolved fluorescence are used to extract information about the system. We also extend the Merrifield kinetic scheme to suit the system and calculate the singlet character of the triplet pair states when the magnetic field is applied as before.

In Chapter 5, tetracene single crystals and tetracene polycrystalline films will be compared. In the past, researchers have come up with different answers for whether or not singlet fission in tetracene was and activated temperature dependent process, and a variety of singlet fission rates have been seen in experiments.[22,24,45] Based on the energetics of $E_{S_1} = 18600$ cm^{-1} and $2E_{T_1} = 20200$ cm^{-1},[20] it is expected to be

an uphill process and therefore activated by temperature, yet Wilson et al. found that even at 10 K fission was still present in a polycrystalline film of tetracene.[22] Others have also found a lack of a temperature dependence in polycrystalline films of tetracene.[23,27,46] On the other hand Arnold et al. did find a temperature dependent triplet yield in a single crystal of tetracene.[45] Also the observed singlet fission rates are much faster in the polycrystalline film($\sim$ 80ps)[24] as compared to the single crystal($\sim$ 200ps)[26] This section will discuss how these two cases are different and use time resolved fluorescence to determine why these differences arise.

In Chapter 6, we attempt to sensitize n-type silicon with tetracene. It has been proposed in the past that Frenkel type triplet excitons could sensitize Wannier excitons in an inorganic semiconductor.[47] If triplet transfer from tetracene to silicon is possible, one of the simplest ways to make a singlet fission sensitized solar cell would be to simply place a film of tetracene on top of silicon. Previously, Boyd et al. explored this concept by depositing tetracene onto crystalline Si with and without a LiF spacer layer and found that Si did indeed quench the integrated fluorescence from the tetracene.[48] It was not clear from this study whether or not this was due to singlet or triplet energy transfer from tetracene to Si. Triplet energy transfer should be energetically possible as the energy of the tetracene triplet matches the 1.1 eV band gap of silicon rather well. We use time resolved fluorescence to study the fluorescence quenching of the tetracene by the silicon under a variety of conditions including different film thicknesses and intermediate layers.

Chapter 2

Experimental Details

This chapter will discuss the various experimental techniques and methods used to perform the experiments contained within the rest of the paper. Included inside are the details of sample preparation, a discussion of the laser systems used to perform the experiments, a description of the various experimental tools used to characterize samples, and details on how fluorescence measurements were taken.

2.1 Sample preparation

2.1.1 Tetracene

Tetracene Crystals

Tetracene single crystals were prepared using Benz[b]anthracene sublimed grade, 99.99% trace metal basis as purchased from Sigma Aldrich with no further purifica-

tion. In an un-lit room, a 0.7 mM solution was prepared in toluene and subsequently filtered through a Whatman qualitative 1 filter. The resulting solution was then dropped onto a Thermo Fisher pre-cleaned glass microscope slide and left to evaporate in a dark desk drawer for 24 hours in air. The resulting crystals were then examined using optical microscopy. These crystals vary in shape and size, but this process tends to create crystals which have a relatively large ($\sim$1 mm^2) surface area, appear rhombohedral, and show uniform extinction using polarized light microscopy. It is these crystals which are used for the experiments described within this dissertation.

Experiments were conducted to see if the yield of crystals with favorable characteristics could be increased. Using a finer filter, such as a Whatman qualitative 5 filter, had no qualitative effects on the crystal growth. Preparing the glass slides in various ways had some effect on the crystals growth patterns. Cleaning the slide with a base bath before drop casting did not make a discernible difference, but using a piranha bath (3:1 sulfuric acid:hydrogen peroxide) caused the growth of many smaller crystallites ($<$10 µm^2) near the edges of the glass slide which tended to not show favorable fluorescence characteristics.

Tetracene Polycrystalline Films

The polycrystalline films of tetracene were prepared using a Pelco vacuum evaporator. The crucible which contains the material to be deposited on the slide was

filled with ∼1 mg of Benz[b]anthracene sublimed grade, 99.99% trace metal basis as purchased from Sigma Aldrich with no further purification. First the chamber is rough pumped to 1.0x10^{-3} Torr as measured by the gauge on the evaporator. Then using the diffusion pump, the chamber was pumped down to 1.5x10^{-5} Torr while the pump cooled with liquid N_2. The Dewar containing the liquid N_2 needed to be filled every 45-60 minutes to reach the desired pressure. When depositing the tetracene onto the slide, the electrode, set to a voltage of 65 V, was turned on for 10 second intervals and the slide was checked by eye between each interval. When a yellow color appeared on the slide, after 3 to 4 of these 10 second intervals, the process was ended and the slide was removed from the evaporator. The films used in these experiments showed a peak absorbance of ∼0.3.

Tetracene on Silicon

Tetracene on silicon samples were prepared by the Lee group in Taiwan as follows. A lightly doped (resistivity, ρ =20Ω-cm) n-type (100) Si substrate was cut into 1.5 cm x 1.5 cm squares, followed by ultrasonic cleaning with acetone, isopropyl alcohol, and de-ionized (DI) water (ρ =18MΩ-cm), each for 5 min. The substrate was then immersed in piranha solution (H_2SO_4:H_2O_2 = 3:1 in volume ratio) at 80 °C for 5 min, followed by DI water rinsing.[49] Then, a buffer oxide etching solution (NH_4F:HF = 6:1) was used to remove the oxide on the silicon wafer for 5 min, creating a hydrogen terminated surface.[50] The substrate was transferred into vacuum chamber with base

pressure of 10^{-5} Torr and the LiF and tetracene thin films were deposited by thermal evaporation.[51] After thin film deposition, the samples were directly transferred into a N_2 glove box with (O_2 and $H_2O < 1$ ppm) for encapsulation.

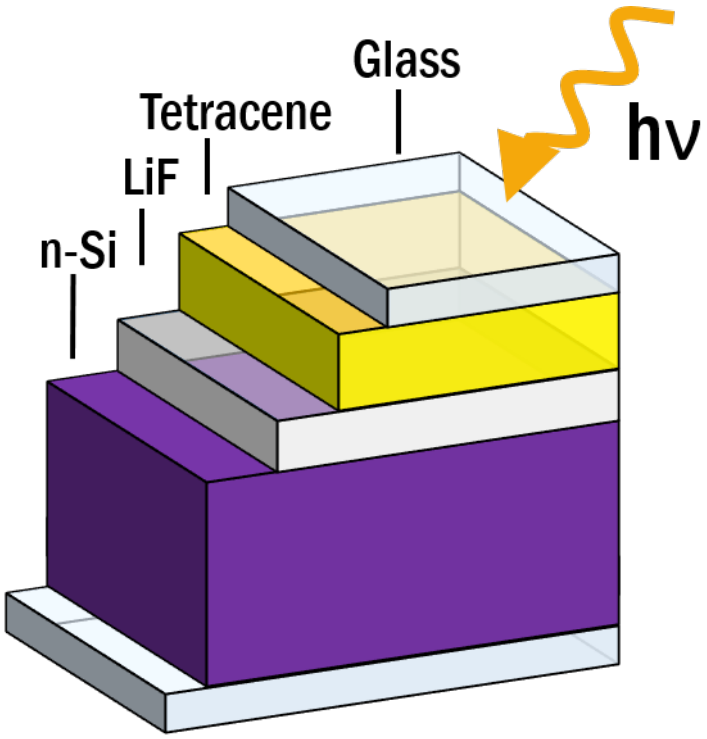

Figure 2.1: Illustration showing the different layers of the samples studied in the time-resolved fluorescence experiments. Both the LiF and tetracene thicknesses could be varied as needed.

A cleaned glass substrate with UV sealant on the periphery covered the sample, followed by UV light illumination to seal the sample under a pure-N_2 atmosphere. With encapsulation, the samples exhibited stable optical characteristics even after storage for 6 months. An illustration of a typical sample can been seen in Figure 2.1.

2.1.2 Rubrene

Amorphous Rubrene Films

Amorphous rubrene films were created using 99% pure rubrene purchased from Sigma Aldrich which was used as received. The films were spin-coated onto a glass microscope coverslip using a chloroform solution containing 7 mM rubrene for 30 s at 3000 rpm. These films were characterized as amorphous due to the lack of any peaks in the powder X-ray diffraction measurements and the absence of any crystalline domains observable by polarization and fluorescence microscopy. The thickness of the films was found to be <10 nm as estimated through optical absorption measurements

Polymer films Containing Rubrene

Films were produced by drop-casting a toluene solution containing ∼10% by weight polystyrene and 0.7 mM rubrene onto a glass microscope slide yielding a polystyrene film containing approximately 8.3 mM rubrene. These were wrapped in foil and allowed to dry in a dark desk drawer.

2.2 Laser Systems

2.2.1 40kHz Ti:Sapphire Laser system

This system consists of three separate units, all of which were required to be working optimally to ensure a strong 800 nm output. This section will discuss each unit and its importance to the system.

Kapteyn-Murnane Laboratories (KML) Model TS Ti:sapphire Laser (Oscillator)

This laser acts as the seed for the regenerative amplifier (RGA). It is pumped by a diode-pumped Nd:VO_4 laser (Millenia, Spectra Physics) at 532 nm. The typical output of this oscillator is $\sim$260 mW of 800 nm when mode-locked and pumped with 3.31 W of 532 nm of pump power. While this laser could be used standalone to perform experiments, the experiments conducted in this paper required either 400 nm light or another wavelength in the visible region selected by white light continuum generation and filters. The peak pulse power of this laser system alone is not enough to effectively generate these wavelengths through non-linear processes and therefore amplification of the beam by the rest of the components is necessary.

Spectra Physics Merlin Laser System (Pump for the RGA)

This system is the pump for the RGA system. It employs a flashlamp to pump a Nd:YLF rod to generate 1053 nm laser light. A lithium triborate (LBO) crystal is

used to double this light to get the proper wavelength to pump the Ti:sapphire in the RGA. To achieve pulsed operation, a Q-Switch is employed which switches at 40 kHz. During my tenure in the Bardeen lab, the typical 527 nm seen out of this system was 7 to 8 W when pumped with a flashlamp run at 5.1 kW (Max power).

The power output of this laser largely determines the output power of the entire system and must be kept in optimal working condition if the entire system is to work. Overtime, power loss was found to mainly come from two main sources, the flashlamp and the laser rod. The flashlamps were typically replaced when the power dropped by 1 W and a rise in the output power was seen after replacement. At an undetermined point, the face of the rod became chipped which led to a power decrease to 3.2 W and caused the RGA to stop lasing. After refurbishing the rod, the system was realigned and a power of 6 W was achieved, but other problems within the system and flashlamps were experiencing large amounts of corrosion after only being on 3-4 hours. At this time, the problems in the Merlin have caused the 40 KHz system to be non-functional.

Spectra Physics Spitfire System (RGA)

A Ti:sapphire system that utilizes both the Merlin as a pump and the KML as a seed to generate and amplify laser pulses in a cavity. The typical output of this system was $\sim$ 200mW of 800 nm light at 40 kHz. There are two main ways this output beam was used in experiments conducted in this thesis. The first is utilization of a

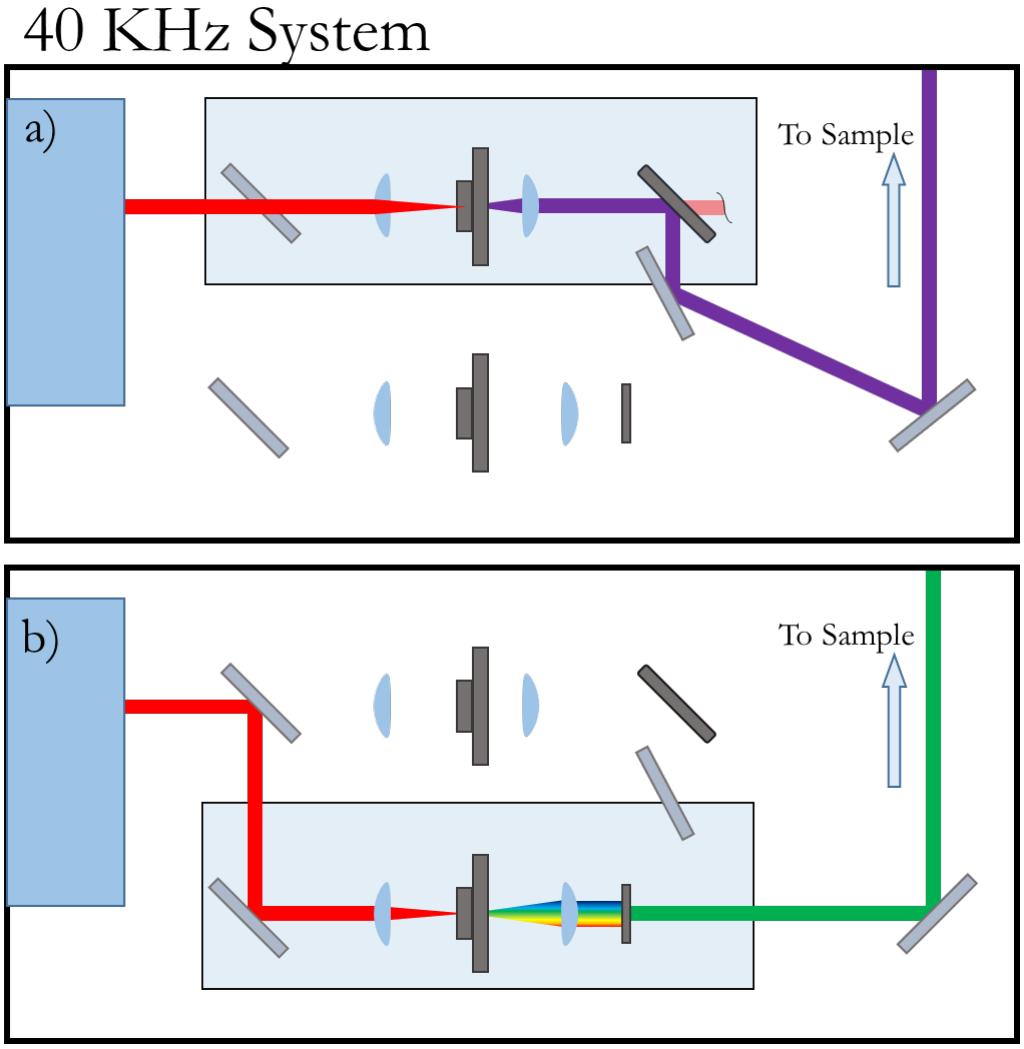

Figure 2.2: A not to scale diagram of the optics used to manipulate the output of the Spitfire regenerative amplifier. The two different paths shown in this system are a) conversion of the 800 nm light to 400 nm using a BBO crystal and subsequent filtering out of the 800 nm with a dichroic mirror and b) continuum generation in a sapphire crystal allowing for the selection of a wavelength in the visible region using an interference filter.

beta barium borate (BBO) crystal to frequency double the 800 nm light to generate 400 nm light. The leftover 800 nm light was then filtered out and the resulting 400 nm light was then used to excite the sample. The second way is using a sapphire crystal to generate white light continuum. Particular wavelengths for excitation could then be selected using interference filters. A diagram illustrating these two different methods can be found in Figure 2.2.

2.2.2 80 MHz MaiTai Oscillator

The MaiTai laser system was used as a standalone laser once the 40 KHz system had degraded in power to an unusable point. The output out of this system can be tuned from 700-900 nm, but was typically run at 800 nm with an average power output of 1.5 W. Besides the laser itself, many other optical elements were added to make this system usable for time resolved fluorescence measurements as shown in Figure 2.3. First a keplerian telescope was used to reduce the beam diameter in order to fit through the aperture of a ConOptics pulse modulator. This pulse modulator was used to alter the repetition rate of the system. This was necessary for many of the chemical systems studied on the laser system as the unaltered time between pulses is 12.5 ns, much shorter than the lifetime of the molecules studied. Following the pulse modulator, a pulse compressor was put in place to obtain better frequency doubling efficiency. Since 800 nm is typically too low energy to excite the studied samples, the beam was frequency doubled to 400 nm using a BBO crystal. The resulting 400 nm

light is then used for excitation while the residual 800 nm light is filtered out using a dichroic mirror.

2.3 Experimental apparatus

2.3.1 Vacuum Pump Setup

To pull vacuum on the solid state samples, a BH2-60HD oil-free pump from DRI-VAC is attached either to the Janis ST-100 or ST-300 cryostat depending on which is needed. To monitor the pressure within the vacuum line and the cryostat, an MC300 gauge from Televac is used. The system reaches 1.0x10^{-3} Torr in $\sim$5 minutes with either cryostat and will continue to drop to $\sim$1.0x10^{-4} Torr over the course of a few hours. This system is used for both time-resolved and steady state fluorescence measurements.

2.3.2 Temperature Dependent Experiments

The configuration for conducting a temperature dependence of the fluorescence is determined by the range of temperatures that require study. For temperatures above room temperature, the cryostat was simply heated using a heater controlled by either a model 335 Lakeshore controller for the Janis ST-300 cryostat or a 321 Lakeshore controller for the Janis ST-100 cryostat. The upper temperature limit for the ST-300 is 500 K while the upper limit for the ST-100 is 325 K. For temperatures lower than

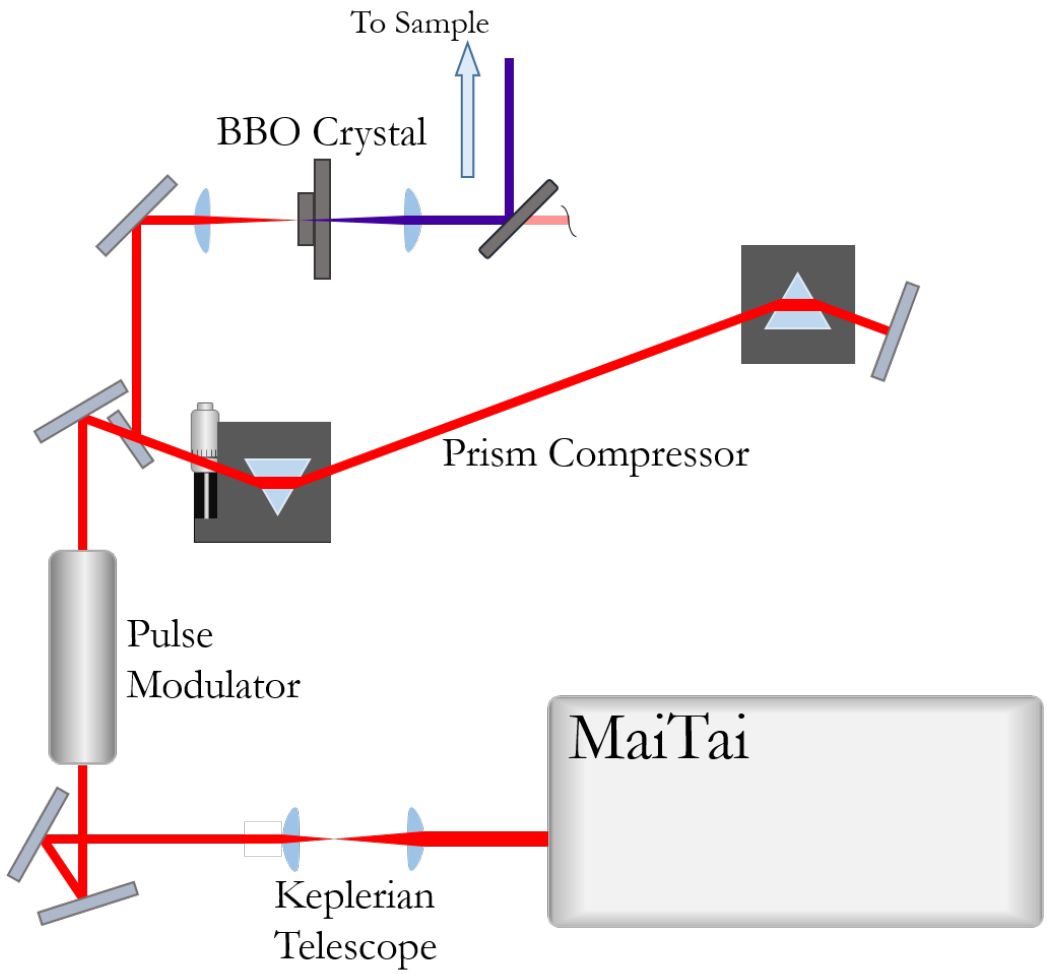

Figure 2.3: A not to scale diagram of the optics used to manipulate the MaiTai beam for fluorescence measurements. For 800 nm light, silver mirrors were used while for 400nm light, aluminum mirrors were utilized.

room temperature, liquid N_2 was used in conjunction with the appropriate temperature controller. To transfer liquid N_2 into the cryostat, a Dewar vessel filled with liquid nitrogen was pressurized using the compressed air output of the fume hood and a vacuum-jacketed cryoliquid transfer line was placed between the cryostat and the Dewar. When liquid N_2 is introduced to the cryostat the temperature will drop to 77 K at which point higher temperatures can be reached using the temperature controller with the cryostat. When using the ST-100 cryostat, it is sometimes necessary to slow the rate of liquid N_2 entering the cryostat to reach a stable temperature, which can be done by either closing the valve on the transfer line by 2-3 full turns, or lowering the air flow into the N_2 Dewar by adjusting the air flow in the hood. If lower temperatures are required, the liquid N_2 can be substituted with liquid He. This setup can be applied to all of the time-resolved fluorescence experiments and the steady state experiments.

2.3.3 Magnetic Field Stage

To perform fluorescence measurements where a magnetic field is applied to the sample a custom magnetic field setup was created and utilized as seen in Figure 2.4. The magnetic field stage was custom manufactured by the UCR machine shop and magnets with a 2 diameter and a 2 length were bought from K&J magnetics (catalog #: DY0Y0-N50). When preforming measurements, the magnets were brought as close to the sample as possible. With a custom small brass cryostat the UCR machine made,

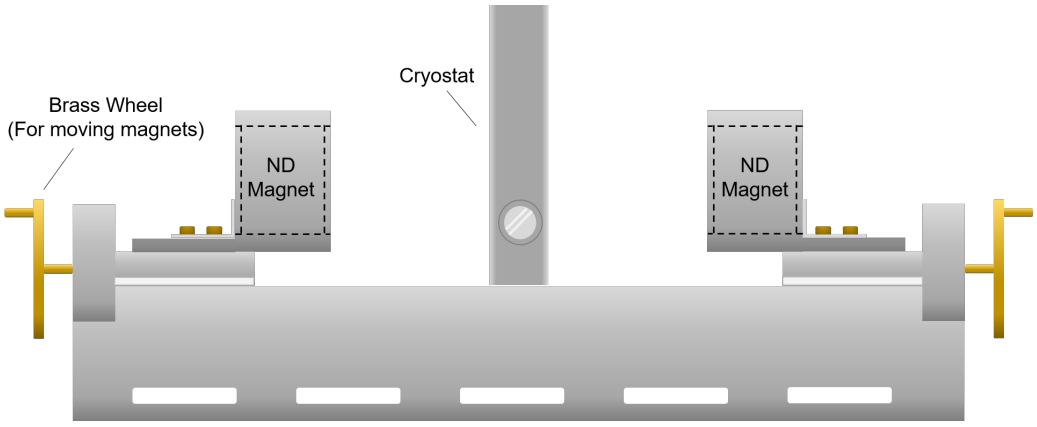

Figure 2.4: An illustration of the magnetic field stage used for magnetic field effect measurements. The base would be clamped to the laser table. The cryostat in the middle was originally a custom brass cryostat, but was later switched to a Janis ST-300 cryostat for temperature dependent measurements. The wheels on the ends of the stage could be turned to extend the magnets toward the sample.

this yielded a ∼8 kG magnetic field on the sample whereas with the Janis ST-300 due to its size, only a ∼2 kG magnetic field could be created on the sample. Nevertheless, as will be shown in this thesis, calculations show that the effects saturate around 0.8 kG meaning there should be no visible difference in the fluorescence dynamics when utilizing different sample holders.

2.3.4 Polarized light microscopy

Polarized light microscopy measurements were taken with a 10x objective with a 0.25 NA. Two plastic thin film polarizers were placed on each side of the sample, one to polarize the light coming out of the light source and the other to polarize the collected light after passing through the crystal. This allows us to exploit the birefringent properties of the crystalline samples which alters the polarization of light

passing through the crystal. To identify single crystals with favorable traits, the polarizer between the sample and the objective lens was rotated until the background became dark and single crystal facets remained lit. Pictures of the crystals could then be saved using a USB camera to reference later during time-resolved fluorescence experiments.

2.4 Time Resolved Fluorescence Experiments

Time resolved fluorescence experiments were conducted using one of the previously mentioned laser systems and the Hamamatsu Streak Camera as a detector. Fluences were generally kept as low as possible (typically on the order of 10^{-6} J cm^{-2}) while still getting reasonable signal to noise ratios. This was to avoid various effects such as photodamage and singlet-singlet annihilation. Photodamage was checked for by monitoring the integrated fluorescence intensity throughout the course of an experiment. If signal was lost over time, the sample was moved slightly to check for recovery of the signal. If the signal recovered to its original state, we could conclude that the sample was being damaged or altered over time by the light source. Singlet-singlet annihilation, a bimolecular process, can be avoided by monitoring the first 100 ps of the fluorescence and lowering the power until changes in the fluorescence decay rate are no longer seen. This holds as long as we assume singlet fission is power independent and the triplet density is not high enough in this time region for triplet-triplet annihilation to affect the decay here. Unless otherwise specified, all experiments were

done with front face detection. Fluorescence from the sample was collected using a plano-convex lens and then later focused through the slit of the detector using another plano-convex lens, in our case a 5 cm fused silica lens. Stray excitation light was generally blocked using the appropriate longwave pass filter

The streak camera allows us to get both dynamic and spectral information from the sample. The camera works as follows. First photons enter the cameras attached monochromator, this give us our spectral resolution. Next, the photons hit a photocathode which will eject electrons through a cathode tube. An electrical trigger signal timed by the laser system then activates a time-varying electric field within the tube, deflecting electrons across an micro-channel plate (MCP). This gives us our time resolution as electrons traveling through the tube at early times experience a different electric field than at electrons at later times causing the electrons to be streaked. After being multiplied by the MCP, the electrons then hit a phosphor screen which is seen by the 640x480 pixel charged-coupled device (CCD) camera. Figure 2.5 illustrates these concepts. All time-resolved fluorescence data in this thesis was taken using this detector.

2.4.1 Solid State Samples

When performing fluorescence measurements on solid state samples, care was taken to minimize exposure to light before loading it into a cryostat where the sample was then stored under a less than $1x10^{-3}$ Torr atmosphere. This was done to minimize

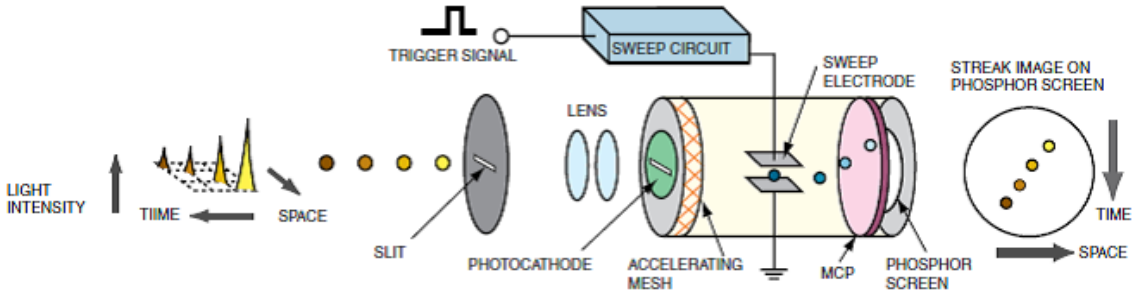

Figure 2.5: Illustration of the working principles of the streak camera taken from the Hamamatsu manual. In the experiments that were conducted in this lab, the space axis was transformed into a wavelength axis through the use of a monochromator.

the risk of photoxidizing samples before the oxygen surrounding the sample could be removed. Three different cryostats were used depending on what experiments needed to be done. The Janis ST-100 was initially used for all general measurements and all temperature dependent measurements whereas a custom small brass cryostat was used for magnetic field effects due to its thinness. A newer cryostat, the Janis ST-300, was eventually used for all experiments as it was thin enough to apply a magnetic field to the sample and had a temperature range of 4-500 K. The samples that were made for us by the Lee group were prepared in a nitrogen filled glovebox and encapsulated using a thin glass slide and a UV cured epoxy. It was assumed that the inert atmosphere inside the encapsulated samples did not leak out into the environment over time and that there was little risk of photoxidizing the organic film due to ambient lights or the excitation beam because of this. These samples were simply mounted on a lens mount using scotch tape and placed on a 2D-stage on the table. The experimental setup was altered for studying the amorphous rubrene films and molecules in dilute solution. Due to their isotropic nature, magic angle detection was used to eliminate

depolarization effects. This is done by polarizing the excitation beam, where the direction of polarization was chosen by the maximum transmission power through the polarizer, and then placing another polarizer between the sample and the detector which is rotated 54.7° from the excitation polarizer. This eliminates the anisotropy of the fluorescence intensity which can distort the fluorescence dynamics.

2.4.2 Samples in Solution

Solutions with the relevant sample were placed in a 1 cm quartz cuvette for study. Front face detection was also used for studying samples in solution unless otherwise stated. While this has a tendency to expose the detector to much more of the reflected excitation beam, generally there was no issue using longwave pass filters to remove this. As mentioned before, magic angle polarization was used to collect the fluorescence from these samples.

Degassing the Solution

As in the case of the solid samples, it was important to remove oxygen from the environment as to not promote the photoxidation of the samples. To achieve this with the samples studied in solution, the cuvettes containing the solutions were sparged with argon. To perform this procedure, a cap with a Teflon septum must be put onto the cuvette. Two needles are then inserted into the top of the cap. One of them is used to flow argon through into the solution and the other is simply acts as an outlet

for the air in the cuvette to escape. The sample is to be sparged with argon for 10 minutes. After the 10 minutes has passed, remove first the outlet needle and then the argon input needle.

2.5 Steady State Spectroscopic Measurements

2.5.1 Absorption

Absorption spectra were taken using a Varian Cary 50 UV/Vis absorption spectrometer. Solution samples were typically placed in a quartz cuvette for measurements. Polymer films could also be mounted in the system using adhesive putty. Typically absorption spectra were taken using the preset Normal setting for integration time and step size.

2.5.2 Fluorescence

Fluorescence and excitation spectra were collected on a Horiba Fluorolog 3 fluorimeter. The system includes two separate sample holders which could be used for either a solution based sample in a cuvette or a solid sample. If possible, the sample for fluorescence was prepared so that the absorption of the sample as $\sim$0.3, which helped to diminish the possibly for the self-absorption of the samples fluorescence. In the case of solution samples this could be achieved through dilution, while for samples such as polycrystalline films, this could be done by creating a thinner film. The setup

for the fluorimeter was, unless stated otherwise, an integration time of 1.0 s, a step size of 1.0 nm, and both the entrance and exit slits were set to 2.0 nm. Samples in solution were measured using a right angle collection configuration while solid state samples were measured using front face collection. For the solid state samples that were not encapsulated, the sample was placed in a Janis ST-100 cryostat and subsequently pumped down to $<1.0\text{x}10^{-3}$ Torr which could then be placed in the sample holder position in the fluorimeter using a custom aluminum mount.

Chapter 3

Magnetic Field Effects

In this chapter, the effects of magnetic fields on the fluorescence dynamics of singlet fission systems will be examined using a theoretical framework. Magnetic field effects help provide evidence for singlet fission by proving the existence of triplet-triplet annihilation in the system, which would arise due to the dense triplet population generated by singlet fission. They also allow us to quantitatively model the system and obtain rates such as the singlet fission rate, triplet-triplet annihilation rate, and spin-lattice relaxation. This approach is based on work done by Merrifield et al and Frankevich.[15–17,52–54]

3.1 Two Electron System

To understand why magnetic fields affect the system, the nature of the triplet state must first be discussed. In a two electron system, there can four different spin

states, one singlet and three triplets. These states can be found as eigenstates of the S^2 operator in the single half-spin basis($|\alpha\rangle$,$|\beta\rangle$) for a two electron system and are described by the following equations in Dirac notation

$$\begin{aligned} |S\rangle &= \frac{1}{\sqrt{2}}(|\alpha\alpha\rangle - |\beta\beta\rangle) \\ |T_+\rangle &= |\alpha\alpha\rangle \\ |T_0\rangle &= \frac{1}{\sqrt{2}}(|\alpha\beta\rangle + |\beta\alpha\rangle) \\ |T_-\rangle &= |\beta\beta\rangle \end{aligned} \tag{3.1}$$

Being eigenstates of the S_z operator, they can also describe the states when a strong magnetic field B_z is applied to the system. The Hamiltonian for the magnetic field is

$$\hat{H}_{B-field} = g\beta \left[h_z \hat{S}_z \right] \tag{3.2}$$

g_s is the dimensionless g-factor, β is the Bohr magneton and $\mathbf{h}_z$ is the strength of the magnetic field in the z axis. By applying this Hamiltonian to these wavefunctions, one can then show that the energy of the $|T_+\rangle$ state increases and the energy of the $|T_-\rangle$ state decreases while the $|T_0\rangle$ and $|S\rangle$ states remain unaffected.

In the absence of a magnetic field, there is effectively a dipole-dipole interaction between the two electrons that can be described using what is known as the 'zero-field'

Hamiltonian,

$$H = D\left[(\hat{S}_z)^2 - \frac{1}{3}\hat{S}^2\right] + E\left[(\hat{S}_x)^2 - (\hat{S}_y)^2\right] \tag{3.3}$$

where D and E are the 'zero-field' field parameters which determined the amount of splitting between the triplet levels and are typically determined experimentally using electron paramagnetic resonance measurements. The triplet eigenstates of this system are

$$\begin{aligned} |x\rangle &= \frac{1}{\sqrt{2}}(|\beta\beta\rangle - |\alpha\alpha\rangle) \\ |y\rangle &= \frac{i}{\sqrt{2}}(|\beta\beta\rangle + |\alpha\alpha\rangle) \\ |z\rangle &= \frac{1}{\sqrt{2}}(|\alpha\beta\rangle + |\beta\alpha\rangle) \end{aligned} \tag{3.4}$$

Now we have two different basis, the 'zero-field' basis of $|x\rangle, |y\rangle, and\, |z\rangle$ and the high-field basis of $|T_+\rangle, |T_0\rangle, |T_-\rangle$. It will be shown in the following sections that it is this change of basis from zero-field to high-field that causes the magnetic field effects in the singlet fission system.

3.2 Four Electron System

In the case of singlet fission, we now must look into spin states of a four electron system. For singlet fission to occur, you need an excited singlet and a nearby ground

state singlet, this would consist of one molecule A having one electron in the HOMO and one in the LUMO, while the other molecule B has both electrons in the HOMO. To find all of the spin states in this system, we can again use the $\hat{S}^2$ operator. When the 4-electron product basis is diagonalized using this operator, we find 16 eigenstates: 2 singlets, 9 triplets, and 5 quintets. First let's examine the singlet states. The first one happens to be the product of two 2-electron singlet states.

$$|S_1\rangle = \frac{1}{\sqrt{2}}(|\alpha\beta\rangle_A - |\beta\alpha\rangle_A)\frac{1}{\sqrt{2}}(|\alpha\beta\rangle_B - |\beta\alpha\rangle_B) \tag{3.5}$$

This shows that the overall two-molecule singlet state can be made from the product of singlet states i.e. S_0S_0, S_1S_0, S_0S_1, S_1S_1. This implies that both singlet fission into two singlets is possible while conserving spin and also that the reverse of singlet-singlet annihilation is a spin conserving process. The second state

$$\begin{aligned} |S_2\rangle = &\frac{-1}{\sqrt{3}}(|\alpha\alpha\rangle_A |\beta\beta\rangle_B + |\beta\beta\rangle_A |\alpha\alpha\rangle_B) \\ &+ \frac{1}{2\sqrt{3}}(|\alpha\beta\rangle_A + |\beta\alpha\rangle_A)(|\alpha\beta\rangle_B + |\beta\alpha\rangle_B) \end{aligned} \tag{3.6}$$

cannot be reduced to a product of singlets like the first, but can be written as a superposition of 2-electron 'zero-field' triplet product states

$$. |S_2\rangle = \frac{1}{\sqrt{3}}(|xx\rangle + |yy\rangle + |zz\rangle) \tag{3.7}$$

This state can also be written at 'high-field' as

$$|S_2\rangle = \frac{1}{\sqrt{3}}(|00\rangle - |T_+T_-\rangle + |T_-T_+\rangle) \tag{3.8}$$

These equations show how triplet pair states can have singlet character and how the $S_0 + S_1 \rightarrow (T_1T_1)$ can proceed rapidly and can occur without a spin flip. This is how singlet fission can be a much more rapid way of generating triplets than intersystem crossing because spin is conserved throughout the process. Jon Burdett et al. saw evidence that these triplet pair superposition states were formed at both zero and high magnetic field by during the singlet fission process through 'quantum beating' in the delayed fluorescence dynamics of tetracene crystals.[25] This is good experimental evidence that at 'zero-field' and at high-field, the states seen in Equations 3.7 and 3.8 are indeed the triplet pair states which are created through the singlet fission process and thus the states with singlet character. To understand the magnetic field effects that are seen in these experiments, we shall study how the triplet pair states change in terms of their singlet character and energy levels. To do this, we will begin in this 'zero-field' triplet pair basis $(|xx\rangle, |xy\rangle, |xz\rangle, ..., |zz\rangle)$ and study how these states evolve as a magnetic field is applied.

3.3 Magnetic Field Effects

As a magnetic field is applied to the triplet pair system, the energies and the singlet character of these states change with the intensity of the magnetic field. The following sections will show how this happens.

3.3.1 Quantum Mechanical Model

To study how the magnetic field changes the energies and the state character of the triplet states, we must first establish a Hamiltonian. The overall Hamiltonian we use can be broken into three distinct parts.

$$\hat{H}_{total} = \hat{H}_{B-field} + \hat{H}_{zero-field} + \hat{H}_{int} \tag{3.9}$$

where

$$\hat{H}_{B-field} = g\beta \left[h_z^A \hat{S}_z^A + h_z^B \hat{S}_z^B \right] \tag{3.10a}$$

$$\begin{aligned} \hat{H}_{zero-field} = D[(\hat{S}_z^A)^2 - \frac{1}{3}\hat{S^A}^2] + E[(\hat{S}_x^A)^2 - (\hat{S}_y^A)^2] \\ + D[(\hat{S}_z^B)^2 - \frac{1}{3}\hat{S^B}^2] + E[(\hat{S}_x^B)^2 - (\hat{S}_y^B)^2] \end{aligned} \tag{3.10b}$$

$$\hat{H}_{int} = X \hat{S}_A \hat{S}_B \tag{3.10c}$$

$\hat{H}_{B-field}$ is the magnetic field part of the Hamiltonian. The parameters were discussed earlier, but here it has been changed to include two triplet states, A and B with 4

total electrons. While in general, one must consider the effect of the magnetic field on the x and y axes as well, for simplicity we only consider the z axis. The same can also be said for $\hat{H}_{zero-field}$ which also now includes the terms for two triplets. Now there is an included triplet-triplet interaction term $\hat{H}_{int}$ which allows the two spins to interact with one another. This term is necessary to break degeneracies in the triplet pair states, but the exact nature of it is unclear at this time.

To identify the singlet character of a particular triplet pair state, it must be projected onto the singlet state of the four electron spin system. Using the 'zero-field' basis, it can be shown as

$$\langle S_2|\phi_l\rangle = \frac{1}{\sqrt{3}}(\langle xx| + \langle yy| + \langle zz|)\,|\phi_l\rangle = C_s^l \tag{3.11}$$

where ϕ_l is one of the nine triplet pair wavefunctions found after diagonalizing the Hamiltonian. When $h_z^i = 0$, we get three triplet pair states with a $|C_s^l|^2$ value of $\frac{1}{3}$ corresponding to the $|xx\rangle, |yy\rangle, and\, |zz\rangle$ states. As h_z^i is increased for both A and B, the system transitions to a case where only two of the triplet pair states have non-zero $|C_s^l|^2$. In the high-field basis, we see that the $|00\rangle$ state has a $|C_s^l|^2 = \frac{1}{3}$ and the $\frac{1}{\sqrt{2}}(|T_+T_-\rangle + |T_-T_+\rangle)$ state has a $|C_s^l|^2 = \frac{2}{3}$. Now it is apparent that one significant change of the magnetic field is that the system goes from three triplet pair states with singlet character at zero-field to two triplet pair states with singlet character at high-field.

3.3.2 Merrifield Kinetic Model

These same calculations can also be used to generate inputs for a kinetic model that predicts the overall rates of singlet fission and subsequent triplet fusion. In this section, we give an overview of the Merrifield kinetic model,[16,52] a model which was pioneered by R.C. Johnson and R.E. Merrifield. In the next chapter, we will present expanded models that will be used to analyze our own experimental data for singlet fission systems. In the model, we assume that the transition matrix element coupling the singlet to a specific triplet pair state $|\phi_l\rangle$ is proportional to C_s^l (l=1-9). The rate coupling the singlet to a specific triplet pair state l will be proportional to $|C_s^l|^2$

$$\text{Rate of Fission}(singlet \rightarrow |\phi_l\rangle) = k_{-2}|C_S^l|^2 \tag{3.12a}$$

$$\text{Rate of Fusion}(|\phi_l\rangle \rightarrow singlet) = k_2|C_S^l|^2 \tag{3.12b}$$

Note that $k_2 \neq k_{-2}$ in general. The use of the 2/-2 subscripts is to be consistent with the notation of earlier workers,[55,56] who reserved k_1/k_{-1} to describe triplet association processes that are important for fusion of free triplets created by $S_0 \rightarrow T_1$ excitation. The kinetic scheme for the populations of the singlet state N_{S_1}, the 9 possible triplet pair states $N_{(T_1T_1)_l}$, and the free triplets $N_{(T_1)}$, is

$$S_1 \underset{k_2}{\overset{k_{-2}}{\rightleftharpoons}} (T_1T_1) \underset{k_1}{\overset{k_{-1}}{\rightleftharpoons}} T_1 + T_1 \tag{3.13}$$

and is described by the following equations:

$$\frac{dN_{S_1}}{dt} = -k_{-2}\sum_{l=1}^{9}|C_s^l|^2 N_{S_1} + \sum_{l=1}^{9} k_2|C_s^l|^2 N_{(T_1T_1)_l} \tag{3.14a}$$

$$\frac{dN_{(T_1T_1)_l}}{dt} = k_{-2}|C_s^l|^2 N_{S_1} - \left(k_2|C_s^l|^2 + k_{-1}\right) N_{(T_1T_1)_l} + k_1 N_{T_1}^2 \tag{3.14b}$$

$$\frac{dN_{T_1}}{dt} = 2k_{-1}\sum_{l=1}^{9} N_{(T_1T_1)_l} - k_1 N_{T_1}^2 \tag{3.14c}$$

Previous workers, not being able to directly observe the $N_{(T_1T_1)_l}$ and N_T species, realized that they could simply remove the intermediate $N_{(T_1T_1)_l}$ population from the problem by assuming steady state conditions $\frac{dN_{(T_1T_1)_l}}{dt} \approx 0$. They could then explicitly solve for the time-dependence of the S1 and T1 populations, finding

$$\frac{dN_{S_1}}{dt} = -\gamma_S N_{S_1} + \gamma_T N_{T_1}^2 \tag{3.15a}$$

$$\frac{dN_{T_1}}{dt} = 2\gamma_S N_{S_1} - \gamma_T N_{T_1}^2 \tag{3.15b}$$

where

$$\gamma_S = \sum_{l=1}^{9} \frac{k_{-2}|C_S^l|^2}{1+\varepsilon|C_S^l|^2} \tag{3.16a}$$

$$\gamma_T = \frac{1}{9}k_1 \sum_{l=1}^{9} \frac{\varepsilon|C_S^l|^2}{1+\varepsilon|C_S^l|^2} \tag{3.16b}$$

and $\varepsilon = \frac{k_2}{k_{-1}}$. These are the 'classical' results for SF, but it should be emphasized that they are derived under somewhat restrictive conditions and cannot describe the full time evolution of N_{S_1}, in particular the early-time decay that takes place before the equilibrium $N_{(T_1T_1)_l}$ population is established. Equations 3.15 show how the C_S^l singlet overlap coefficients are the key quantities for understanding magnetic field effects on SF kinetics. Note that if the intermediate (T_1T_1) states did not exist, the rates of N_{S_1} and N_{T_1} decays would not depend on C_S^l and there would be no magnetic field dependence. This is true as long as $\sum_{l=1}^{9} |C_S^l|^2 = 1$. This condition is equivalent to saying that the norm of the singlet vector is conserved under unitary transformations of the spin Hamiltonian, which is typically the case.

The Merrifield model provides a way to predict the kinetics of singlet fission and triplet fusion, subject to some approximations. As described in the previous section and shown in Equation 3.8, in the high-field there are three triplet pair states with equal singlet character. Thus one would naively expect to have the exact same situation as in the zero-field case: three triplet pair states, each with $|C_S^l|^2 = \frac{1}{3}$. But Merrifield realized that if $X \neq 0$ in Equation 3.10c, the presence of the $\hat{H}_{AB}$ term can break the degeneracy of the $|T_+T_-\rangle$ and $|T_+T_-\rangle$ states, generating two new superposition states,

$$|TT_\pm\rangle = \frac{1}{\sqrt{2}} \left(|T_+T_-\rangle \pm |T_-T_+\rangle \right) \tag{3.17}$$

As mentioned earlier, only $|TT_+\rangle$ has $C_S^l \neq 0$ in this new basis. One can now see that the combination of this kinetic model and the quantum mechanical model leads to fewer triplet states with singlet character . This in turn leads to decreased fission and fusion rates, with a concomitant increase in the prompt fluorescence (γ_S is smaller) and a decrease in the delayed fluorescence (γ_T is smaller). It should be emphasized, however, that different molecular arrangements can yield qualitatively different magnetic field effects which will be discussed in the following chapter.

Equations 3.15 were sufficient to analyze early experiments that measured the magnetic field effects on the prompt and delayed fluorescence signals, but those early experiments had some important limitations. Although the designations prompt and delayed suggest that their temporal behavior was measured, in reality prompt fluorescence referred to the total luminescence after direct excitation of the $S_0 \rightarrow S_1$ transition (proportional to $1/\gamma_S$), while delayed fluorescence was generated by excitation of the $S_0 \rightarrow T_1$ transition in the near infrared (proportional to $1/\gamma_T$).[20,57] In practice, the calculated dependence of γ_S and γ_T on magnetic field should mirror the observed dependence of the time-integrated fluorescence signals. The good correspondence between the calculated γ_S/γ_T dependence on B-field strength and orientation and the fluorescence signal observed after excitation of either the $S_0 \rightarrow S_1$ or $S_0 \rightarrow T_1$ transitions provided conclusive evidence for SF in tetracene.[17,18,58] But with the advent of modern time-resolved spectroscopic techniques, we are now in a position to examine the full time-dependence of the SF process and directly probe the formation

and relaxation of the (T_1T_1) intermediate. The signature of this intermediate may have been detected indirectly via optically detected magnetic resonance experiments on tetracene,[59] but without determining its kinetic properties.

3.3.3 Expanded Merrifield Kinetic Model

Here we present an expanded Merrifield kinetic model for three different molecular systems: tetracene, rubrene, and diphenylhexatriene. There will be a discussion of how and why the kinetic equations are customized for each case. These models will then be applied in Chapter 4.

Tetracene

Given the new information available from picosecond time-resolved fluorescence measurements, one goal of our work has been to extend the Merrifield model to describe how the fluorescence signal changes on all timescales. Suna provided a more detailed model of triplet fusion based on the density matrix,[60–62] but in this work we will continue with the kinetic approach. In this section, we extend our earlier model in order to take exciton diffusion into account, albeit in a crude way. The kinetic scheme is similar to one proposed by Bouchriha and coworkers[63] and is outlined in Figure 3.1. We consider two types of triplet pairs: associated and separated. We also consider a spin-lattice relaxation process, parameterized by k_{relax}, which only occurs in the separated pairs and serves to redistribute the population across the 9 possible

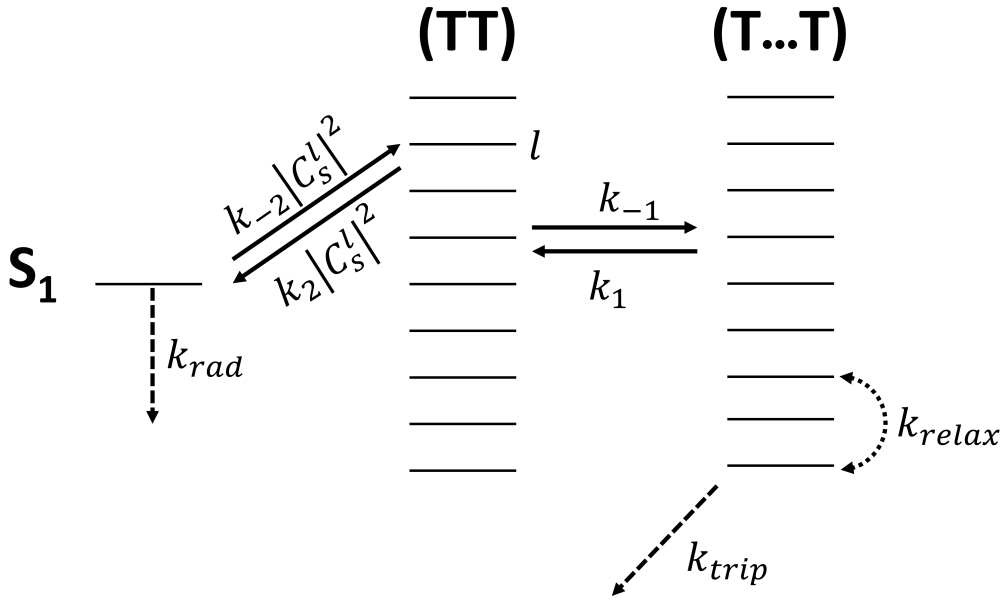

Figure 3.1: Schematic representation of the kinetic model. $(TT)_l$ refers to an associated triplet pair state while $(T\cdots T)$ refers to a spatially separated triplet pair state. This diagram only shows transfer rates to the l^{th} triplet, but transfer can occur between the singlet state and all of the triplet pair states. k_{rad} represents the radiative decay from the singlet states, k_{-2} and k_2 determine the fission and fusion rates, respectively and k_{relax} transfers population between the separated triplet pair states.

spin states. This kinetic model assumes that diffusion of the triplet excitons occurs on a timescale more rapid than spin relaxation. The kinetic equations are given below

$$\frac{dN_{S_1}}{dt} = -(k_{rad} + k_{-2})N_{S_1} + k_2 \sum_{l=1}^{9} |C_s^l|^2 N_{(TT)_l} \tag{3.18a}$$

$$\frac{dN_{(TT)_l}}{dt} = k_{-2}|C_s^l|^2 N_{S_1} - (k_2|C_s^l|^2 + k_-1)N_{(TT)_l} + k_1 N_{(T^{\cdots}T)_l} \tag{3.18b}$$

$$\frac{dN_{(T\cdots T)_l}}{dt} = k_{-1}N_{(TT)_l} - (k_1 + k_{trip} + k_{relax})N_{(T^{\cdots}T)_l} + \sum_{j\neq l} \frac{1}{8} k_{relax} N_{(T^{\cdots}T)_j} \tag{3.18c}$$

The rate constants are defined as follows: k_{rad} is the radiative rate, k_{-2} refers to the rate of fission, k_2 is the rate of fusion, k_{-1} is the rate at which triplets become spatially separated, k_1 is the rate at which triplets move into a distance at which fusion is possible, and k_{relax} is the rate at which a triplet pair state relaxes into other triplet pair states. Note that k_{relax} is only operative for the separated triplet pairs. This is equivalent to saying that the same processes that underly triplet exciton hopping also enable spin-lattice relaxation. The main difference between the model in Equation 3.18 and the standard Merrifield model is that the $k_{1/-1}$ processes in our model do not lead to free triplets that can recombine with any other triplet (which would give rise to a kinetic term proportional to N_{T1}^2) but instead describe the spatial separation of the geminate pair. These equations will be valid under low laser intensity conditions, where our experiments are typically performed. We will use this kinetic approach to model the magnetic field effect on the SF process in polycrystalline tetracene thin films. We choose this system rather than tetracene

single crystals because the quantum beats arising from spin state coherences are largely suppressed in the polycrystalline film,[25] possibly due to rapid spin relaxation at the surfaces of the crystallites.[64] This allows us to use a kinetic theory that considers only populations, rather than a more complicated density matrix that is required to take quantum coherences into account. The applications of this model will be discussed in Chapter 4.2

Rubrene

Next, we will address the disordered molecular system of rubrene. We first consider the early period of the fluorescence decay, commonly referred to as prompt fluorescence. During this period, the population exchanges between the singlet and triplet pair manifolds, but the correlated pairs do not interact with other triplets. We have previously shown that such correlated pairs can survive for at least 10 ns in room-temperature tetracene crystals.[25] The evolution of the early time fluorescence signal will be governed by the kinetics of the populations of the singlet state N_{S_1} and of the nine possible triplet pair states $N_{(TT)_l}$ as shown in Figure 3.2 and described by the following equations

$$\frac{dN_{S_1}}{dt} = -(k_{rad} + k_{-2}\sum_{l=1}^{9}|C_S^l|^2)N_{S_1} + \sum_{l=1}^{9} k_2|C_S^l|^2 N_{(TT)_l} \tag{3.19a}$$

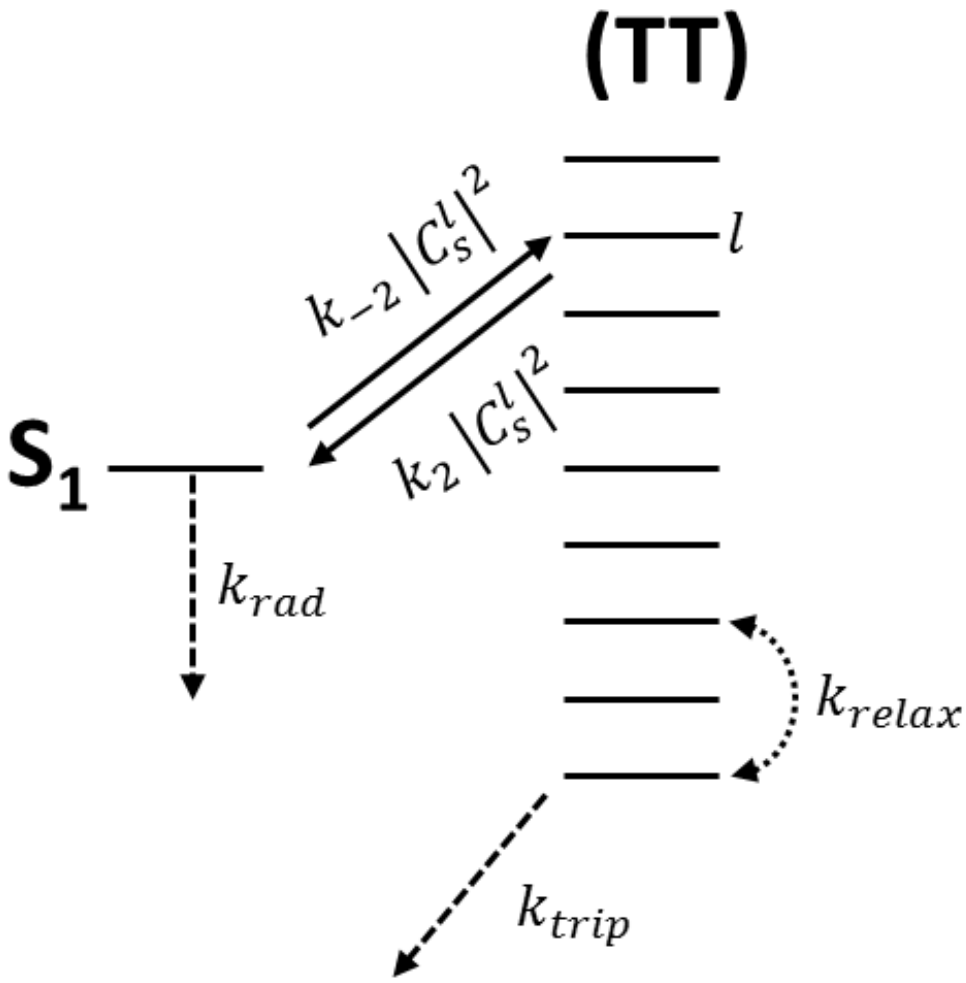

Figure 3.2: Schematic representation of the kinetic model. $(TT)_l$ refers to a geminate triplet pair state. This diagram only shows transfer rates to the lth triplet, but transfer can occur between the singlet state and all of the triplet pair states. k_{rad} represents the radiative decay from the singlet states, k_{-2} and k_2 determine the fission and fusion rates, respectively, k_{trip} allows for population loss from the triplet pair states, and k_{relax} transfers population between the triplet pair states.

$$\frac{dN_{(TT)_l}}{dt} = k_{-2}|C_S^l|^2 N_{S_1} - (k_2|C_S^l|^2 + k_{trip} + k_{relax})N_{(TT)_l} + \sum_{j\neq l} \frac{1}{8} k_{relax} N_{(TT)_l} \tag{3.19b}$$

The rate constants are defined as follows: k_{rad} is the radiative lifetime of the singlet state, k_{trip} is the intrinsic lifetime of the triplet state, k_{relax} is the rate of population transfer between triplet pair states (also known as the spinlattice relaxation rate), k_2 is the rate of triplet pair fusion back to the singlet, and k_{-2} is the rate of SF. Although we have assumed that S_1 decays only via k_{rad}, the inclusion of nonradiative decay pathways is trivial and would not affect our conclusions. Before making a detailed analysis, we first explore how eqs 3.19a and 3.19b behave in some simple limits that illustrate how changes in the quantum structure induced by a magnetic field can affect the kinetic behavior of the fluorescence.

The first important aspect of eqs 3.19a and 3.19b is that they predict that the initial decay of the S_1 state should be independent of the magnetic field strength. This is because the sum of singlet projections will always be unity, that is, $\sum |C_S^l|^2 = 1$, and thus changing individual C_S^l terms by changing the magnetic field only affects terms where the sum also runs over the l states, for example, the second term in eq 3.19a. This means that at very short times, before there is appreciable population in the $(TT)_l$ states, the fluorescence decay should be dominated by first-order kinetics of the form

$$\frac{dN_{S_1}}{dt} \cong -(k_{rad} + k_{-2}\sum_{l=1}^{9} |C_S^l|^2)N_{S_1} = -(k_{rad} + k_{-2})N_{S_1} \tag{3.20}$$

In other words, the effect of the magnetic field on the prompt fluorescence signal really comes after the triplet and singlet levels begin to equilibrate due to the competition between fission and fusion processes. At very early times, the decay should not depend on magnetic field at all. If only fission is occurring, with negligible fusion, then the transfer between the singlet and triplet levels is one-way and the k_2 fusion rate is negligible. In this case, no magnetic field effect on the singlet decay is expected on any time scale. This situation may hold in systems that undergo very rapid SF, for example, pentacene or the carotenoids, and where the triplets are not energetic enough to fuse back into the singlet.

However, if the magnetic field cannot affect the initial singlet decay, then what is the physical origin of the enhanced prompt due to the interplay of SF and TF rates at slightly later times and can be best illustrated if we assume that the S_1 and T_1 manifolds rapidly reach a quasi-equilibrium state, before triplet relaxation and radiative decay begin to play a significant role. We first define a simplified model, where there are M triplet pair states, each with equal singlet character $|C_S^l|^2 = 1/M$ and $k_{rad} = k_{trip} = k_{relax} = 0$. Note that changing the magnetic field will change M. We can now simplify eqs 3.19a and 3.19b in terms of the total triplet pair population $N_{tot} = \sum_{l=1}^{M} N_{(TT)_l}$.

$$\begin{aligned} \frac{dN_{S_1}}{dt} &= -k_{-2}N_{S_1} + k_2 \sum_{l=1}^{M} \frac{1}{M} N_{(TT)_l} \\ &= -k_{-2}N_{S_1} + k_2 \frac{1}{M} N_{(TT)}^{tot} \end{aligned} \tag{3.21a}$$

$$\frac{dN_{(TT)}^{tot}}{dt} = k_{-2}N_{S_1} - \frac{k_2}{M}N_{(TT)}^{tot} \tag{3.21b}$$

After the initial depopulation of the singlet state that occurs within the first nanosecond or so, we assume the system reaches a quasi-equilibrium with $(dN_{S_1}/dt) \cong 0$, which leads to an effective equilibrium constant for the reaction[23]

$$\frac{N_{S_1}}{N_{(TT)}^{tot}} = \frac{1}{M}\frac{k_2}{k_{-2}} \tag{3.22}$$

Thus the amount of singlet population available to generate fluorescence during this period is inversely proportional to the number of dark triplet pair states where the population can hide. This is the origin of the enhanced prompt fluorescence signal for oriented molecules in high magnetic fields. The magnetic field decreases M, the number of triplet pair states, and more population in the S_1 state leads to more fluorescence. If the molecules are randomly oriented, then the increased number of available triplet pair states will decrease the amount of fluorescence in this time regime. It should be emphasized that this treatment assumes that at early times the (TT) triplet pair produced by the SF event can be considered in isolation and the geminate triplets do not diffuse and interact with other triplets. This was backed up with a fluorescence power dependence measurement, shown in Chapter 4.3, which showed that the triplet fusion rate does not depend on density in this system. Applications of this model and the calculation of the $|C_S^l|^2$ values will be shown in Chapter 4.3.

Diphenylhexatriene

For diphenylhexatriene, the model that had been previously used for tetracene was employed with some minor changes. As before, we modify the Merrifield kinetic model to fit the magnetic field effects:

$$S^* \underset{k_2|C_s^l|^2}{\overset{k_{-2}|C_s^l|^2}{\rightleftharpoons}} [TT] \underset{k_1}{\overset{k_{-1}}{\rightleftharpoons}} [T\cdots T] \tag{3.23}$$

where $[TT]$ represents a closely associated triplet pair that can fuse back to the singlet state S*, $[T\cdots T]$ represents spatially separated triplets that cannot directly recombine, and $|C_s^l|^2$ represents the singlet overlap of the lth triplet pair state (out of 9 possible).[26,32] This model describes the low intensity regime where nongeminate recombination is negligible. In order to accurately reproduce the size of the magnetic field effect, we included a magnetic-field-dependent spinlattice relaxation rate, k_{relax}, that decreases by a factor of 10 at high magnetic fields. The kinetic equations used to simulate the fluorescence decays are given by

$$\frac{dN_{S_1}}{dt} = -(k_{rad} + k_{-2})N_{S_1} + k_2 \sum_{l=1}^{9} |C_S^l|^2 N_{(TT)_l} \tag{3.24a}$$

$$\frac{dN_{(TT)_l}}{dt} = k_{-2}|C_S^l|^2 N_{S_1} - (k_2|C_S^l|^2 + k_{-1} + k_{relax})N_{(TT)_l} + \sum_{j\neq l} \frac{1}{8} k_{relax} N_{(TT)_j} \tag{3.24b}$$

$$\frac{dN_{(T\cdots T)_l}}{dt} = k_{-1}N_{(TT)_l} - (k_1 + k_{relax})N_{(T\cdots T)_l} + \sum_{j\neq l}\frac{1}{8}k_{relax}N_{(T\cdots T)_j} \tag{3.24c}$$

where k_{rad} is the radiative decay rate, k_{-2} and k_2 are the rates for fission and fusions, k_{-1} and k_1 are the rates for triplet separation and association (in terms of being too far away form each other or close enough for fusion of triplets to occur), and k_{relax} accounts for spin-lattice relaxation, which allows the triplet population to redistribute across all triplet pair states. Unlike in the tetracene model, spin-lattice relaxation is allowed for associated triplet pairs. Chapter 4.4 will detail the applications of this model.

Chapter 4

Applications

This chapter will detail how the theory of magnetic field effects discussed in the previous chapter can be applied to three different molecular systems: tetracene, rubrene, and diphenylhexatriene. There will be a thorough discussion of how magnetic fields affect the singlet character and energy levels of the triplet pairs in these systems, and an analysis of how the fluorescence lifetime is changed in each of these systems by showing how the Hamiltonian and the kinetic equations are customized for each case.

4.1 General Approach

The three systems were studied using generally the same approach. The overall Hamiltonian can be broken into three distinct parts.

$$\hat{H}_{total} = \hat{H}_{B-field} + \hat{H}_{zero-field} + \hat{H}_{int} \tag{4.1}$$

where

$$\hat{H}_{magnetic} = g\beta \left[h_x^A \hat{S}_x^A + h_y^A \hat{S}_y^A + h_z^A \hat{S}_z^A \right] + g\beta \left[h_x^B \hat{S}_x^B + h_y^B \hat{S}_y^B + h_z^B \hat{S}_z^B \right] \tag{4.2a}$$

$$\begin{aligned} \hat{H}_{zero-field} = D[(\hat{S}_z^A)^2 - \frac{1}{3}\hat{S^A}^2] + E[(\hat{S}_x^A)^2 - (\hat{S}_y^A)^2] \\ + D[(\hat{S}_z^B)^2 - \frac{1}{3}\hat{S^B}^2] + E[(\hat{S}_x^B)^2 - (\hat{S}_y^B)^2] \end{aligned} \tag{4.2b}$$

$$\hat{H}_{int} = X \hat{S}_A \hat{S}_B \tag{4.2c}$$

These equations were largely discussed in the previous chapter. To apply this to an experimental system, the magnetic field vector and the zero-field parameters D and E must be found. D and E were simply found from the results discovered by other researchers. The magnetic field vector used was different for each system based on its crystal packing structure. X, the triplet-triplet interaction energy, just set to be some non-zero positive number to break a degeneracy between high-field states. While it is clear from experiments that this interaction most likely exists, it is thought to be very small.

4.2 Tetracene

In this section, the theory discussed in the previous chapter will be applied to a crystalline samples of tetracene. The two major aspects of the system that will be discussed are how the applied magnetic field affects the 'quantum-beats' in the fluorescence decay of a single crystal of tetracene and how the applied magnetic field affects the dynamics of the fluorescence in a polycrystalline film of tetracene.

4.2.1 Magnetic field effects on energy levels and quantum beats

In order for the magnetic field to alter the 'quantum-beating' behavior of the system, it must alter the energies of the triplet sublevels. We first consider the quantum mechanical part of the problem, starting with the Hamiltonian for two molecules A and B (4 electron spins) in an external magnetic field B. The orientation of A and B are fixed by the crystal packing, while the orientation of the magnetic field is fixed by the position of the crystal between the poles of the magnet. In the case of tetracene, the crystal fine structure x^* and z^*-axes are located in the **ab** plane of the crystal, and we define the angle of rotation of the **ab**-plane in the magnetic field as shown in Figure 4.1. The overall Hamiltonian used is described by equation 4.1. Experimentally, it is much simpler to work with a single crystal of tetracene in its crystal axes as the single crystals tend to grow in thin sheets in the *ab*-plane therefore

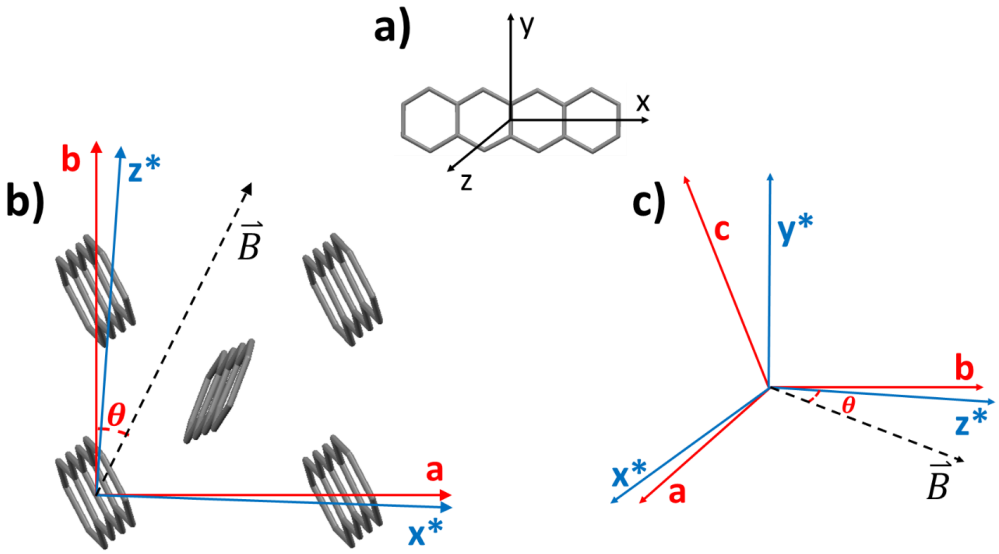

Figure 4.1: a) Tetracene labled with the molecular axes. b) A c-axis projection of the crystal lattice detailing the orientation of the magnetic field in the crystal axes(a and b) and the crystal fine structure tensor axes(x^* and z^*) θ indicates the angle from the b-axis in the **ab** plane. c) An illustration of the crystal axes and the crystal fine structure tensor axes superimposed on each other with the magnetic field in the **ab** plane.

making rotation in that plane trivial. With this in mind, we must first calculate the B-field in the crystal axis frame and then convert to the crystal fine structure tensor axis frame (x^*, y^*, z^*) where our Hamiltonian works. To find the B-field projections on the molecular crystal axes, we first calculate the projections of the magnetic field vector onto the crystal unit cell axes:

$$h_a^i = \mathbf{B}Sin(\theta^i) \qquad h_b^i = \mathbf{B}Cos(\theta^i) \tag{4.3}$$

where $\mathbf{B}$ is the strength of the magnetic field and the angle θ is shown in Figure 4.1. Once projected onto the crystal axes, the vectors are then projected onto the molecular axes using the following directional cosine table[56] to obtain the values for h_x^i,h_y^i,h_z^i:

	x^*	y^*	z^*
a	0.9634	0.2634	-0.0372
b	-0.0269	0.2463	0.9714
c	0.2663	-0.9330	0.2390

(4.4)

For example, in order to calculate h_x using the table values, take the linear combination of the a, b, and c vectors that equal the x^* axis. This table shows how the a,b, and c crystal axes, which were discovered by x-ray crystallography, rotate into the x^*, y^*, and, z^* frame, which are the calculated principle axes for the two molecule

unit cell. For this table, we find $x^* = 0.9634a - 0.0269b + 0.2663c$. The coefficients found in the table are the cosines of the angles between the related axes. Next, the zero-field part of the Hamiltonian is considered(Equation 4.2b). The only parameters which need to be varied here to suit tetracene are the D^* and E^* parameters. For these calculations, we use -0.0062 cm^{-1} and 0.0248 cm^{-1} respectively.[65] D^* and E^* are averaged zero-field parameters obtained after the rotation of the principle axes of each of the two molecules in the unit cell from the x,y,z axis frame to the x^*,y^*,z^* axis frame. Lastly, we include the interaction term, as seen in Equation 4.2c. This includes the spin-spin coupling term X which as mentioned before simply is included to break the degeneracy of triplet pair states.

The total Hamiltonian can be solved using either the zero-field basis or the high field basis. For this system, we will use the zero-field basis. We can project these new wavefunctions onto the singlet wavefunction to obtain their singlet character, given by

$$\langle S_2^{(4)}|\phi_l\rangle = \frac{1}{\sqrt{3}}(\langle xx| + \langle yy| + \langle zz|)\,|\phi_l\rangle = C_s^l \tag{4.5}$$

As previously mentioned, if B=0, there are only three zero-field triplet pair states that have equal values for C_s^l, i.e. the $|xx\rangle$, $|yy\rangle$, and $|zz\rangle$ states (each with a different energy). At high field, in the absence of $\hat{H}_{AB}$, there are again three states with equal singlet character: the $|00\rangle$,$|+-\rangle$, and $|-+\rangle$ states. The $|+-\rangle$ and $|-+\rangle$ states are degenerate, while the energy difference between the and states depends on the

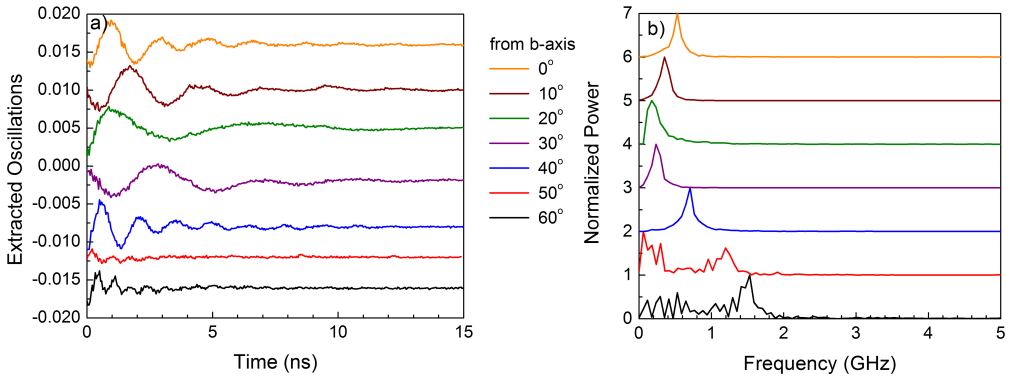

Figure 4.2: a) Oscillatory component of the experimental time resolved delayed fluorescence data taken with various B-field angles θ. b) Fourier transform power spectra of the oscillations in part a)

angle θ. Previous workers used first order perturbation theory (where $\hat{H}_{zero}$ is the perturbation) to estimate this energy splitting as

$$\Delta E_{00/+-} = 3D^* \left(cos^2\theta - \frac{1}{3} \right) + 3E^*(cos^2\alpha^* - cos^2\beta^*) \tag{4.6}$$

where α^*, β^* and θ^* are the angles between the magnetic field and the fine structure tensor axes x^*, y^*, and z^* respectively. Given θ and the cosine table in Equation 4.4, one can find h_x^* and h_y^* and then extract the angles α^*, β^* and θ^*. In other words, θ uniquely determines these angles, although writing the full θ dependence of Equation 4.6 would result in a very cumbersome expression. For tetracene, we expect the three distinct quantum beat frequencies observed at zero-field to collapse to one quantum beat frequency whose dependence on angle θ can be deduced from Equation 4.6. Indeed, this is what is observed experimentally for a subset of angles

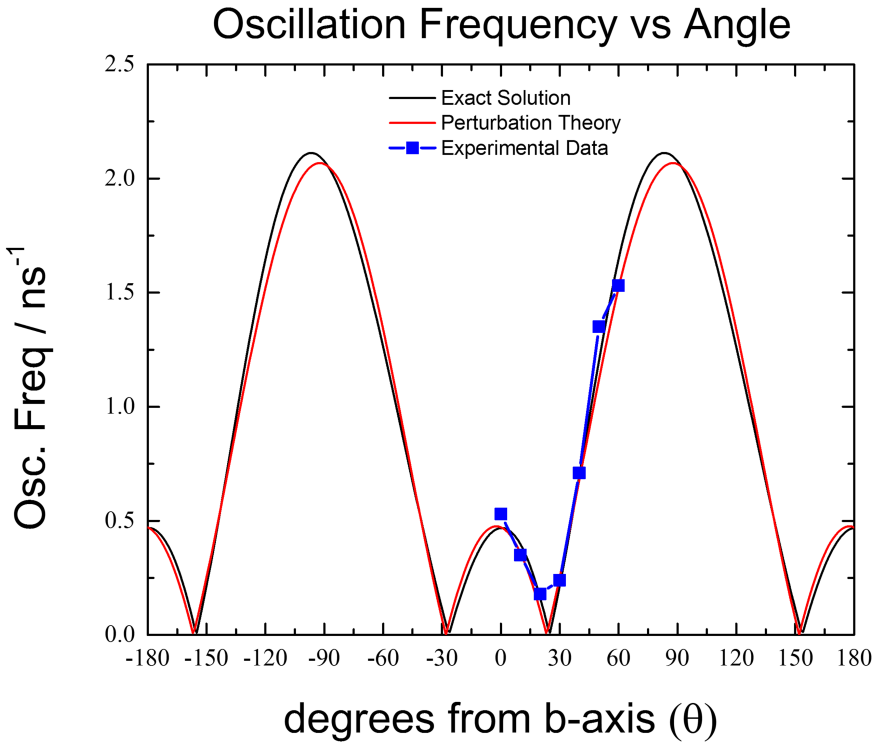

Figure 4.3: Plot of oscillation frequency of the quantum beats from versus the angle of the B-field relative to the crystal **b**-axis. Also shown are the calculated frequencies from perturbation theory(Equation 4.6) and an exact calculation obtained by diagonalizing the full spin Hamiltonian in Equation 4.1

θ = 0°-60°, as shown in Figure 4.2. The experimental oscillatory component of the delayed fluorescence signal, over a 15 ns interval, is shown for seven different crystal orientations in the B-field. The Fourier transforms of these signals are shown in Figure 4.2b. In Figure 4.3, we plot the oscillation frequency as a function of crystal angle, along with the theoretical prediction obtained by both numerical diagonalization of and by using the perturbation expression given in Equation 4.6. In the limit of

high magnetic field strength (B$> 10^3$ Gauss), the frequencies predicted by the exact solution and by Equation 4.6 agree quantitatively.

4.2.2 Kinetic modeling of the magnetic field effects

Using the kinetic model described in Chapter 3, our first task is to determine the C_s^l coefficients that are needed to fix the relative transition rates between singlet and triplet pair states. The sample is assumed to consist of a mosaic of small crystallites, all of which have their **ab** planes oriented parallel to the plane of the substrate, but randomly rotated with respect to the magnetic field. The C_s^l coefficients are calculated by solving the Hamiltonian in Equation 4.1 for different crystal orientations. Once the nine $|C_s^l|^2$ values have been calculated for a specific orientation of the crystal in the magnetic field, the angle is rotated and another set of $|C_s^l|^2$ values is calculated for the new orientation. To illustrate how $|C_s^l|^2$ changes with crystal angle, in Figure 4.4 we show $|C_s^l|^2$ values for all nine triplet pair states as the magnetic field is increased from 0 to 800 Gauss for three different orientations of the tetracene **ab**-plane with respect to the B-field. We chose the angles 18.8°, 23.8°, and 28.8° to illustrate how the number of triplet pair states with singlet character changes as the crystal angle varies. At 18.8°, the expected 3→2 change in the number of triplet pairs with singlet character is observed. At 28.8°, we again have the 3→2 evolution, but the relative amplitudes of states 4 and 6 have been reversed. This reversal occurs at 23.8°, where the $|00\rangle$ and $|T_+\rangle$ states become degenerate. At this point, there is only one state with

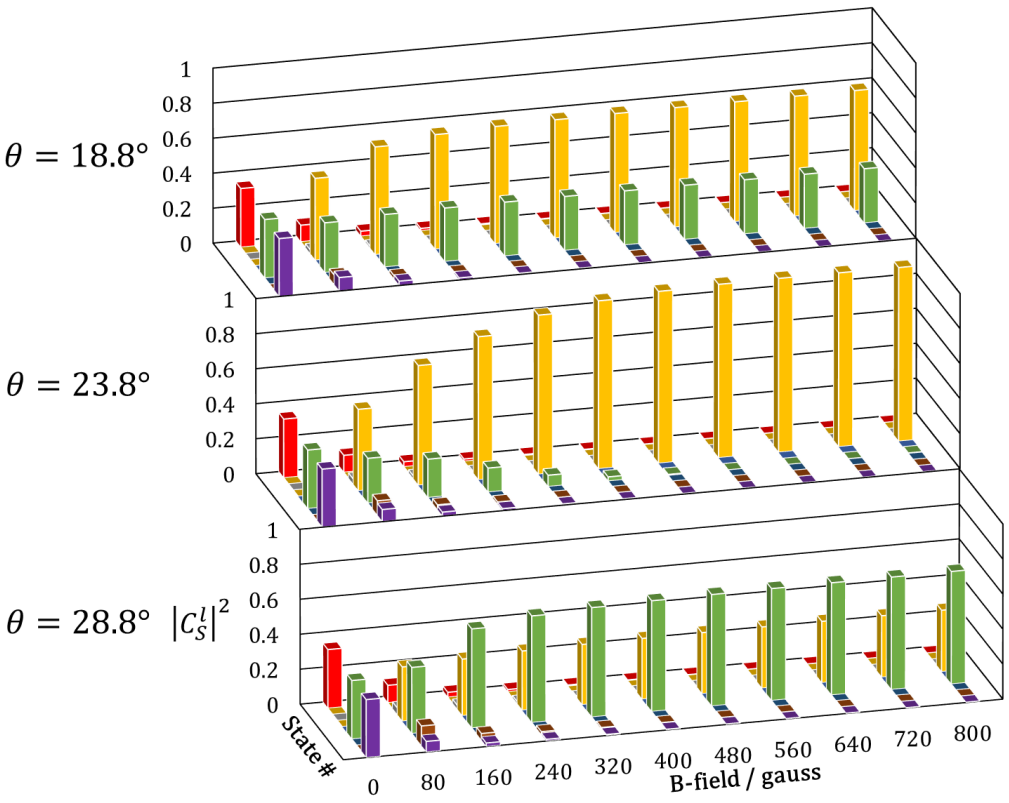

Figure 4.4: Histograms of singlet character (vertical axis) for each of the 9 triplet pair states as a function of magnetic field strength (long horizontal axis). The triplet pair states are ordered from lowest to highest energy. The three θ values correspond to the angle of the crystal **b**-axis with respect to the B-field.

singlet character at high field. With only one state, rather than two, participating in the SF/TF processes, we would expect to see a significant effect on the fluorescence kinetics, as discussed previously. If we were studying a single crystal, we would expect to see a narrow peak in the fluorescence intensity at this angle, as many previous workers have.[17,18,56,58] However, here we are concerned with the polycrystalline film, where we average over all angles and the B-field induced changes in the fluorescence dynamics are dominated by the 3→2 change in states with single character.

The C_s^l coefficients are used as inputs to scale the transition rates between the singlet and triplet pair states. The rate constants k_2 and k_{-2} are fixed, as are the other kinetic parameters. In order to use the $|C_s^l|^2$ values as inputs for the kinetic calculations, we have two choices. One can simply sum over the energy-ordered $|C_s^l|^2$ values for all orientations in order to get a set of nine averaged $|C_s^l|^2$ values, which were used as inputs for a single kinetic calculation. A more rigorous calculation would involve performing individual kinetic calculations for each orientation and then summing up all these time-dependent contributions to obtain a total $N_{S_1}(t)$ signal. We use the latter approach for the simulations here, since it is physically more reasonable to assume that the triplet dynamics occur within single crystal domains, and that the total fluorescence is given by a sum over signals emanating from all these domains. In Figure 4.5a, we show the experimental fluorescence decay in a 1 ns window, with and without an applied B-field. In order to simulate the observed fluorescence decays, we solved Equations (21) using the parameters summarized in Table 4.1 and plot

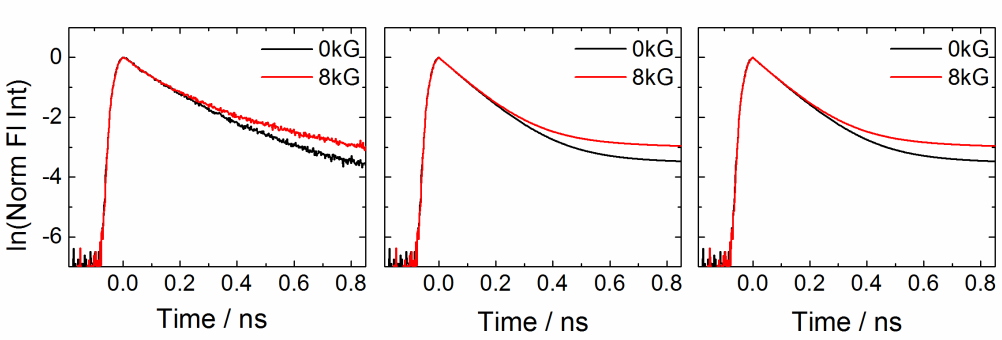

Figure 4.5: a) Experimental fluorescence decay in the 1ns window without magnetic field (black) and with an 8 kG magnetic field (red). b) Simulated fluorescence decay displaying the magnetic field effect using the model given in Figure 3.1 with k_{relax}=0.3 ns^{-1}. c) Simulated fluorescence decay displaying the magnetic field effect using the model given in Figure 3.1 with k_{relax}=0

the results in Figures 4.5b (k_{relax}=0.3 ns^{-1}) and 4.5c (k_{relax}=0 ns^{-1}). Both the experimental and simulated signals indicate that the initial decay of the fluorescence, over the first natural log within the first 200 ps or so, is not sensitive to the magnetic field. This is because the initial decay of the singlet, before any triplet pair states are significantly populated, is given by

$$\frac{dN_{S_1}}{dt} \cong -\left(k_{rad} + k_{-2}\sum_{l=0}^{n}|C_s^l|^2\right)N_{S_1} = -\left(k_{rad}+k_{-2}\right)N_{S_1} \tag{4.7}$$

where the last equality arises from the conservation of the norm of the singlet state under unitary transformation, as discussed earlier. Additionally, this simple theory predicts that if there is no population transfer from the triplet states back into the singlet state (k_2=0), then Equation 4.7 becomes exact and no magnetic field effect on the singlet decay is expected. Of course, the triplet pair states may equilibrate with

Table 4.1: Kinetic parameters used in Equation 3.18 to model the data in Figures 4.5 and 4.6

Kinetic Parameters / ns^{-1}						
k_{rad}	k_{-2}	k_2	k_{-1}	k_1	k_{relax}	k_{trip}
0.18	9.3	1.0	0.2	0.1	0.3	0.004
Energetic Parameters / cm^{-1}						
D^*	E^*	X_{int}				
-0.0062	0.0248	0.001				

other types of singlet states, for example charge-transfer states that eventually give rise to free carriers, and the B-field may affect different observables that are sensitive to such states. The important point is that in order to see magnetic field effects, some form of back-and-forth population transfer between the triplet pair states and another state with singlet character is required, and this two-way transfer requires some time to become established. At longer times, after ∼200 ps, the singlet and triplet pair states are both populated and one begins to see an enhanced prompt fluorescence signal under the applied B-field. In the 1 ns time window, the signal is most sensitive to k_{-2} and k_2. k_{-2}=9.3 ns^{-1} is determined by the initial decay rate of the fluorescence and is the same as that reported in previous work on polycrystalline tetracene thin films.[24,66–69] The fusion rate k_2=1 ns^{-1} is an order of magnitude slower than k_{-2}, consistent with the results of our experiments on single crystal tetracene delayed fluorescence.[25] These values give a reasonably good representation of the observed signal shape, where the initial exponential decay crosses over to a slower decay due to the replenishment of the singlet population via TF. The enhancement of the prompt

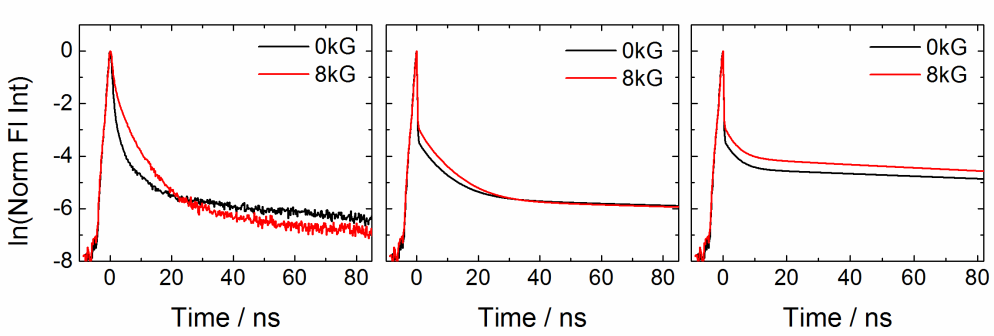

Figure 4.6: Experimental fluorescence decay in the 100ns window without magnetic field(black) and with an 8 kG magnetic field (red). b) Simulated fluorescence decay displaying the magnetic field effect using the model given in Figure 3.1 with k_{relax}=0.3 ns^{-1}. c) Simulated fluorescence decay displaying the magnetic field effect using the model given in Figure 3.1 with k_{relax}=0.

fluorescence in this time range reflects the fact that at high field there are only two triplet pair states for the population to partition into, and thus an average of $\frac{1}{3}$ of the population resides in the emissive singlet state, rather than $\frac{1}{4}$ as in the zero-field case. The triplet pair feedback into the singlet state in this time regime leads to an enhanced fluorescence signal that partially cancels out the rapid decay that would be observed if only SF were operative. The simulated signals for both k_{relax}=0.3 ns^{-1} and k_{relax}=0 are very similar in this time window, which is not surprising since the timescale of separation and spin-lattice relaxation are both longer than 1 ns. The longer time fluorescence decay dynamics are more sensitive to the TF and exciton diffusion rates. Figure 4.6a shows the experimental fluorescence decays, while Figures 4.6b and 4.6c show the simulated curves using the parameters in Table 4.1. The k_1/k_{-1} rates determine the level of the delayed fluorescence signal, since they limit the ability of the separated triplets to recombine. In Table 4.1, the separation rate

k_{-1}=0.2 ns^{-1} is a factor of 2 greater than the association rate, k_1=0.1 ns^{-1}, reflecting the fact that association is less likely as the excitons diffuse apart. These two values are chosen to make the level of the simulated delayed fluorescence comparable to the experimental level. The value of k_{relax} does not have a strong effect on the absolute magnitude of the delayed fluorescence signal. It does, however, influence the crossing of the high-field and zero-field decay curves, seen experimentally at around 20 ns delay, where the high-field delayed fluorescence signal dips below the level of the zero-field delayed fluorescence. In Figure 4.6b, the simulated signal for k_{relax}=0.3 ns^{-1} shows the convergence of the two curves on this timescale, whereas in Figure 4.6c the curves for k_{relax}=0 remain well-separated. We were unable to reproduce the more pronounced crossing seen in the experimental data, however, suggesting that this model needs further refinement.

From a physical standpoint, the suppression of the delayed fluorescence signal in the high-field case is related to the fact that the triplet pairs can randomize their spin populations on longer timescales. Once the triplets become distributed across the nine possible spin states, at high-field there are only two channels back to the singlet ($|00\rangle, |T_+\rangle$) rather than the three available at zero-field ($|xx\rangle$,$|yy\rangle$,$|zz\rangle$). Note that if k_{relax}=0, and the triplet pairs are not allowed to randomize their spin states, then the separated pairs are always trapped in states with singlet character and it does not matter whether there are two or three such states. In this case, changing the number of singlet gateway states using the magnetic field has no effect on the TF

rate and no crossing of the high- and zero-field decay curves is observed in Figure 4.6c. If, on the other hand, we turn on k_{relax} and allow population to redistribute across all triplet pair states, then the decreased number of gateway states at high B-field will suppress TF and decrease the amount of delayed fluorescence as seen in Figure 4.6b. In a previous paper,[32] we only considered associated triplet pairs, and in that case the combination of rapid fusion and radiative loss from the singlet state could also cause a curve crossing, even if k_{relax}=0. The problem with that treatment is that we had trouble describing the highly nonexponential character of the decay curves. In this paper, by taking diffusion into account using associated and separated pairs, we postulate a different mechanism where spatial separation of the triplets is accompanied by spin relaxation. This model gives a more accurate representation of the data, although the match is still not exact. Discerning the precise role of spin relaxation using fluorescence measurements alone is probably asking too much of a single technique, and in the future we hope to utilize other types of experimental methods to gain a fuller picture of the triplet exciton dynamics after the SF event.

In this section, we have tried to extend the work of pioneering researchers like Merrifield, Suna, Pope and Swenberg to look at both the mechanism of SF and how it is affected by the presence of a magnetic field.[17,19,21,52,56,60] Direct evidence that SF produces the theoretically predicted triplet superposition state is provided by the observation of quantum beating in the delayed fluorescence of tetracene crystals. The dependence of both the quantum beat frequencies and the fluorescence decay rates on

magnetic field and crystal orientation are consistent with the predictions of a quantum mechanical model that takes the detailed spin Hamiltonian into account. The magnetic field also affects the kinetics of the SF/TF processes, which we can understand in terms of an expanded Merrifield model. This model allows us to make several qualitative observations. First, when the full time-dependence of the singlet population is considered, we find that the magnetic field has no effect on the very initial fluorescence decay rate, but only becomes observable at later times when the triplet pair states begin to equilibrate with the singlets. This implies that the existence of a magnetic field effect on the singlet decay depends on the exchange of population back and forth between the singlet and triplet pair states. If this exchange is not possible, e.g. due to energetic mismatches, then the absence of a magnetic field effect does not necessarily rule out the presence of SF. Second, the longer time behavior of the fluorescence decay reflects association and separation of the triplet pairs, along with the relaxation of the triplets into different spin states. In particular, our model suggests that the crossing point of the delayed fluorescence curves at high and zero-field is sensitive to the spin relaxation dynamics of the triplets.

4.3 Rubrene

4.3.1 Introduction

As in crystalline tetracene, most observations of SF have occurred in crystalline or polycrystalline samples, there have also been claims of SF in biological assemblies,[37,70] amorphous molecular films[33,71] and polymers.[72,73] Because the processing of amorphous materials tends to be less costly, the observation of efficient SF in such materials could bring it closer to practical applications. Recently, our group and others have studied exciton dynamics in crystalline tetracene, where SF occurs on a 50-200 ps time scale to generate triplet pair superposition states with overall singlet character.[23–25,69,74,75] Tetracene readily crystallizes under almost any preparation conditions at room temperature. It is possible to prepare amorphous films on substrates held at low temperatures, but these films tend to show strong excimerlike emission,[76] suggesting that rapid intermolecular charge transfer between pi-stacked molecules competes effectively with SF in such films. When phenyl groups are added to tetracene, for example, rubrene, it is less prone to crystallization, and amorphous films can be formed by vacuum evaporation and solvent casting. The singlet and triplet energies of rubrene are very similar to those of tetracene,[77] and SF has been documented in both single crystals[54,78,79] and in amorphous films.[80] Solid rubrene thus represents a system where the influence of intermolecular packing and disorder on SF can be investigated. In this chapter, we present a study of the photophysics

of highly disordered rubrene. We find that it is very difficult to eliminate all signs of excitonic coupling in evaporated thin films, finally turning to rapid spin coating to generate ultrathin films that are free of the spectral signatures of delocalization. By studying the temperature-dependent steadystate absorption and fluorescence spectral lineshapes, we confirm that these films do not exhibit the intermolecular excitonic effects seen in more crystalline materials like tetracene. The temperature-dependent fluorescence decays of the neat films are consistent with the dominant relaxation channel being a thermally activated SF process. To confirm the role of SF, we extend previous theories of magnetic field effects on SF and triplet fusion (TF) to simulate the room temperature fluorescence decays in orientationally disordered systems. We get good qualitative agreement between theory and experiment when we assume that the fission event occurs at ordered pairs within the neat film. Furthermore, our results suggest that the geminate triplets remain correlated with each other for > 100 ns, necessitating the use of a different model than that assumed by previous workers in the field. From a practical perspective, it is encouraging that SF can proceed efficiently in amorphous rubrene without the benefit of singlet delocalization or strong intermolecular coupling, albeit with a rate significantly slower than in crystalline tetracene.

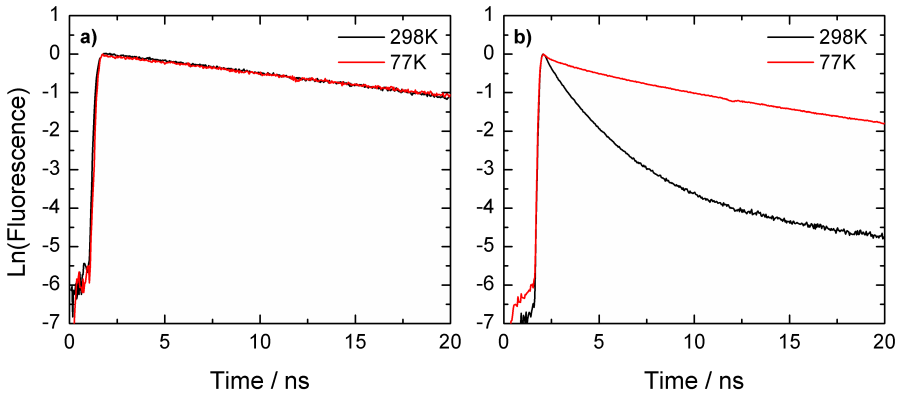

Figure 4.7: a) Normalized fluorescence decay of rubrene in polystyrene at 298 and 77 K. b) Normalized fluorescence decay of amorphous rubrene at 298 and 77 K.

4.3.2 Results

Time-Resolved Fluorescence

The time-resolved fluorescence is studied for evidence of singlet fission. For both isolated molecules and films, the fluorescence spectrum did not change over time ,indicating that in both systems the emission originates from a single species, namely, the excited singlet state. Isolated rubrene molecules have a high fluorescence quantum yield (0.98) and a very low yield for intersystem crossing to the triplet state ($< 1\%$).[77] The lack of activated nonradiative decay channels means that for rubrene molecules embedded in a polymer, one expects to see a temperature-independent decay whose lifetime is close to the radiative lifetime of the molecule. Indeed, this is what we observe. The fluorescence decays, integrated over the whole spectral range, at 298 and 77 K for rubrene in polystyrene are shown in Figure 4.7a. The single exponential decays allow us to extract a fluorescence lifetime at both temperatures of

Table 4.2: Exponential Fits to Time Resolved Fluorescence Decays

Amorphous Rubrene					*Rubrene in Polystyrene*		
	A1	τ_1/ns	A2	τ_2/ns		A1	τ_1/ns
298 K	0.475	0.226	0.525	2.22	298 K	1.00	16.4
77 K	0.226	1.11	0.774	6.89	77 K	1.00	16.3

16.3 ± 0.2 ns, which is close to the radiative lifetime of 16.5 ns for rubrene solution.[77] The fluorescence decays observed in our amorphous rubrene films are qualitatively different from those of the dilute samples, as shown in Figure 4.7b. At both 298 and 77 K, they are highly nonexponential, but there is considerable slowing of the decay at 77 K. When the room temperature decay in a 20 ns detection window is fit using a biexponential decay function, we obtain time constants of $\tau_1 = 0.23$ ns and $\tau_2 = 2.2$ ns. Note that the spectrum of the long-lived component is identical to that of the short-lived component. When the temperature is lowered to 77 K, the decay slows and becomes closer to a single exponential, with $\tau_1 = 1.1$ ns and $\tau_2 = 6.9$ ns. The decay times and amplitudes for both dilute rubrene in PS and the amorphous rubrene films in a 20 ns time window are summarized in Table 4.2. As discussed below, there is an even longer-lived component, but for all times the emission spectrum is identical to that of the prompt fluorescence.

The rapid fluorescence decay in amorphous rubrene suggests that a new non-radiative decay channel is present in the solid. The rapid decay of the initial fluorescence, followed by a long lived delayed fluorescence signal, is similar to what has been observed in polycrystalline thin films of tetracene.[24,69] Delayed fluorescence

due to TF has been observed in crystalline rubrene and extensively analyzed.[81,82] The most straightforward interpretation of rubrenes fluorescence dynamics is that, similar to tetracene, SF is occurring, followed by triplettriplet recombination that produces delayed fluorescence. On the basis of the singlet energy E(S_1) = 18 500 cm^{-1} and the triplet energy E(T_1) = 9200 cm^{-1} for molecules in solution,[83–85] both processes are expected to be facile at room temperature. If the SF process is thermally activated, then SF would be suppressed at lower temperatures and the prompt fluorescence decay would slow down, as observed experimentally in Figure 4.7, but whereas the temperature-dependent fluorescence decays are consistent with SF, they do not provide conclusive evidence. To provide additional confirmation that SF is occurring, we turn to the use of magnetic fields, which affect the wavefunctions of triplet excitons but leave singlets unaffected. Early workers developed the theory of how the rates of singlet⇌triplet pair processes (both SF and TF) are perturbed by magnetic fields.[16,52,60] The ability of magnetic fields to affect both the SF and TF rates allowed early investigators to deduce the presence of fission from changes in the fluorescence signal.[17,18,56,58] To confirm the presence of SF in amorphous rubrene, in the following, we will develop the theory of magnetic effects in a disordered system and show how they affect the time-resolved fluorescence dynamics.

Theory of Magnetic Field Effects in Disordered Systems

To analyze magnetic field effects in a sample of randomly oriented chromophores, we consider two independent molecules, with their own axis systems, labeled A and B, that can be oriented at any angle with respect to each other. When a magnetic field is applied, its orientation will have different projections in axis systems A and B. This situation is outlined in Figure 4.8. As with tetracene, the overall Hamiltonian as seen in Equation 4.1 will be used. Here the h_x^i, h_y^i, h_z^i terms in $\hat{H}_{magnetic}$ are given by

$$h_x^i = sin(\theta^i) \cdot cos(\phi^i) \qquad h_y^i = sin(\theta^i) \cdot sin(\phi^i) \qquad h_z^i = cos(\theta^i) \tag{4.8}$$

where the angles θ^i and ϕ^i are described in Figure 4.8. For $\hat{H}_{zero-field}$, the zero-field parameters for crystalline tetracene will be used.[65] These are $D = 0.0062$ cm^{-1} and $E = 0.0248$ cm^{-1}, which are the same as those of rubrene to within the experimental error.[53] It turns out that the actual values for D and E have no effect on the kinetics of SF and TF in the treatment that follows, as long as they are small relative to the energy shifts induced by the magnetic field (i.e., in the high-field limit). For example, we obtained identical results using the D and E parameters for molecular tetracene.60 Using the crystalline tetracene values, the high-field limit, where the triplet pair wave functions stop evolving with magnetic field strength, was achieved by $\sim$ 200 G. First, we again consider the case of two parallel molecules with their magnetic z-axes aligned

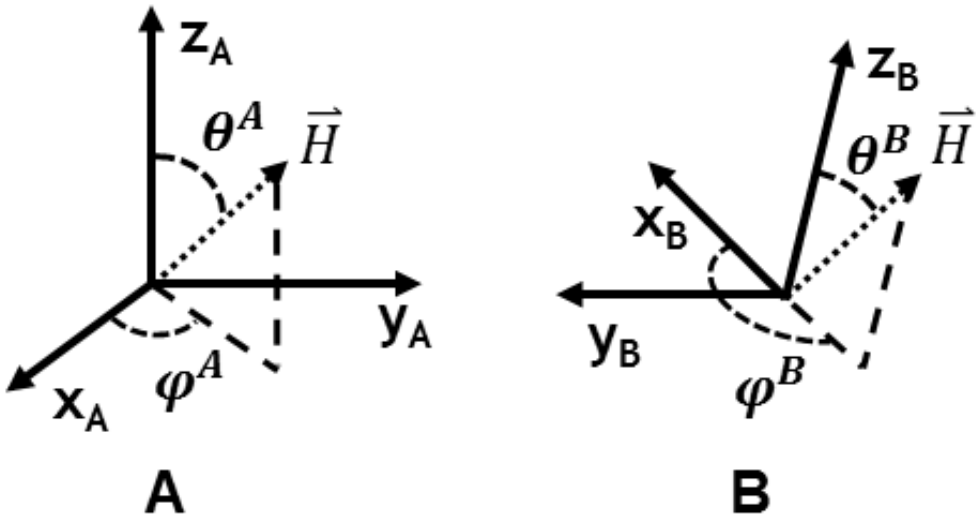

Figure 4.8: Schematic representation of the orientations of the magnetic axes of two independent molecules with respect to an applied magnetic field H. By rotating the axes of each molecule with respect to each other and the magnetic field, we can average over all possible orientations.

parallel to the magnetic field ($\phi^{(A,B)} = \theta^{(A,B)} = 0$). This situation, which is most relevant for the case of a polyacene crystal whose **ab** crystal plane is aligned between the poles of a magnet, is the one most commonly assumed when magnetic field effects are considered. The evolution of the singlet character for two parallel chromophores is shown in Figure 4.9a. As described in the previous chapter, the three states with equal singlet character at zero-field evolve into two states with a 2:1 ratio of $|C_S^l|^2$ at high field. At small field strengths, additional states temporarily gain singlet character before the two states $|00\rangle$ and $|TT_+\rangle$ become dominant. It is this transient opening of new states that leads to the enhancement of the SF rate at intermediate field strengths seen in the theoretical plots of the overall SF rate versus magnetic field strength by previous workers,[56] but it should be emphasized that if the two molecules are not

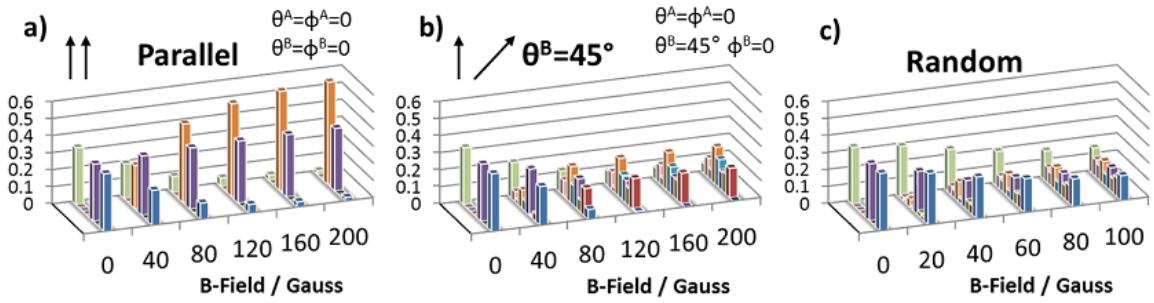

Figure 4.9: Singlet projections $|C_S^l|^2$ of each triplet pair state as a function of magnetic field strength for different molecular orientations. The parameters used in eq 1 are: D = -0.0062 cm^{-1}, E = 0.0248 cm^{-1}, X = 0.0001 cm^{-1}, and $g\beta/\hbar = 5x10^{-4}cm^{-1}gauss^{-1}$. a) For parallel molecules, the number of states with singlet character decreases from 3 to 2. b) For a 45° angle between molecules, the number of states with singlet character increases from 3 to 8. c) For a collection of randomly oriented molecular pairs, the number of states with singlet character increases from 3 to 9.

parallel, then the presence of the magnetic field can distribute singlet character over more than three triplet pair eigenstates, as shown in Figure 4.9b for $\theta^A = 0°$, $\phi^A = 0°$ and $\theta^B = 45°$, $\phi^B = 0°$. Swenberg and Geacintov[56] recognized the possibility that a collection of randomly oriented molecules could give rise to an enhancement of the SF/TF rates due to the presence of intermolecular arrangements like that in Figure 4.9b. Our numerical simulations confirm that a singlet⇌triplet processes should become more facile in a random system under application of a magnetic field. To model a randomly oriented amorphous sample, we obtain the singlet projection given by every possible orientation of the magnetic field with respect to both molecule A and molecule B, which in turn are randomly oriented with respect to each other. The sum of the singlet projections is then divided by the number of angles that were sampled to give the singlet projection averaged over all possible angles. As shown

in Figure 4.9c, the number of states with nonzero singlet character steadily increases from 3 to 9 as the magnetic field increases.

We now refer back to the model described in Chapter 3. At longer times, the relaxation of the triplet (k_{trip}) and singlet states (k_{rad}) cannot be neglected, and we must consider the full time evolution of eqs 3.21a and 3.21b. In Figure 4.10, we show a series of calculated curves for different values of M. The kinetic parameters used in Figure 4.10a are $k_{rad} = 0.06$ ns^{-1},k_{trip}=0ns^{-1}, $k_2 = 1$ ns^{-1}, and $k_{-2} = 1$ ns^{-1}. As predicted in the previous paragraph, as M decreases, the amount of prompt fluorescence is enhanced due to the increased partitioning of the population into the singlet state, but at longer times the delayed fluorescence for lower M values actually decays more rapidly. This can again be understood in terms of the increased partitioning of the population into S_1. More population in S_1 leads to greater signal at the beginning, but the total excited state population decays more rapidly due to the fact that the radiative decay from S_1 acts as a loss channel. Note that this will always be the case if the singlet decay is more rapid than the triplet decay. If the reverse were true, then the decay of the delayed fluorescence would get slower as M increases. In most cases, however, the triplet state is longer lived than the singlet state and Figure 4.10a should provide a better qualitative guide.

For parallel chromophores, increasing the magnetic field decreases M and the delayed fluorescence should decay more rapidly, leading to a crossing of the curves at high ($M = 2$) and zero ($M = 3$) fields, as shown in Figure 4.10a. For randomly

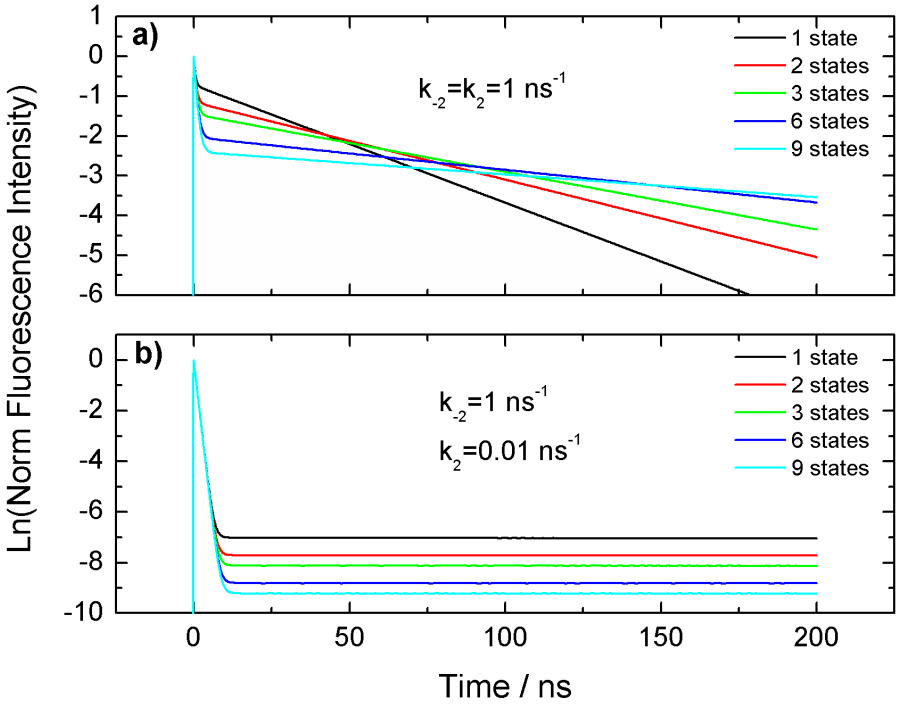

Figure 4.10: Simulated fluorescence decays for different numbers of triplet pair states with singlet character (M in eqs 3.21a and 3.21b). For all simulations, $k_{trip} = k_{relax} = 0$. a) $k_{rad} = 0.06$ ns^{-1} , $k_2 = 1$ ns^{-1} , and $k_{-2} = 1$ ns^{-1} . Note that when k_2 (fusion) and k_{-2} (fission) rates are comparable, fluorescence decays with lower M values cross those with higher M values as enhanced prompt fluorescence gives way to more rapidly decaying delayed fluorescence. b) $k_{rad} = 0.06$ ns^{-1} , $k_2 = 0.01$ ns^{-1} , $k_{-2} = 1$ ns^{-1} . When $k_{-2} \gg k_2$, we only see enhanced delayed fluorescence levels when M decreases because the singlet population at any given instant is higher.

oriented chromophores, increasing the magnetic field should increase M and lead to the opposite effect: less prompt fluorescence but a slower delayed fluorescence decay because more population can hide in the triplet manifold. The decay curves at high (M = 9) and zero (M = 3) fields still cross but from the opposite direction as compared with the parallel case. Finally, we emphasize that the simulations in Figure 7a have assumed equal fission and fusion rates, that is, $k_{-2} = k_2$. If fusion is much slower than fission, then the equilibration between singlet and triplet manifolds cannot be complete until much later. In Figure 4.10b, we show how the fluorescence decay changes with M when fusion is much slower than fission: $k_{rad} = 0.06$ ns^{-1},$k_{trip} = 0.0$ ns^{-1}, $k_2 = 0.01$ ns^{-1}, and $k_{-2} = 1$ ns^{-1}. In this case, the effect of M on the prompt fluorescence has vanished, we are back in the limit described by eq 3.20. The equilibrium described by eq 3.22 holds only after 100 ns. At longer times, smaller M values lead to a higher apparent delayed fluorescence signal. Furthermore, because k_2 is small, the loss of triplet population due to fusion and subsequent radiative decay due to k_{rad} is smaller and the delayed fluorescence decay is much slower, appearing flat in the 200 ns time window.

Analysis of Rubrene Fluorescence Decay

We confirmed that the presence of the magnetic field had no measurable effect on the fluorescence decay of the rubrene/ polystyrene sample, as expected. In Figure 4.11, we show the experimental rubrene fluorescence decay in three time windows: 1,

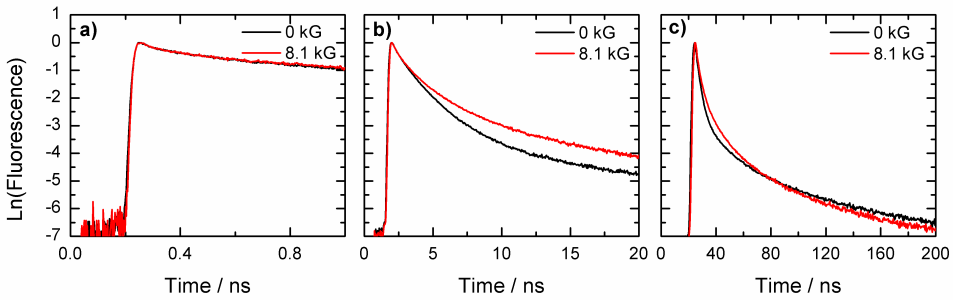

Figure 4.11: Time-resolved fluorescence decays of amorphous rubrene displaying the magnetic field dependence in the a) 1, b) 20, and c) 200 ns windows. The lack of effect in the 1 ns window is followed by an enhanced prompt fluorescence in the 20 ns window, whereas the 200 ns window shows that this enhancement changes to a decrease in the long-lived delayed fluorescence near 80 ns.

20, and 200 ns both with and without an applied magnetic field. Application of a 8.1 kG magnetic field to the neat film resulted in several noticeable changes in the fluorescence decay. The initial decay (<1 ns) was largely unaffected by the magnetic field, as shown in Figure 4.11a, as expected based on eq 3.20. At slightly later times (120 ns), there is a clear increase in the fluorescence signal due to increased population in the S_1 state, as predicted based on eq 3.22 if M decreases in the high magnetic field. At much longer times, the delayed fluorescence decay in the magnetic field is more rapid than the zero-field case and the curves cross at ∼100 ns, again as expected if M decreases in a magnetic field. Thus our overall signal shape is qualitatively consistent with what is expected based on the oriented picture of SF, in contrast with our expectations for a random system. The total fluorescence decay in zero-field on all time scales can be parametrized using a triexponential decay with amplitudes and time constants summarized in Table 4.3. In the following analysis, we will not

Table 4.3: Parameters from Triexponential Fit

A1	τ_1/ns	A2	τ_2/ns	A3	τ_3/ns
0.171	0.226	0.820	2.22	0.009	50.0

attempt to analyze the small, rapid component with $\tau_1 = 0.23$ ns, but assume that $\tau_2 = 2.2$ ns reflects the SF time for the majority of the singlet excitons. Note that the delayed fluorescence extends beyond the 200 ns time window, which was the longest used in our experiments. This provides a lower bound for the triplet lifetime in our samples, but the actual lifetime is expected to be longer because it has been measured to be 20 µs in single crystals of rubrene.[82] Before trying to simulate the data in Figure 8, we first note that calculations based on the simplified kinetic model in eqs 3.21a and 3.21b capture the main features of the fluorescence signal with consideration of only geminate pair triplets. The Merrifield model used a three-state model of the following form to analyze magnetic field effects on the fluorescence.[52,56,60]

$$S_1 \rightleftharpoons (T_1T_1) \rightleftharpoons T_1 + T_1 \tag{4.9}$$

In this model, the $T_1 + T_1$ state implies that the triplets are uniformly distributed in space. In this limit, the probability that a triplet will recombine with its twin is equal to the probability that it will recombine with a triplet exciton spawned by a completely separate photon absorption event. If this is the case, then the signal shape will change as the excitation density is increased: the amount of prompt fluorescence should increase linearly, whereas the delayed fluorescence, dominated by encounters

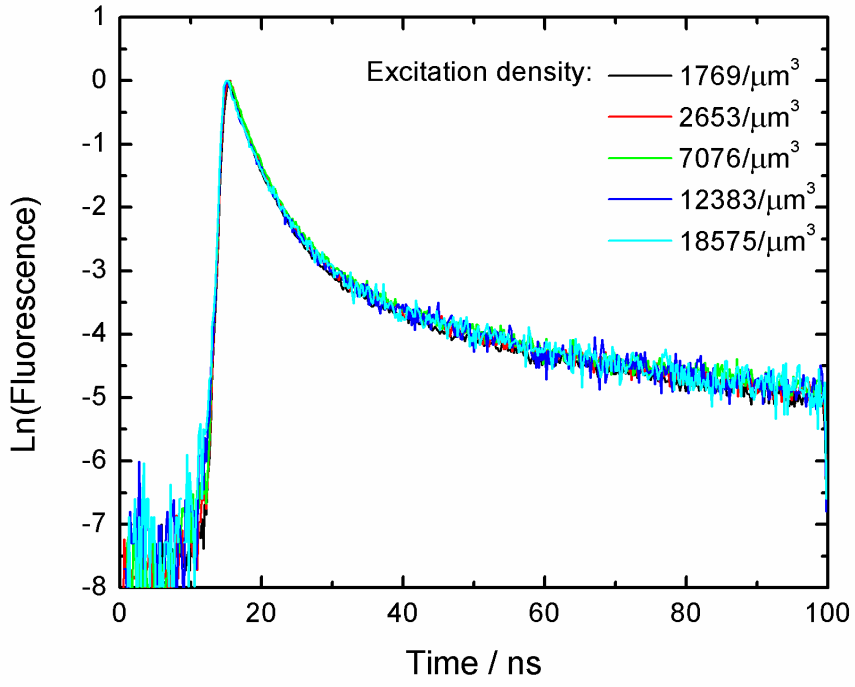

Figure 4.12: Fluorescence decay of amorphous rubrene at different excitation densities. The decay shape does not depend on laser power, which indicates that only geminate pair triplets play a role in the dynamics on this time scale.

between triplet excitons created by separate photons, should increase approximately quadratically, as observed previously in tetracene thin films,[69] but at very low excitation densities, only geminate (formed from the same singlet) triplets are expected to contribute to the signal. To test whether nongeminate triplets play a significant role in our amorphous samples, in Figure 4.12, we show the total fluorescence decay in a 100 ns window for excitation densities ranging from $1.8x10^3$ to $1.9x10^4$ µm^{-3}. These excitation densities were calculated as done previously for tetracene,[24] and they result in an average distance between excitation of 89 and 34 nm, respectively.

The similarity of the decay curves in this fluence range suggests that recombination of nongeminate triplets makes a negligible contribution to the signal on the 100 ns time scale. Further evidence that we are not in the uniform triplet density regime is provided by a log-log plot of the fluorescence decay. Of course, on microsecond time scales, the triplets become uniformly distributed and one expects to see the bimolecular reaction kinetics seen in rubrene crystals.[82]

Because nongeminate triplets do not appear to play an important role in the dynamics in amorphous rubrene, we concentrate on the kinetic scheme given in Figure 3.2. To quantitatively model our fluorescence signal, we undertake a more complete analysis using eqs 3.19a and 3.19b. The rate constants are defined as previously, and we assume all of the population starts in the singlet state with the experimentally measured excitation density. We then numerically solve eqs 3.19a and 3.19b and assume the fluorescence signal is proportional to N_{S_1}. Our simulations of the data are designed to address two issues. The first concerns the relative orientation of the two chromophores that participate in SF. As shown in Figure 4.10, our data are qualitatively consistent with the magnetic field decreasing the number of triplet pair states with singlet character. In Figure 4.13a, we show the experimental data in the 20 ns time window, which can be compared with two different simulations. In Figure 4.13b, we show a simulation that gives a reasonable match to the data. In this simulation, we have assumed that the two molecules participating in the SF event lie parallel to each other but are still randomly oriented with respect to the magnetic field. The

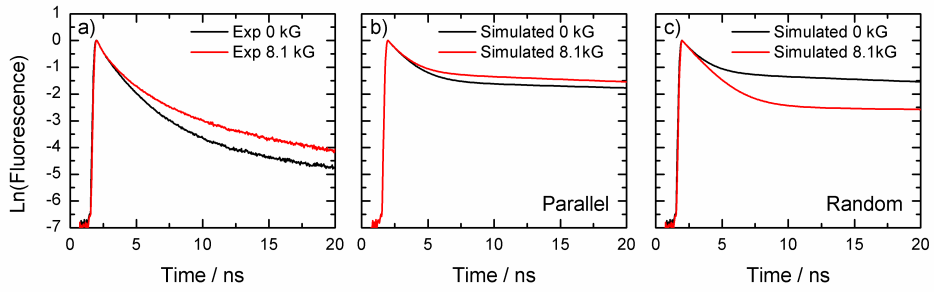

Figure 4.13: a) Experimental fluorescence decays of amorphous rubrene in the 20 ns time window. b) Simulated fluorescence decays, using the parameters in Table 4.4, showing the enhancement in the prompt fluorescence when the molecules are assumed to be parallel. This simulation agrees qualitatively with the data. c) Simulated fluorescence decay showing suppressed prompt fluorescence when randomly oriented molecules are assumed.

kinetic parameters are given in Table 4.4. In Figure 4.13c, we show the simulated data using the same rate parameters but now assuming perfectly random orientations of the chromophores with respect to each other and the magnetic field. As expected, the two different scenarios show opposite magnetic field effects, with the parallel case agreeing with the data. The agreement is not quantitative, however, because the simulated data overestimates the prompt fluorescence decay rate and does not do a good job of reproducing the nonexponential curvature in the 1-20 ns time regime.

Previously, in our analysis of tetracene data on this time scale, we found that tuning k_{trip} could introduce nonexponential character into the zero-field decay simulations and bring them closer to experiment.[25] Adjusting k_{trip} probably reflects the time scale of this diffusion-controlled loss of fusion, rather than the true lifetime of the triplet excitons. This strategy can also be employed for rubrene but at the expense of changing the behavior of the magnetic field dependence at long times. Rather than present a detailed analysis of how varying k_{trip} affects the decay shapes and magnetic

Table 4.4: Parameters Used for Simulated Data in Figures 10 and 11

Kinetic Parameters / ns^{-1}

k_{rad}	k_2	k_{-2}	k_{trip}	k_{relax}
0.06	0.5	0.5	0	0

Energetic Parameters / cm^{-1}

D*	E*	X_{int}
0.0062	0.0248	0.0001

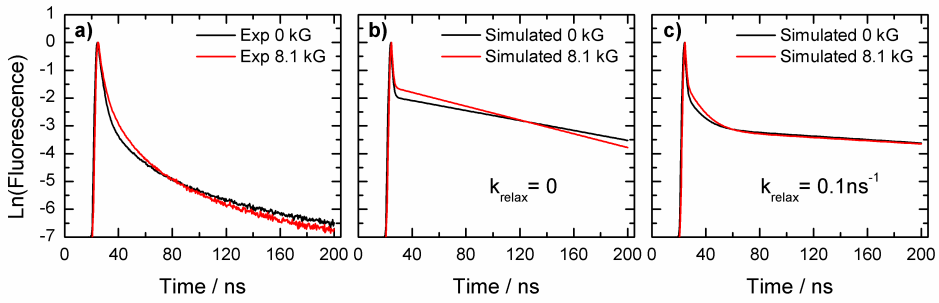

Figure 4.14: a) Experimental fluorescence decay of amorphous rubrene in the 200 ns time window. b) Simulated fluorescence decays using the parameters in Table 4.4 (assuming parallel molecules) showing both the enhanced prompt fluorescence and the later crossing of the zero and high-field decays. This simulation agrees qualitatively with the data. (c) Simulated fluorescence decays using the parameters in Table 4.4 except with $k_{relax} = 0.1$ ns^{-1}. Allowing population relaxation between triplet pair states adds curvature to the decay at early times but erases the curve crossing at later times.

field dependence, we simply state that we were unable to significantly improve the overall agreement between our simulations and the data by tweaking this rate.

An alternative approach to improve the agreement between our simulated signal and the data involves varying k_{relax}, the rate of relaxation between the triplet pair states within a given pair state manifold. In Figure 4.14a, the experimental data in the 200 ns time window can be compared with simulations, where $k_{relax} = 0$ (Figure 4.14b) and where $k_{relax} = 0.1$ ns^{-1} (Figure 4.14c). Clearly, a nonzero k_{relax} can add

some curvature to the early time decay while maintaining the magnetic field enhancement of the prompt fluorescence. The problem is that at longer times this simulation fails to predict the curve crossing due to the increased total population in the high magnetic field case. Instead, the two curves (high and zero-field) simply merge together. In fact, it is a general result that a nonzero k_{relax} eventually erases any effect of the magnetic field on the fluorescence dynamics. This can be understood in terms of the simple M-state model described above. Recall that the magnetic field effect is due to changing the number of triplet pair states with singlet character. If we again assume $|C_S^l|^2 = 1/M$ for $M \leq 9$ and furthermore that k_{relax} is rapid relative to the other relaxation rates, then the triplet population is equally distributed across all levels, $N_{(TT)_l} = 1/9 N_{(TT)}^{tot}$, and it is straightforward to show that the M dependence cancels out in eqs 3.21a and 3.21b, which become

$$\begin{aligned} \frac{dN_{S_1}}{dt} &= -k_{-2}N_{S_1} + k_2 \sum_{l=1}^{M} \frac{1}{M} N_{(TT)_l} \\ &= -k_{-2}N_{S_1} + k_2 \frac{1}{M}\frac{M}{9} N_{(TT)}^{tot} \\ &= -k_{-2}N_{S_1} + \frac{k_2}{9} N_{(TT)}^{tot} \end{aligned} \tag{4.10a}$$

$$\begin{aligned} \frac{dN_{(TT)}^{tot}}{dt} &= k_{-2}N_{S_1} - \left(k_{trip} + \frac{k_2}{M}\frac{M}{9}\right) N_{(TT)}^{tot} \\ &= k_{-2}N_{S_1} - \left(k_{trip} + \frac{k_2}{9}\right) N_{(TT)}^{tot} \end{aligned} \tag{4.10b}$$

In the limit of rapid spin relaxation, the dependence on M disappears and there is no magnetic field effect. If there is a separation of time scales, then the general argument

still holds and the difference between high and zero-field data will disappear on a time scale comparable to the inverse of k_{relax}. Experimentally, we see a measurable difference between the two decays out to 200 ns, where our signal-to-noise becomes limited by the low signal levels. The fact that we see a clearly resolved crossing of the high and zero-field curves at $\sim$ 100 ns indicates that population relaxation between the spin sublevels is not complete on this time scale. Thus we cannot use a rapid k_{relax} to improve our agreement with the data in the 20 ns window because it leads to the disappearance of the magnetic field effect in the 200 ns time window.

Discussion

The qualitative agreement between our simulations and the experimental data provides support for the idea that SF is occurring in amorphous rubrene films. Although SF has been reported previously in amorphous rubrene, that work mainly focused on the magnetic field effects on triplet spin relaxation and did not even report a fission rate.[80] It is interesting that a purely amorphous system that shows no sign of excitonic coupling can still exhibit reasonably efficient SF, although as noted in the Introduction, previous work has provided considerable evidence for SF in other disordered systems.[33,71] Our results suggest that SF events occur mainly within certain ordered locations within the film rather than between totally randomized chromophores. This conclusion is consistent with the recent work on disordered diphenyltetracene films, where the transient absorption kinetics were interpreted in

terms of exciton migration to preferred sites where rapid SF can occur.[33] The initial rapid decay (0.2 ns) of the fluorescence may be due to SF by excitons created at or near such preferred sites, whereas the later decay (2.1 ns) may represent a convolution of exciton diffusion, followed by SF. Rapid singlet exciton migration is certainly occurring in our rubrene films. We attempted to measure its rate using polarization anisotropy decay but found that the anisotropy decreased to zero within our instrument response, indicating an exciton transfer time of 15 ps or less, but if the singlet excitons rapidly diffuse through the film until they arrive at a location where two rubrenes are optimally aligned to undergo SF, then this would explain why the magnetic field effect is consistent with an oriented SF chromophore pair, despite the disordered character of the film. In reality, the kinetics of the SF/TF processes are more complicated than the simple model presented in eqs 3.19a and 3.19b. A more sophisticated model would take into account exciton diffusion (both triplet and singlet) as well as the possibility that SF can occur with a distribution of rates due to a distribution of pair distances and orientations. Rather than attempt a detailed modeling of singlet diffusion and variable SF rates in amorphous rubrene, we have approximated these complex processes by simple rate constants. If we assume that the only other singlet decay process is radiative decay, occurring with the monomeric rate $k_{rad} = 0.06$ ns^{-1} , then given $k_{fiss} = k_{-2} = 0.5$ ns^{-1} , we can estimate that more than 90% of the initially excited singlets undergo SF.

One reason we don't see any evidence for the randomly oriented magnetic field

effect we calculated is that the theory used to calculate the C_S^l values could possibly be incorrect. After performing this work, it came to our attention by researchers Patrick Tapping and David Huang at the University of Adelaide that we made an error in our calculations and the magnetic field effect for randomly oriented molecules should be similar to that of parallel molecules in that the number of triplet pair states with singlet character decreases as you approach the high field limit. Our error was presented to us as follows. The basis we calculated our C_S^l values in was not the product basis of $|xx\rangle$,$|xy\rangle$,$|xz\rangle$...$|zz\rangle$ as presented in the previous text, but actually $|xx'\rangle$,$|xy'\rangle$,$|xz'\rangle$...$|zz'\rangle$ such that $x_A \neq x_B$ as we were working with two inequivalent axis frames. The issue with this approach is that the singlet state of $|S\rangle = \frac{1}{\sqrt{3}}(\langle xx| + \langle yy| + \langle zz|)$ only holds for equivalent molecules and therefore the calculated projections of our triplet pair states onto this singlet state would yield incorrect C_S^l values. One solution for this would be to create the Hamiltonian matrices for one of the molecules in the x',y',z' basis and conduct a change of basis into x,y,z basis in order to correctly project onto the singlet state. This could be done by applying rotation operators to the Hamiltonian such that $H_{rot} = RHR'$ where R can be a directional cosine matrix or a set of Euler rotations which map one basis on to the other, i.e. $x = ax' + by' + cz'$ where a, b, and c are coefficients. While we agree that this rotation needs to be done, in a paper by Lendi et al. which included rotations such as these, it was shown that certain orientations between molecules will yield the results presented within this Chapter.[86] There are also researchers who have since

used our method of calculation to match their experimental results.[87] Therefore, it is unclear to us at this time whether correcting the calculation will have any effect on the physical picture presented here.

The high SF efficiency in the amorphous films most likely arises from the ability of the single excitons to explore their environment and find ordered pairs suitable for rapid SF. The behavior of the amorphous films can be contrasted with that of other acene systems. In covalent tetracene dimers, computational results suggested that a low barrier to rotation around the linker also leads to conformational disorder in solution, yet in those molecules only 2 to 3% of the singlets underwent SF.[88,89] The disorder in a truly amorphous molecular film may provide a much greater variety of molecular pair geometries, some of which may be optimal for undergoing SF. The possible arrangements of the tetracenes in our covalently linked dimers were much more limited due to the constraints of the covalent linker that enforced large spatial separations. When compared with crystalline and polycrystalline tetracene, where fission occurs with time scales of 200 and 80 ps,[24,69] the overall rate in our amorphous films is slower. An even more appropriate comparison is with recently reported results in rubrene single crystals, where SF apparently occurs on two different time scales, 5 and 50 ps.[79] In both types of crystalline samples, more rapid SF would be expected if the crystal packing arranges the molecules in an orientation favorable for SF because the excitons no longer have to undergo diffusion to an ordered site.

Our analysis of magnetic field effects has provided some insights into their origin

and implications. Changes in both the early and late time fluorescence signals can be most easily understood in terms of changes in partitioning between the singlet and triplet manifolds due to a change in the number of triplet pair states with singlet character. For parallel chromophores, application of a magnetic field decreases the number of triplet states that can couple to the singlet. As this number decreases, less population is able to hide in the triplet manifold, which increases the fluorescence signal in the short term but decreases it in the long term as long as $k_{trip} < k_{rad}$. At very early times, before any back transfer from the triplet pair can occur, the magnetic field should not affect the fluorescence decay at all, as we observe experimentally. If back transfer cannot occur at all, for example, because the triplet pair energy is much lower than the singlet energy, then we also predict no magnetic field effect. Lastly, rapid population relaxation between triplet pair states (large values of k_{relax}) is also expected to wash out magnetic field effects on the singlet decay, but it is important to emphasize that whereas the quantum kinetic model we have developed gives a good qualitative description of the data it fails to provide quantitative agreement. As discussed above, adding spin-lattice relaxation is not sufficient. The clearest deficiency of our model is its neglect of the spatial diffusion of the excitons. In reality, the recombination rate parametrized by k_2 is most likely time dependent due to the gradual spatial separation of the geminate triplets as they diffuse in the film. Such a time-dependent k_2 rate would effectively smooth out the sharp biexponential features of the calculated curves in Figures 4.13 and 4.14. Currently, we are working to add

diffusion to the kinetic model to improve agreement with experiment.

The last area of interest is the evolution of the newly created triplet excitons. In this article, we only studied relatively low excitation densities due to the limited power of our laser pulse. Given the large spatial separation ($\sim$ 50 nm) of the triplet pairs produced under these conditions, it is not surprising that triplets from different pairs never encounter each other. Even if the triplets are separating spatially, the lack of intensity dependence in the fluorescence signal means that nongeminate triplets play no role in the dynamics even on a 200 ns time scale. Of course, at higher laser intensities, we would expect that triplets produced by nearby SF events to interact and lead to bimolecular dynamics, including a power-law decay. Another factor that may limit the role of nongeminate triplets is the disordered nature of the film. Disorder limits the triplet diffusion and may allow the pairs to remain associated for such long times. In a crystal, with more rapid diffusion, triplets created by separate SF events would be more capable of fusing with each other, and nongeminate triplets might become important on shorter time scales. Another important point is that the measurable magnetic field effect at long times means spin population relaxation in this system is slow, longer than 200 ns at room temperature. This lack of population relaxation is consistent with the observation of long spin diffusion lengths in this material.[90] However, it has been found that the spin-lattice relaxation rate (k_{relax}) for triplets in molecular crystals decreases as the magnetic field increases, and this can affect the delayed fluorescence dynamics.[91,92] Thus the negligible k_{relax} deduced from

the high magnetic field data may not apply to the zero-field dynamics of the triplet. Finally, we cannot say how long the geminate pairs studied in this work maintain spin coherence. Our previous work on tetracene showed that SF produces coherent triplet pairs that can lead to quantum beats in the delayed fluorescence. The SF rate in amorphous rubrene does not appear to be sufficiently rapid to generate beating, and we could not discern any periodic modulation in the delayed fluorescence signal. Whether the triplet sublevel coherences can be maintained on the same time scale as the association of the geminate pair (i.e., > 100 ns) remains an open question.

4.3.3 Conclusions

In this work, it has been shown that SF can occur in highly disordered films of rubrene. Compared with crystalline tetracene films, the dominant SF rate is about 10 times slower, but we still estimate that 90% of the singlet excitons undergo SF at room temperature. The hybrid quantum-kinetic model pioneered by Merrifield has been extended to model how the dynamics of the geminate triplet pairs are manifested in the fluorescence decay dynamics and their magnetic field dependence. Our simulations show that the magnetic field effect is very sensitive to mutual chromophore alignment, and our data are consistent with a local ordering for rubrenes that participate in the SF event. Overall, our data indicate that SF is indeed possible in a relatively simple amorphous system and demonstrate the utility of making dynamic measurements in the presence of a magnetic field. Varying the film preparation conditions could allow

us to probe the dependence of SF on the molecular-level morphology, whereas the effect of the exciton diffusion rates on the SF dynamics should manifest itself in the temperature dependence of the fluorescence decay. These experiments are currently underway

4.4 Diphenylhexatriene

It has been proposed that the singlet fission rate rate depends critically on the interaction geometry between participating chromophores, and this dependence has been the subject of several theoretical investigations.[93–97] A second criterion concerns the accessibility of the triplet products. Ideally, the triplet states would have long lifetimes, allowing them to diffuse over long distances, as well as sufficient energy to undergo ionization[98] or energy-transfer reactions. As discussed in the bulk of this thesis, SF has been most thoroughly studied in the polyacenes,[22,33,99,100] which tend to have relatively low energy triplet states. The observation of efficient SF in carotenoid aggregates[36] suggests that polyene-based molecules may provide an alternative to the polyacenes.

Crystalline 1,6-diphenyl-1,3,5-hexatriene (DPH), a compound that allows us to address both issues raised in the preceding paragraph, would be a great tool to answer these fundamental questions about SF. DPH crystallizes into two different polymorphs, a monoclinic form (Figure 4.15a,b) and an orthorhombic form (Figure 4.15c,d).[101] This polymorphism can be controlled using different crystallization con-

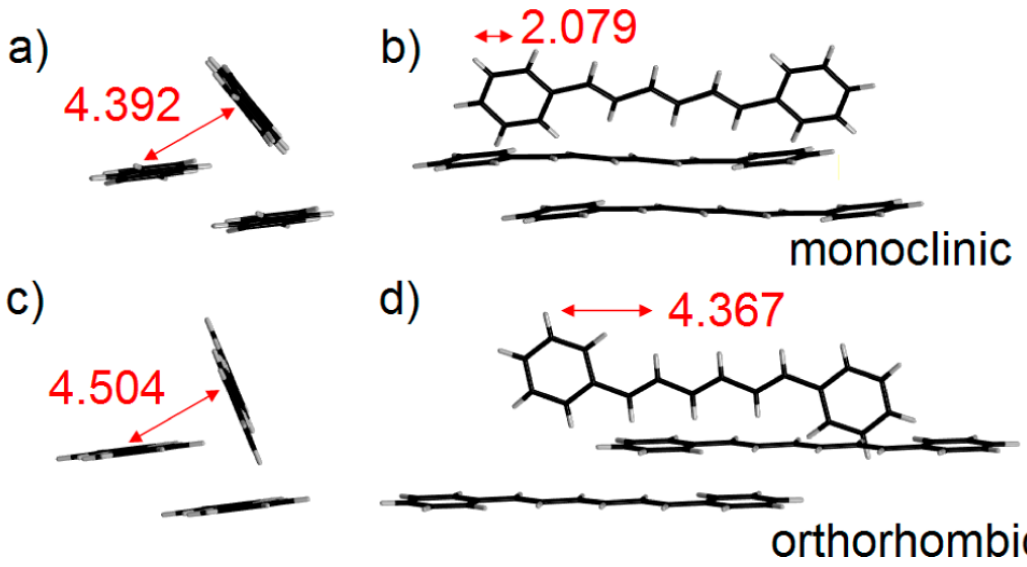

Figure 4.15: Crystal packing patterns of monoclinic DPH [(a) top-down view and (b) side view] and orthorhombic DPH [(c) top-down view and (d) side view] from ref.[101] The edge-to-face distance and vertical slip distance are measured from the long axis of each molecule; all values are in angstroms.

ditions and provides an opportunity to study how the SF rate depends on molecular arrangement without having to modify the molecular structure. Furthermore, we characterize the triplet dynamics subsequent to the SF reaction to determine which polymorph demonstrates favorable triplet diffusion properties. In order for SF to take place, it is usually assumed that the excited singlet S* and triplet T_1 energies must fulfill E(S*) 2E(T_1). In DPH, E(T_1) has been measured to be $\sim$ 12400 cm^{-1}, Robert Dillon, during his time in the Bardeen group, measured E(S_1*) to be 26700 cm^{-1}, and therefore $\Delta 2T - S = 2E(T_1) - E(S^*) = -1770$ cm^{-1}. Therefore, SF should be exoergic for isolated DPH molecules. When the DPH molecules crystallize, both singlet and triplet states shift in energy. It was found that the values of $\Delta 2T - S$ are 340 cm^{-1} for the monoclinic form and 320 cm^{-1} for the orthorhombic form, which

are the same to within the experimental error of ± 50 cm^{-1}. Due to the large singlet energy shifts, SF becomes slightly endoergic in both crystal forms of DPH, but this does not necessarily preclude rapid SF. As will be shown in the following chapter, an even larger energetic mismatch exists in crystalline tetracene, where the SF reaction proceeds rapidly at room temperature. Dynamic evidence for the role of SF is obtained by measuring the singlet-state decay using time-dependent fluorescence. Logarithmic plots of the fluorescence decays of the monomer in toluene, along with the monoclinic, and orthorhombic crystal forms, are shown in Figure 4.16a for a 1 ns time window. In toluene, the decay is single exponential with a time constant of 6.53 ns. In the crystals, the fluorescence decay is strongly non-exponential with an initial decay time on the order of 300 ps in the monoclinic form but slower in the orthorhombic form. The initial fast decay is followed by a longer-lived multiexponential fluorescence decay. We attribute the long-lived decay component to delayed fluorescence from the singlet state re-formed by triplet fusion (TF), based on the fact that the spectrum of the initial component (0-100 ps) is identical to that of later components. In both monoclinic and orthorhombic crystals, the delayed fluorescence decayed with a single-exponential decay time of 50 ± 5 µs^{-1}, which places a lower limit on the triplet lifetime. The long-lived monoclinic fluorescence decay is shown in Figure 4.16b. The fluorescence decays were insensitive to preparation conditions: single crystals and ultrathin polycrystalline films grown by solution or vapor deposition show the same initial and delayed fluorescence kinetics.

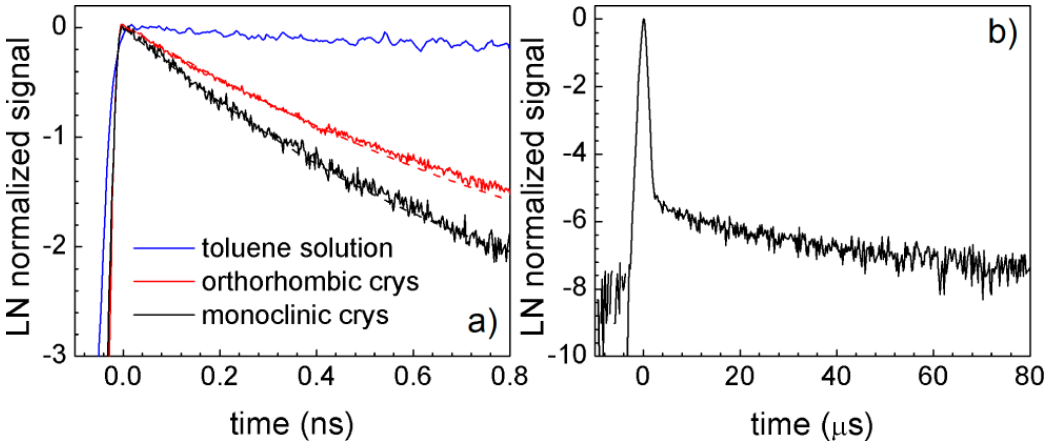

Figure 4.16: (a) Fluorescence decays in a 1 ns window for DPH in toluene (blue), monoclinic crystal (black), and orthorhombic crystal (red). The dashed lines are the calculated decays using the Merrifield kinetic model with the parameters in Table 4.5. (b) Decay of the delayed fluorescence of monoclinic DPH in a 100 s window.

While the presence of a rapid singlet decay channel is consistent with the presence of SF, it is not conclusive proof. As with the other systems discussed within this chapter, one can look for magnetic field effects on the fluorescence dynamics.[18,56] In both monoclinic and orthorhombic crystals, the molecules are close to parallel, and application of a magnetic field decreases the number of triplet pair states with singlet character from 3 to 2, out of 9 possible pair states. Figure 4.17 shows a clear enhancement of the fluorescence signal in the 20 ns time window for both (a) monoclinic and (b) orthorhombic crystals in the presence of a 8100 G magnetic field. The fast singlet decay is dominated by SF in the case of the solid state samples unlike the solution sample.

Table 4.5: Kinetic Rates Used To Simulate the Crystal Fluorescence Decays in ns^{-1}.

crystal	k_{rad}	k_1	k_{-1}	k_2	k_{-2}	$k_{relax}(highfield)$
mono	0.21	0.05	0.7	1.8	3.4	0.5(0.05)
ortho	0.21	0.01	0.2	1.3	2.3	0.5(0.05)

4.4.1 Kinetic modeling of the magnetic field effects

We start with the kinetic model described in chapter 3. The coefficients for singlet character, C_S^l, are calculated quantum mechanically as described previously for a set of parallel molecules. Simulation of the fluorescence decays yielded the rate constants summarized in Table 4.5. The fluorescence decays calculated using these parameters are overlaid with the data in Figures 4.16 and 4.17. The agreement is quantitative in the 1 ns window, and the calculations do a reasonable job of reproducing the 20 ns data. The kinetic model contains five parameters listed in Table 4.5, and it is worth considering how sensitive e calculated curves are to the details of the model. The initial decay (< 0.5 ns) is determined solely by the k_{-2} fission rate, and thus the different k_{-2} rates in Table 4.5 are model independent. If we take the lifetime of DPH in the absence of SF to be that of the isolated molecule in polystyrene (0.21 ns^{-1}), we estimate from the k_{-2} values that up to 90% of the initially excited DPH molecules undergo SF. The k_2 fusion rate is fixed by the point where the initial fast decay gives way to a slower delayed fluorescence and should also be robust with respect to model choice. There is more flexibility to adjust the k_1, k_1, and k_{relax} rates to match the longer time delayed fluorescence dynamics in the 20 ns window, so the

absolute magnitudes of these rates should be viewed with more caution.

A notable difference between the monoclinic and orthorhombic fluorescence decays is the lower overall level of delayed fluorescence for the monoclinic form. The amplitude of the delayed fluorescence is determined by k_1, k_{-1}, and k_{relax}. k_{relax} reflects spinlattice relaxation, a localized process that is expected to be insensitive to crystal packing. The decrease in k_{relax} in the presence of a magnetic field has previously been observed in SF/TF materials,[91,102] and can arise through several different physical mechanisms.[80] The k_1 and k_{-1} rates reflect the rate of separation and association of the triplet pairs and should be proportional to the triplet exciton diffusion constant. Both rates are higher in the monoclinic crystal, which likely reflects more rapid exciton hopping. In the orthorhombic form, the larger separation of neighboring DPH molecules is expected to reduce the triplet hopping rate,[103] resulting in smaller observed k_1/k_{-1} values.

In summary, the rapid fluorescence decay and strong magnetic field effect in crystalline DPH indicate that up to 90% of the initially excited singlets undergo SF. Compared to the prototypical SF material tetracene, DPH crystals have the advantages of longer triplet lifetimes ($\geq$ 50µs) and significantly higher triplet energies ($\sim$12000 cm^{-1}). By taking advantage of crystal polymorphism, we have provided unambiguous evidence that molecular packing affects the rates of SF and triplet pair separation, both important parameters for determining the ultimate utility of a SF material.

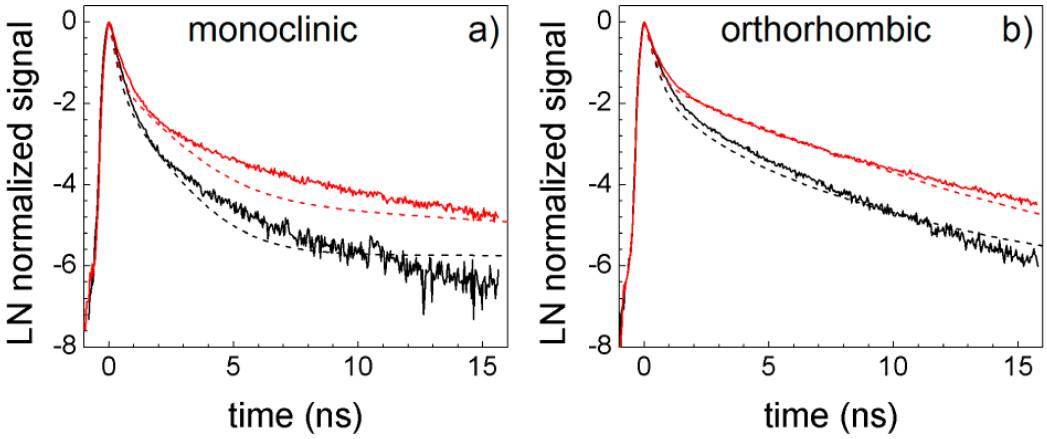

Figure 4.17: Magnetic field dependence of the fluorescence for the monoclinic crystal (a) and the orthorhombic crystal (b). The black curves are the data with no applied field, and the red curves are in the presences of an 8.1 kG field. Dashed lines are the calculated decays using the Merrifield kinetic model using the parameters in Table 2

Chapter 5

How Crystal Morphology Influences Singlet Fission Dynamics

5.1 Introduction

The magnetic field effects studied in the previous chapters explain the dynamics of the back and forth transfer between singlet state and triplet pair, but they do not explain the forward rate of singlet to two triplets. Despite extensive study, there remain discrepancies in the literature as to the kinetics of singlet fission (SF) in crystalline tetracene. The first unresolved issue concerns the initial decay rate of the S1 state. Time-resolved fluorescence measurements on tetracene single crystals

consistently yielded singlet lifetimes on the order of 200-300 ps.[45,104–108] Fluorescence lifetime and transient absorption measurements on polycrystalline films (PCFs) revealed singlet lifetimes ranging from 30-90 ps.[22,66–68,75] Two-photon photoemission experiments on tetracene monolayers yielded an even shorter SF time on the order of 8 ps.[23] A second question concerns the existence of an activation energy ΔE_{act} for SF. Early investigators making temperature-dependent fluorescence quantum yield measurements on single crystals deduced that SF was an activated process with $\Delta E_{act} =$ 1200-1800 cm^{-1}.[18,45,57] These values correlated well with the $\Delta E_{act} = 2E(T_1)$-$E(S_1)$ obtained from measurements of the S_0-T_1 and S_0-S_1 optical transition energies.[20] However, recent measurements on PCFs show that the initial singlet decay has little or no dependence on temperature over the range 300-5 K.[22–24,46,68] This apparent lack of activation barrier has been attributed to entropic contributions due to exciton diffusion in the solid,[23,109] as well as to the presence of dull or dark intermediate states.[22,24,46]

The discrepancies between the single crystal and PCF results are hard to understand if the SF rate depends only on the local ($\sim$ 1 nm) crystal environment, since both samples are crystalline on this lengthscale. One possible explanation is experimental error, but the variations are large enough and widespread enough to make this unlikely. A second explanation is that the picosecond dynamics are sensitive to differences in crystal morphology, like crystallite size, defect concentration, or modified molecular packing near interfaces. It is this second mechanism that is the subject

of this chapter. We investigate the differences in dynamics between PCFs and single crystals grown from solution. We find that single crystals and PCFs have different singlet decay rates and different temperature dependences. Other notable divergences in behavior include the absence of spin state quantum beats and the appearance of a red-shifted excimer-like emission in many PCF samples. We confirm that morphology is the dominant factor by showing that when a PCF is thermally annealed to produce larger crystal domains, single crystal behavior is recovered. The results herein should help resolve discrepancies as to the intrinsic timescale for SF in crystalline tetracene, which we think is in the range 250-300 ps. We hypothesize that the faster rates observed in PCFs are likely mediated by singlet exciton diffusion to defects or interfaces. These results suggest that crystal morphology as well as molecular packing should be taken into account when analyzing SF rates in molecular solids.

5.2 Results and Discussion

5.2.1 Polarized Light Microscopy

Figure 5.1 shows polarized light microscopy images of three types of tetracene samples. In Figure 5.1a, a single solution-grown tetracene crystal, on the order of 100 µm wide and 20 nm thick, shows uniform birefringence, indicative of a single crystal domain. The evaporated PCF in Figure 5.1b shows only a few birefringent specks, suggesting that most of the crystal domains are smaller than the microscope

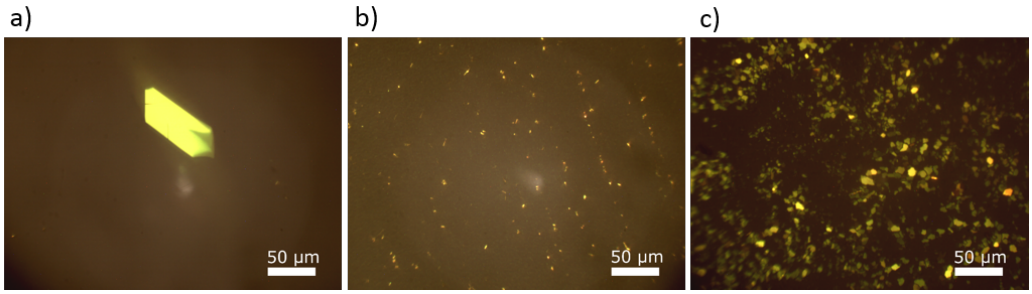

Figure 5.1: Polarized light microscopy images of a) a solution-grown single crystal of tetracene, b) an evaporated polycrystalline film (PCF) of tetracene, and c) an evaporated film of tetracene which has been annealed at 400k for 30 minutes. These images illustrate the differences in the sizes of the crystalline domains for the different samples.

resolution and randomly oriented. This is consistent with previous x-ray diffraction and electron microscopy studies of tetracene thin films grown by sublimation.[110,111] After the PCF film is heated to 400 K in vacuum, one observes the formation of larger crystalline domains, as shown in Figure 5.1c. This thermal annealing process provides a way to increase the crystallinity of the sample without introducing other chemical species. This approach allows us to prepare three different samples, grown from the same batch of tetracene, with distinct morphologies. We did not examine vacuum sublimed single crystals due to the difficulty of isolating optically thin specimens.

5.2.2 Time-Resolved Fluorescence

The initial fluorescence decay in solid tetracene samples is roughly 20x faster than for tetracene by itself in solution.[69] The extensive experimental work cited in the Introduction has established that this accelerated decay is due to SF, although the enhanced radiative decay channel makes a small contribution (0.08 ns^{-1}).[67] In Figure

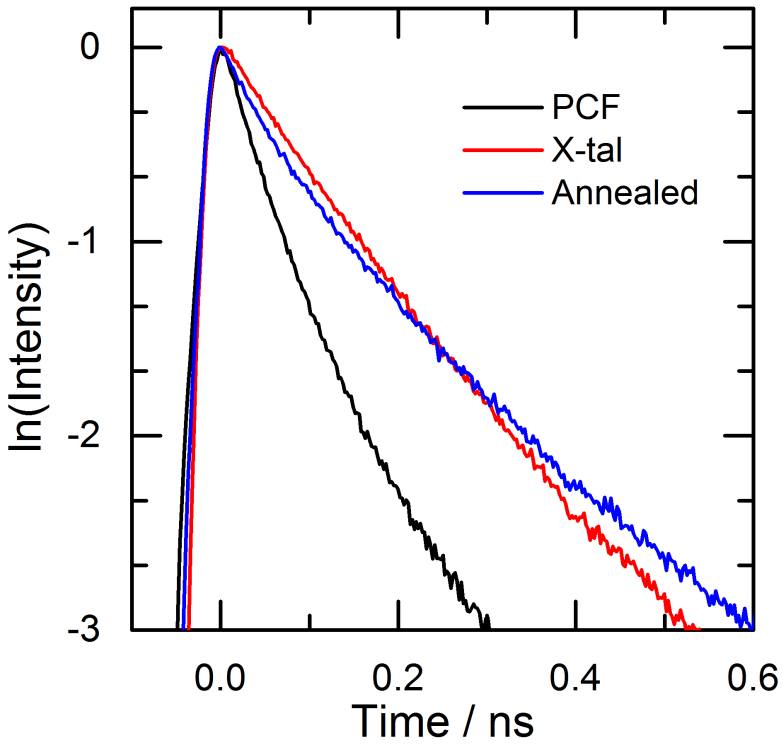

Figure 5.2: Comparison of the fluorescence decays (log scale) for a solution grown tetracene single crystal (red), a tetracene PCF before (black) and after annealing (blue). The 1/e time for the tetracene single crystal is 170 ps,while that of the PCF is 70 ps before annealing and 140 ps after annealing.

5.2, we show that the three different solid-state morphologies give rise to different initial fluorescence decay rates on the subnanosecond timescale, as measured by the slope of the natural log of the signal over the first two natural logs (86%) of the decay. We take this region to reflect the intrinsic decay of the initially excited singlet state, before triplet fusion gives rise to a slower delayed fluorescence component. The solution grown single crystal yields a decay time of 170 ps. This value is at the low end of the range reported by earlier workers.[45,104–108] Other single crystals yielded

slower decay times of up to 300 ps, and the data in Figure 5.3 show that the initial decay rates could vary by a factor of 2. The evaporated films, on the other hand, always have more rapid decays. The example shown in Figure 5.2 has an initial decay time of 70 ps. This decay time is close to the average reported by most workers who have studied tetracene PCFs deposited by evaporation.[66–68] In general, we saw more uniform decay times for the PCF samples, with initial lifetimes varying between 70 and 90 ps. When the PCF is thermally annealed, the initial fluorescence decay slows dramatically to 140 ps, close to that of the single crystal. The conclusion is that the singlet decay is at least 2x faster in a PCF than in a single crystal, on average.

We note that recent transient absorption experiments on tetracene single crystals have reported more rapid singlet decay times of 50-80 ps, leading to the opposite conclusion that SF is more rapid in single crystals.[112,113] In those experiments, high pump pulse fluences mean that exciton-exciton annihilation always plays a role in the observed dynamics, complicating analysis of the singlet decay. Higher defect densities resulting from different crystal growth methods could also contribute to a faster apparent SF rate (see below).

In Figure 5.3, we compare the temperature dependent initial decays for the PCF and single crystal over the range 200-400 K. In a PCF, we and others have found that the initial singlet decay has almost no temperature dependence in the range 300-4 K.[22–24,46] But this conclusion must be qualified by the knowledge that tetracene can

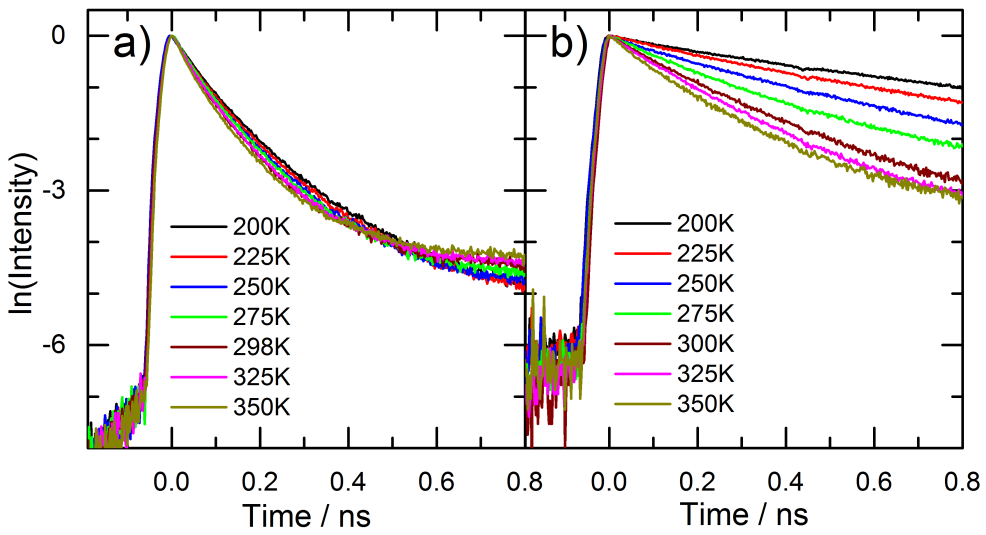

Figure 5.3: Temperature dependent fluorescence decays (log scale) for a) a tetracene evaportaed PCF and b) a tetracene single crystal. The singlet lifetime of the single crystal exhibits a much greater response to temperature than that of the thin film.

undergo at least on phase transition around the temperature of 150 K.[114–116] In the present work, we measure the SF rate over the range 200-400 K, where there are no known phase transitions. In Figure 5.3a, the fluorescence decays for the PCF sample over this temperature range exhibit almost no change, while the single crystal decays in Figure 5.3b show a dramatic increase in the initial singlet decay rate. As described above, there was a significant variation in the initial decay rate in the single crystals, but all showed a larger temperature dependence than the PCF. In Figure 5.4 we show Arrhenius plots for a PCF sample and for seven different single crystals. The PCF has a small slope, from which we extract an activation energy $\Delta E_{act} = 55$+/-30 cm^{-1}. For the single crystal samples, there is a larger variation in rate constants, but we can extract an average value for $\Delta E_{act} = 440$+/-100 cm^{-1}. If the PCF is thermally

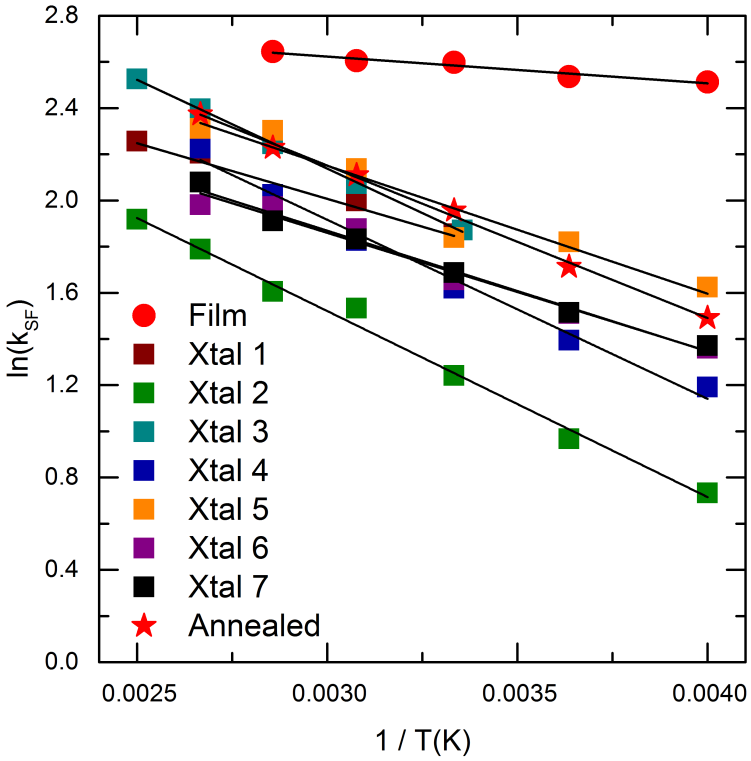

Figure 5.4: Arrhenius plot showing the relationship between the initial decay rate vs temperature for a tetracene PCF (purple squares) and 7 different tetracene single crystals in order to demonstrate the spread in initial singlet decay times. The data for the annealed PCF is also shown (red stars).

annealed and its temperature-dependent singlet decay rate measured, the ΔE_{act} = 460 +/-100 cm^{-1} is similar to that of the single crystals.

There are two other reproducible differences between the PCFs and the more crystalline samples. First, as shown in our previous work,[25] the PCF exhibits little or no oscillations in the delayed fluorescence signal due to quantum beating of the triplet pair spin states, as shown in Figure 5.5.The oscillation visibilities are consistently higher in the single crystal and thermally annealed samples, as shown in Figure 5.5b and 5.5c. A second difference between the PCF and single crystal is that many PCF samples exhibit a red-shifted, broadened emission centered close to 600 nm. The amplitude of this feature in the spectrum shown in Figure 5.6 varies between PCF samples, and in our previous work we concentrated on samples where this feature was minimized or absent altogether. Its decay time of 2.5 ns is much slower than that of the exciton fluorescence peaked at 535 nm, but it can dominate the delayed fluorescence spectrum in samples where it is present. This feature is largely absent in single crystals and can be removed by thermally annealing the PCFs (Figure 5.6). The fact that it can be minimized by improving sample crystallinity suggests that this emission is associated with a defect in crystal packing. Its lower energy and lack of vibronic features suggests that it could be an excimer species associated with sites where the tetracenes experience face-to-face packing, rather than the edge-to-face packing in a perfect crystal lattice. This type of defect-induced excimer emission has been well-studied in crystalline anthracene[117–119] and has been characterized to a limited degree in tetracene single crystals.[120]

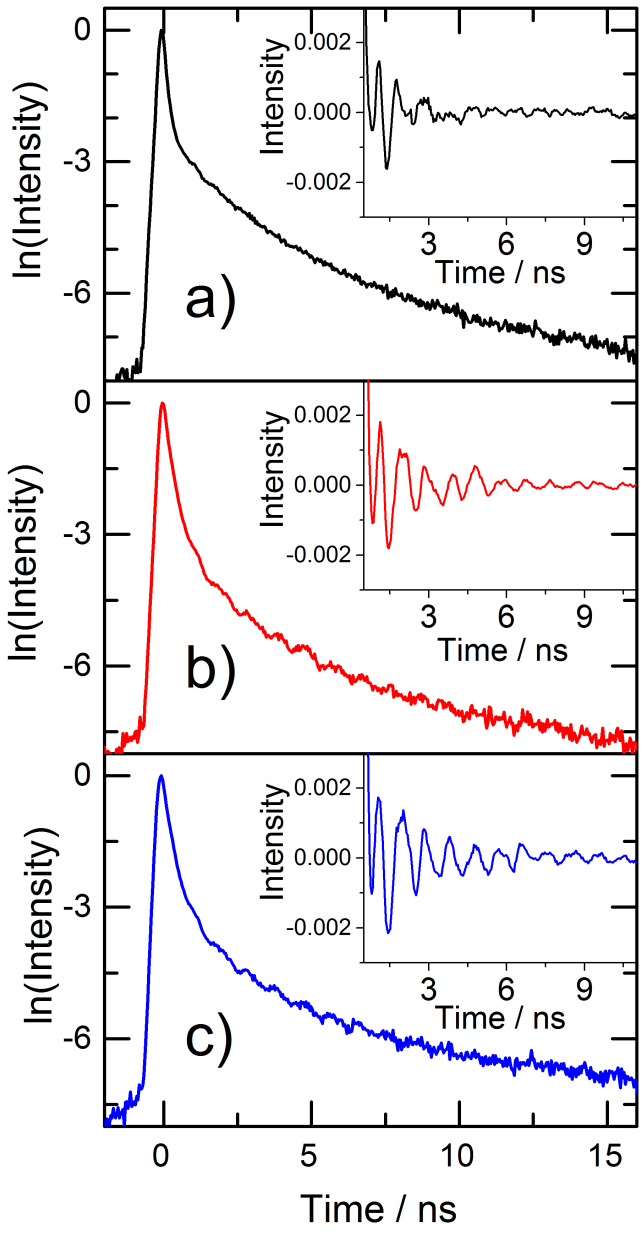

Figure 5.5: Normalized time-resolved fluorescence decays for a) a tetracene PCF, b) a tetracene single crystal, and c) an annealed tetracene PCF. All three decays have similar levels of delayed fluorescence that display quantum beats (insets), but the annealed film and the single crystal exhibit more intense beating over a longer time.

We now examine the origin of the faster singlet decay in the PCFs. We consider three types of nonradiative relaxation processes: internal conversion to the ground state, relaxation to a lower energy dark state, and accelerated singlet fission. We rule out internal conversion because transient absorption experiments on PCFs show no evidence for recovery of the ground state bleach on the 1 ns timescale.[22,69,75] Formation of a lower energy dark state would be expected to have a recognizable signature in the PCF transient absorption signal, but experiments on thin films and single crystals yield similar results, all of which are consistent with SF being the dominant nonradiative decay pathway.[22,24,75,112,113] Additional evidence that SF is the main decay channel in the PCFs is that the ratio of prompt to delayed fluorescence signals is similar for both PCFs and single crystal samples, as can be seen from the decay curves in Figure 5.5. If the accelerated singlet decay in the thin film did not produce triplets, we would expect the magnitude of the delayed fluorescence to decrease since there would be fewer triplets to recombine.

Our observations are consistent with the idea that structural differences between the PCF and single crystal play a central role in determining the SF rate. The fluorescence spectra in Figure 5.6 provide evidence that the PCF has defect sites associated with tetracene molecules that have adopted a more cofacial arrangement. But there is also evidence that when tetracene is evaporated onto a surface, subtle differences in the molecular packing can arise.[121,122] These differences, which presumably would be most pronounced for molecules closer to the substrate surface, could also lead to

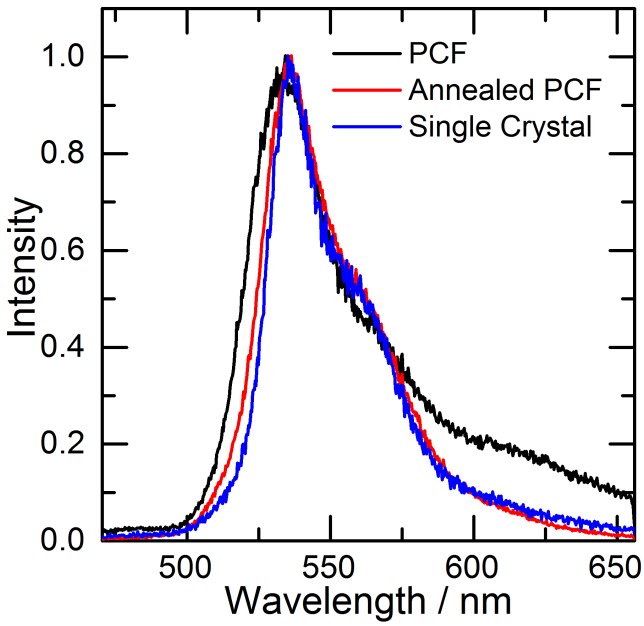

Figure 5.6: The fluorescence spectra of a tetracene PCF (black), single crystal (blue) and annealed PCF (red). The data are integrated over 0-15 ns. The unannealed PCF sample exhibits an additional feature at 625 nm that has a lifetime of approximately 2.5 ns

an accelerated SF rate. The diffusion length for the singlet exciton in crystalline tetracene has been estimated to be 10-15 nm at room temperature,[123,124] allowing a large fraction of the excited singlet population to access regions of the sample with modified packing and/or defect sites. The physical picture of the dynamics in the PCFs starts to resemble that postulated for amorphous films of diphenyltetracene[33] and rubrene,[32] in which the singlet excitons diffuse until they reach a site where the molecules are suitably oriented to undergo rapid SF. In this scenario, the singlet decay in the PCFs reflects a weighted average of different SF rates, including the intrinsic SF rate of the single crystal. Different preparation methods could affect the density of defect sites and/or the presence of substrate-induced packing changes, resulting in the wide variance in reported SF rates for PCFs. Of course, our single crystal samples also exhibit substantial variations in both the SF rates and ΔE_{act} values. The physical origin of these variations, which seem to be uncorrelated with each other, is not understood at this time. We suspect they can be attributed to variations in defect type or density between crystals. We have observed similar variations in the fluorescence decays of distyrlbenzene microcrystals grown from by solvent evaporation.[125] It may be that more controlled crystal growth methods would yield more consistent behavior.

The evidence that SF in tetracene can be mediated by defects raises the question of what type of defect states could accelerate SF. Cofacial slip-stack packing can enhance the charge-transfer (CT) interactions that enable rapid SF.[12,40] and this type

of packing can also give rise to excimer emission, as seen in some of the PCF samples. Excimer formation has been invoked as both an intermediate state in SF[126–128] and as a competing channel.[39,129,130] It is possible that in a disordered film there exist multiple cofacial packing motifs. For efficient SF, at least some of these motifs should have CT interactions that are stronger than those of the edge-to-face packed molecules in the pristine crystal, but too weak to form stable excimer states that cannot dissociate into triplets. In this scenario, excimer emission signals the presence of the type of structural defects that can enhance SF, but the emissive excimer states themselves are not necessarily intermediates in the SF process.

Lastly, we address the question of whether SF is thermally activated in tetracene. SF mediated by singlet exciton diffusion to hotspots would be expected to depend only weakly temperature, since Forster energy transfer relies on spectral overlaps that change only slightly over this temperature range. The absence of such hotspots in a solution grown crystal allows us to measure an activation energy, $\Delta E_{act} = 450$ cm^{-1}, that probably represents a lower bound for that of a perfect tetracene crystal. We should also note that this activated process is only operative in the range 200-400 K. These results cannot explain the lower temperature data in both the PCF and the single crystal, where the singlet decays remain rapid while the signature delayed fluorescence is replaced by redshifted, longer-lived emission features.[24,46] Early workers simply integrated over the entire emission spectrum, assuming it all originated from the singlet state, and derived roughly Arrhenius behavior. We now know the situation

is more complicated and that multiple emitting states are involved, but the nature of the state formed by the rapid decay of the initial singlet state at lower temperatures remains unclear.

5.3 Conclusion

In this chapter, We explored how SF dynamics in tetracene depend on sample preparation. We find large differences between the behaviors of polycrystalline thin films grown by thermal evaporation versus thin crystals grown from solution. In the more crystalline samples, we see a slower SF rate that has a substantial activation energy over the range 200-400 K. More crystalline samples also exhibit more pronounced quantum beats due to the triplet pair spin coherences, and less redshifted excimer-like emission. We hypothesize that these differences arise from the ability of rapidly diffusing singlet excitons to sample defect sites or areas with different molecular packing in the PCFs. Our results provide a dramatic demonstration of how sample preparation can affect exciton dynamics in molecular crystal semiconductors.

Chapter 6

Studying Energy Transfer into Si from Tetracene Using Fluorescence Quenching

6.1 Introduction

In previous chapters, singlet fission (SF) was studied in different molecular systems, but in this chapter the resultant triplets coming from the SF process will be studied to determine whether they can do useful work. Ideally, the SF phenomenon could be integrated into existing silicon photovoltaic technology without having to develop an entirely organic-based photovoltaic system. One approach would be to use energy transfer from excitons in the organic layer to create excitons in an inorganic substrate, which would then dissociate into electron-hole pairs. Dexter originally suggested that it might be possible to utilize Frenkel triplet excitons in an organic material to photosensitize Wannier excitons in an inorganic semiconductor.[47] Agranovich has recently summarized theoretical and experimental work on energy transfer

in hybrid excitonic systems.[131] In related work, it has been shown that triplets produced by SF in pentacene can be ionized by PbSe nanocrystals, and the resulting charge carriers injected into an amorphous Si layer.[132] However, it is an open question whether the triplet excitons produced by SF could be directly harvested in the manner suggested by Dexter.

Tetracene is a prototypical SF material[27] whose S0→T1 energy gap is close enough to Sis bandgap that triplet energy transfer should be possible. In 1983, Boyd and coworkers investigated the photoluminescence of tetracene layers deposited on crystalline Si both with and without a LiF spacer layer.[48] They concluded that a distance-dependent energy transfer mechanism, possibly mediated by surface plasmons in the tetracene layer, resulted in strong luminescence quenching. While most of their results concerned amorphous tetracene layers grown on low-temperature substrates, quenching was also observed for crystalline tetracene layers grown on room temperature substrates. However, that work left many unanswered questions, including an anomalous dependence on tetracene layer thickness and an apparent lack of change in the fluorescence lifetime. Given the interest in harvesting the triplet excitons produced by SF, we decided to revisit the tetracene-Si system to gain an improved understanding of the fluorescence quenching mechanism. In this chapter, we report the results of experiments on polycrystalline tetracene layers deposited onto a clean hydrogen-terminated Si 100 crystal, with and without a variable thickness LiF spacer layer. We look at how both the steady-state and time-resolved photoluminescence

signals change as a function of LiF spacer layer thickness. Because tetracene exhibits prompt fluorescence (due to the decay of the initially excited singlets) and delayed fluorescence (due to triplet-triplet fusion back into a singlet), the dynamics of both singlet and triplet excitons can be monitored in a singlet, time-resolved photoluminescence experiment. We find that the fluorescence changes can be explained by singlet energy transfer to the Si, combined with dielectric effects that affect the ability of the fluorescence to escape the sample. We find no evidence of triplet exciton quenching by the Si. Our results highlight the complexities of hybrid organic-inorganic materials and suggest that transferring excitons between the two phases may require new chemical approaches.

6.2 Results and Discussion

Both LiF and tetracene were deposited on a clean Si substrate using thermal evaporation under high vacuum. Figure 6.1 shows AFM images of a bare Si 100 surface before and after deposition of tetracene layers with nominal thicknesses of 3 and 27 nm. It is clear that the tetracene does not form a uniform coating, but instead forms islands distributed across the surface. This type of island growth has been observed previously for vacuum deposited tetracene[111,133] and is commonly seen for conjugated organic molecules that crystallize easily and have high surface mobility at room temperature. We chose to do most of our luminescence experiments with a tetracene

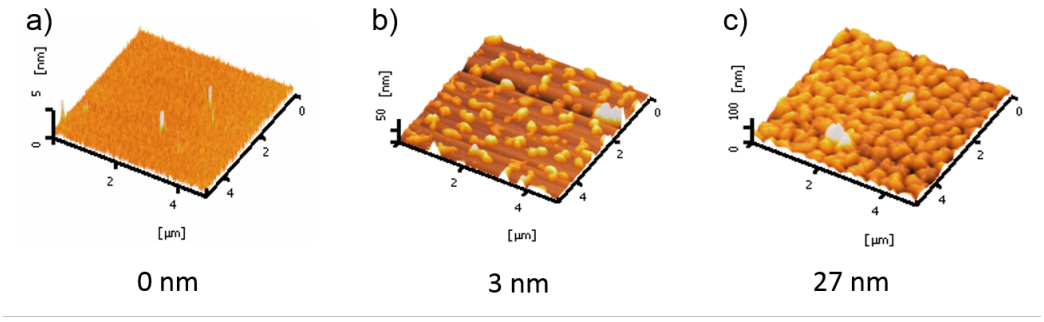

Figure 6.1: AFM images of the tetracene/Si surface for thicknesses of (a) 0 nm, (b) 3 nm, and (c) 27 nm. For thinner layers of tetracene, uniform coverage is not achieved due to island formation.

thickness of 27 nm since the AFM images show that this thickness provides a reasonably even surface coverage. It should be emphasized, however, that the film itself is not a perfectly homogeneous layer and is quite bumpy on nanometer lengthscales.

The crystalline nature of the tetracene islands is confirmed by the fluorescence lineshapes shown in Figure 6.2a. For LiF buffer layer thicknesses of 0, 5 and 10 and 35 nm, the fluorescence lineshape has the characteristic features of polycrystalline tetracene, with an enhanced 0-0 peak at 535 nm and a 0-1 vibronic replica at 550 nm. The roughly 3:1 ratio of the two peak intensities is characteristic of the delocalized singlet exciton that has been previously observed in ultrathin tetracene films and crystals.[67,68,134] The time-resolved fluorescence decays of tetracene on Si samples are also qualitatively similar to those observed for tetracene on inert substrates like glass. The set of data shown in Figure 6.2b is typical, with a prompt fluorescence decay on the order of 80-250 ps followed by a much longer delayed fluorescence with a lifetime on the order of 200 ns. To fit the entire fluorescence decay, including in-

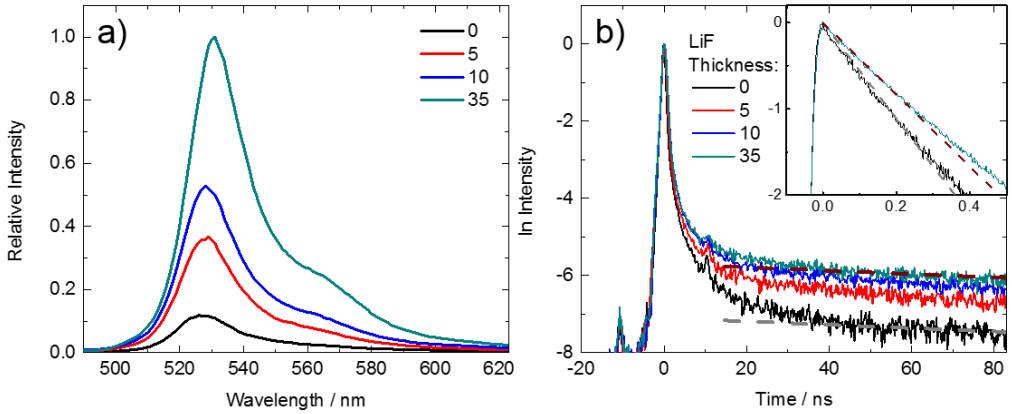

Figure 6.2: (a) Steady state photoluminescence of tetracene on Si with variable thickness (0, 5, 10, 35 nm) LiF spacer layers. (b) Time-resolved photoluminescence of tetracene on Si with variable thickness (0, 5, 10, 35 nm) LiF spacer layers in 100 ns time window, showing prompt and delayed fluorescence. Straight lines indicate single exponential fits to the delayed fluorescence component (τ_2) for 0 and 35 nm LiF thickness layers. Inset: Initial decay of prompt fluorescence signal for 0 and 35 nm LiF thickness layers. Dashed lines indicate a single exponential functions with $\tau = 0.18$ and 0.24 ns respectively.

termediate timescales, at least three exponential functions would be required.[24] In order to simplify our analysis, we concentrate only on the two separate time domains. The prompt fluorescence (reflecting the singlet lifetime) is characterized by τ_1 and the delayed fluorescence (proportional to the triplet lifetime) is characterized by τ_2. These two time constants can be thought of as parameterizing the data on very short timescales (< 1 ns) and very long timescales (> 100 ns). The two decays generated by τ_1 and τ_2 are shown as straight lines overlaid with the appropriate data ranges in Figure 6.2b.

Figure 6.3a shows the variation in the integrated steady-state fluorescence intensity as a function of LiF spacer layer thickness d_{LiF}. Also shown are data points for 5 nm thick crystalline tetracene on a p-doped Si crystal (orientation not specified),

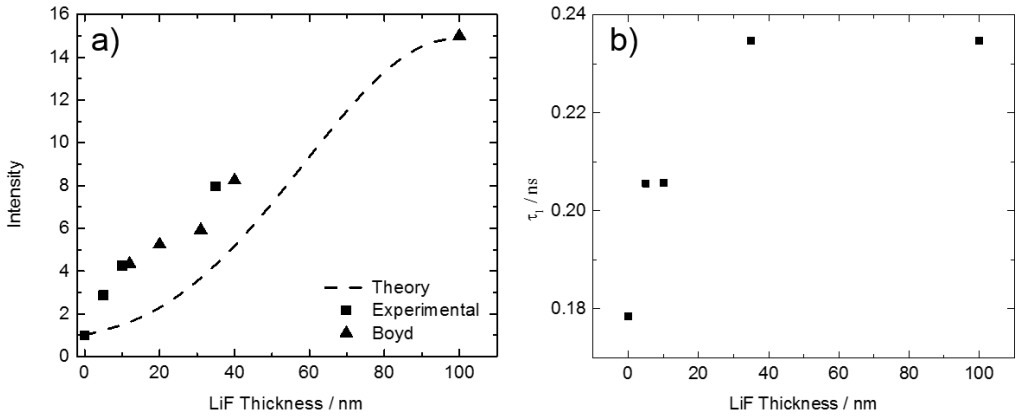

Figure 6.3: (a) Integrated steady-state photoluminescence intensity for various LiF thicknesses. Data from this Chapter (squares), Boyd et al.[48] (triangles) and the calculated signal based on both dielectric effects and the prompt fluorescence decay time data in (b). (b) The τ_1 decay time of the prompt fluorescence for various LiF thicknesses.

taken from the paper by Boyd and coworkers.[48] There is good agreement between the two sets of data, despite the use of different types of Si substrates. The present set of experiments also measure the τ_1 and τ_2 fluorescence decay times. Figure 6.3b shows that τ_1 lengthens by about 30% as the LiF thickness d_{LiF} increases, while the τ_2 values remain constant. The τ_2 values do not depend on d_{LiF} to within our experimental error. Finally, we note that the fluorescence decays were measured for at least three different coating runs of tetracene on Si. The same trends in τ_1 and τ_2 were observed for all sets of samples, despite some variability (10-20%) in the absolute τ_1 and τ_2 values. Experiments on p-doped Si yielded the same trends as well.

It is tempting to assign the shortened τ_1 value for the thinner LiF layers to an interaction with the Si, e.g. more rapid energy transfer from the tetracene S_1 state into the Si. To see if our kinetic data are consistent with such a scenario, we take a

simplified model of the S_1 and T_1 kinetics:

$$\frac{dN_{S_1}}{dt} = -(k_{fis} + k_{rad} + k_q)N_{S_1} + k_{fus}N_{2T_1} \tag{6.1}$$

$$\frac{dN_{2T_1}}{dt} = k_{fis}N_{S_1} - (k_{fus} + k_{trip})N_{2T_1} \tag{6.2}$$

where $k_{rad} = 0.08\,\mathrm{ns}^{-1}$ is the radiative decay rate,[125] $k_{fis} = 5$ ns-1 is the SF rate, $k_{fus} = 0.01$ ns^{-1} is the fusion rate, and k_{trip} =0.005 ns^{-1} is the triplet relaxation rate. These rates are consistent with our previous modeling of tetracene thin films and single crystals and reproduce the asymptotic τ_1 and τ_2 decay times as well as the relative amplitudes of the prompt and delayed fluorescence.[25,69] k_q is the non-radiative decay term due to the presence of the Si that varies with d_{LiF}. Note that $\frac{1}{\tau_1} = k_{rad} + k_{fis} + k_q$. We should also note that equations 6.1 and 6.2 describe the low intensity limit where the delayed fluorescence is dominated by recombination of geminate triplet pairs,[32] and do not take separation and diffusion of the pairs into account.[26] Figure 6.4a shows the calculated N_{S_1} fluorescence decays as k_q changes from 0 (thick LiF with $\tau_1 = 0.24$ ns) to 1.3 ns^{-1} (no LiF, τ_1= 0.18 ns). As expected, the prompt fluorescence decay time decreases as k_q increases. Using these parameters, Figure 6.4b shows that the delayed fluorescence decay rate remains almost constant, while its relative amplitude decreases since the competing k_q decay channel reduces the number of triplets produced by SF. In theory, the k_q loss channel can also accelerate the decay of the delayed fluorescence if k_{fus} is sufficiently rapid. But the relatively

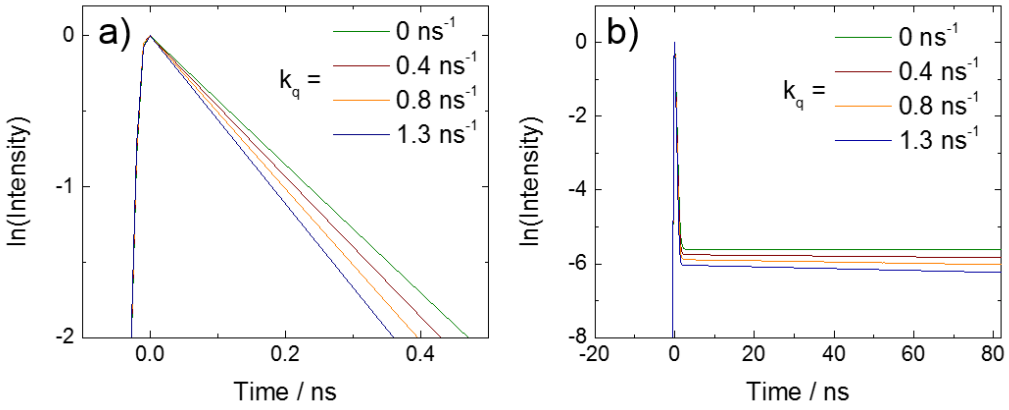

Figure 6.4: (a) Simulated fluorescence decays calculated using Eqs. (1) and (2) with the parameters k_{rad} = 0.08 ns^{-1}, k_{fiss}= 4.2 ns^{-1}, k_{fus} = 0.01 ns^{-1}, k_{trip} = 0.005 ns^{-1} and different values of k_q. The presence of the k_q terms leads to more rapid decay in the prompt fluorescence (a) and reduces the relative amplitude of delayed fluorescence (b).

slow fusion rate (k_{fus} = 0.01 ns^{-1}) used in our calculations means that the triplets only fuse every 100 ns, on average, which is comparable to their intrinsic lifetime in these thin films (200 ns), and k_q never has the chance to remove significant triplet population. The other possible triplet loss channel would be direct quenching by the Si, which should be reflected in the decay of the delayed fluorescence. The fact that the decay rate of the delayed fluorescence is unchanged even for d_{LiF} = 0 suggests that any triplet quenching by the Si must occur on timescales slower than 200 ns. In the limit of slow fusion, our calculated fluorescence signals do a reasonable job of reproducing the qualitative features of the decays on both short and long timescales using only the k_q singlet decay channel.

Although we can extract k_q values for varying LiF thicknesses from our data, we have not attempted to analyze them in terms of a specific model for singlet energy

transfer. Sokolowski and coworkers have investigated the fluorescence quenching of tetracene on alumina-coated Ni_3Al surfaces and suggested that both charge transfer and Forster-type energy transfer could be operative, depending on molecular orientation.[135,136] Danos et al. used variable thickness Langmuir-Blodgett films to estimate a Forster radius on the order of 5.5 nm for a cyanine dye monolayer on Si.[137] This distance is consistent with our observation that $\sim 50\%$ of the change in τ_1 occurs for d_{LiF} = 5-10 nm. In our experiments, because the thickness of our tetracene layers is large relative to the transfer distance, a quantitative analysis would require additional assumptions about singlet and triplet exciton diffusion within the tetracene layer, as well as other unknown factors that would lead to large uncertainties in any model parameters. For now, we leave a more detailed analysis for future studies on a simpler organic system.

Despite our success in modeling the fluorescence decay in terms of a distance-dependent k_q, the question remains as to why the steady-state fluorescence signal changes so dramatically, given the relatively small lifetime changes. Comparing Figures 6.3a and 6.3b, it is apparent that the small ($\sim 30\%$) change in τ_1 is not enough to account for the large change in the integrated fluorescence signal. In order to explain the observed fluorescence quenching, Boyd and coworkers proposed that an unspecified surface wave in the tetracene film couples energy into the Si substrate.[48] We have tried to make this idea more concrete by calculating the emission properties of a dipole sitting on top of a dielectric layer on top of bulk Si. The high index of the

Si is expected to yield a distance-dependent evanescent coupling of the emission into the Si substrate. Note that the calculation of the far-field emission pattern is separate from the kinetic equations described in the previous paragraph. This calculation takes into account the propagation of light after it is emitted from the tetracene molecule, whose nonradiative quenching is taken into account by Equations 6.1 and 6.2. Thus these effects will affect the intensity of the emission that escapes the sample, but do not affect the dynamics of the fluorescence decay. There is no simple analytical expression that describes these dielctric effects, so we numerically calculate the far-field emission pattern of the dipole using Crawfords formalism[138,139] for a 3-layer system (air, n_1= 1.0; LiF, n_2= 1.39; Si, n_3 = 11 + .25i[140]), where the emitting dipole is placed at the interface between layers 1 and 2 and the far-field emission profile is calculated using Equations 3 and 4 from reference.[138] We further assume that the dipoles are randomly oriented in the x-y plane, which means that the **ab** plane of the tetracene crystal is parallel to the substrate. This is the growth mode of tetracene on a variety of surfaces,[121,141] including hydrogen-terminated Si.[142] We calculated emission profiles F(d_{LiF},θ) where θ is the angle from the substrate, for various d_{LiF} values. Some example profiles, calculated for an emission wavelength of 550 nm, are shown in Figure 6.5 for different values of d_{LiF}. We find that as d_{LiF} increases, the evanescent coupling of the dipole radiation into the Si decreases and more radiation can escape into the n_1 air layer above the sample, where it can be detected.

If we combine the effects of changing both τ_1 and the radiative coupling of the

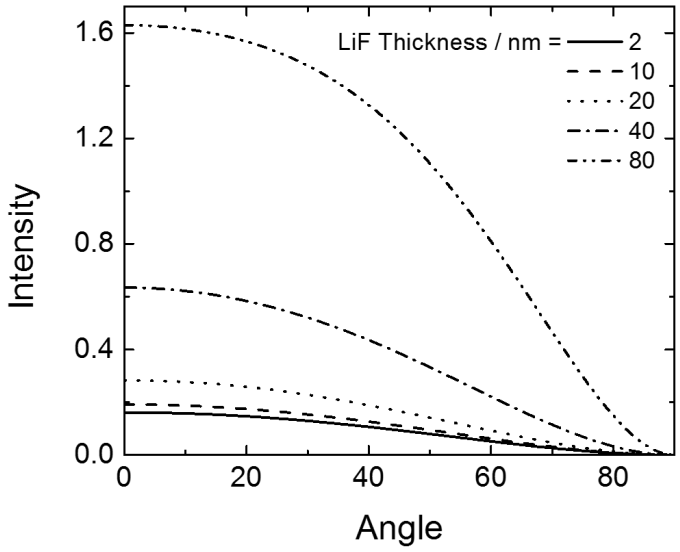

Figure 6.5: Angular dependence of the steady-state emission profile of a single dipole, oriented in the xy plane parallel to the Si substrate, for varying LiF buffer layer thicknesses. The curves are calculated using the methods outlined in Crawford's paper.[138] We assume that the detected luminescence intensity is proportional to the signal at $\theta = 0^{\circ}$ (emission normal to the surface).

dipole emission into the Si, we can calculate how the steady-state (integrated over time) emission signal should change with d_{LiF}. We assume that the detected fluorescence is proportional to $\tau_1 x F(d_{LiF}, \theta{=}0^\circ)$. This calculated curve is overlaid with the data in Figure 6.3a. The overall increase in fluorescence intensity is well-described for $d_{LiF} < 100$ nm, but the experimental points deviate from the calculated curve. In particular, the rapid increase at small d_{LiF} values is not well-reproduced by the calculation. This discrepancy may arise from the simplifying assumptions used in our calculations. First of all, a 27 nm thick tetracene film is likely not well approximated by a single dipole layer. Second, the irregular surface of the tetracene film (Figures 6.1b and 6.1c) may lead to scattering and degrade interference effects that affect the shape of the emission curves shown in Figure 6.5. Nevertheless, the fact that the calculation reproduces the overall change in luminescence intensity strongly suggests that dielectric coupling to the Si must be taken into account to quantitatively understand the increase in steady state luminescence intensity with increasing d_{LiF}.

One curious aspect of our results is that all our τ_1 values are significantly longer than the prompt fluorescence decay times for polycrystalline tetracene on glass, a non-quenching substrate, which range from 30-90 ps in the literature.[24,66–68,75]To further explore the factors that determine τ_1, we decided to examine the dynamics of variable thickness tetracene layers deposited directly onto Si without a LiF buffer layer. If exciton quenching by the Si was the only factor, we would expect the fluorescence decay to lengthen as the tetracene thickness d_{tet} increased and the average distance

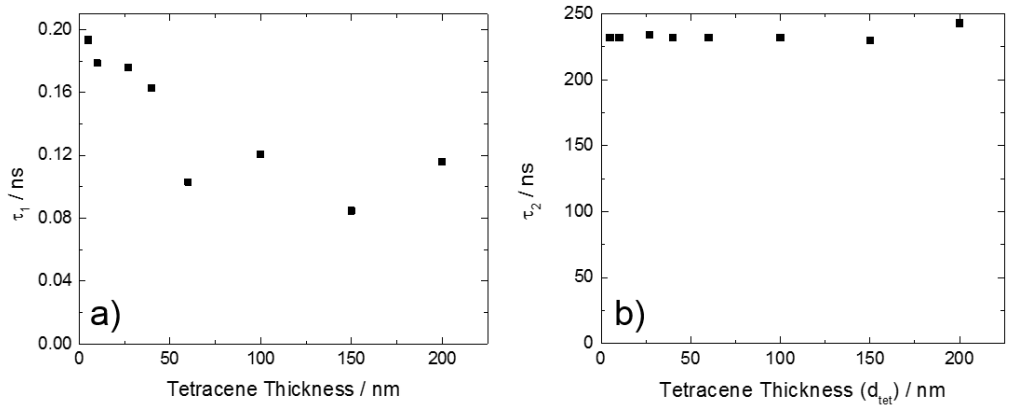

Figure 6.6: (a) The τ_1 decay time of the prompt fluorescence (1 ns window) for various tetracene thicknesses without a LiF spacer layer. (b) The τ_2 decay time of the delayed fluorescence (100 ns window) for various tetracene thicknesses without a LiF spacer layer.

to the Si interface increased. Surprisingly, τ_1 actually decreased as d_{tet} increased, as shown in Figure 6.6a, while τ_2 did not change at all (Figure 6.6b) On bare Si, τ_1 decreased from 180 ps to $\sim$ 90 ps, which is the value we have previously measured for tetracene films on glass.[24] This result cannot be easily rationalized in terms of a quenching process mediated by the Si. In order to explain the anomalous dependence of τ_1 on d_{tet}, as well as the longer τ_1 on LiF as compared to glass, we must consider how the SF rate depends on the solid-state morphology. Although in pentacene it has been claimed that SF occurs only in single crystals,[74] more recent results have shown that SF occurs very rapidly in polycrystalline films.[28,143] In tetracene as well, the single decay is faster by at least a factor of 2 in polycrystalline films.[27] If we consider that very thin films of tetracene (< 10 nm) actually consist of isolated single crystals, then the longer lifetimes for thin films on Si make sense: as the nominal tetracene thickness increases, we transition from a collection of single crystals to a

polycrystalline film. On LiF, a different substrate, we hypothesize that the 27 nm tetracene film behaves more like a single crystal, as evidenced by its relatively long τ_1 at large d_{LiF} values. In fact, we found that when different thicknesses of tetracene were deposited on a 100 nm thick LiF layer, the τ_1 value remained constant at its single crystal value of 240 ps irrespective of thickness. We should emphasize that the different thickness dependences of τ_1 for tetracene Si versus LiF is not fully understood. It is possible that the different substrates lead to different growth modes, but proving this will require additional experiments to characterize the film morphology.

6.3 Conclusion

In this chapter, we have revisited the experiments of Boyd and coworkers that examined the fluorescence of tetracene deposited on Si with variable thickness LiF buffer layers. We find the distance-dependent fluorescence quenching is dominated by dielectric effects, with a small ($\sim$30%) increase in the prompt fluorescence decay time for thicker LiF spacers that can be attributed to singlet energy transfer to the Si. A counterintuitive change in the prompt fluorescence lifetime as the tetracene thickness is increased on top of bare Si is interpreted in terms of crystallinity changes, where thicker tetracene layers act like polycrystalline films with more rapid SF rates which was observed in chapter 5 where the differences between single crystal and polycrystalline tetracene were studied. No clear evidence for triplet energy transfer to the Si is found. We should emphasize that any conclusions about morphology based on

fluorescence measurements are tentative, and an obvious next step is to characterize the structure of the organic layers in more detail, for example using scanning probe microscopy or electron and x-ray diffraction. More sophisticated modeling of the multilayer dielectric system would also be helpful to gain a quantitative understanding of the luminescence output. A combination of surface characterization techniques and optical measurements will be required to determine the ultimate fate of excitons at the organic-inorganic semiconductor interface.

Chapter 7

Conclusions

7.1 Summary and conclusions

To obtain the necessary efficiencies for solar light harvesting, new technological advances in the area are needed. Singlet fission was shown to exist in the three organic systems of tetracene, rubrene, and diphenylhexatriene. Methods of studying the phenomenon through luminescence and magnetic fields were presented to better understand how the process works so that it may be applied to device applications.

In Chapter 3, the effects of a magnetic field on the singlet fission system were explained and the Merrifield kinetic models were advanced. The results coming from these models showed that understanding the spin aspect of singlet fission and the diffusive nature of the triplets will be important for further study. The magnetic field effects show that the triplet pair can have singlet character and that the singlet

character of a triplet pair is important for the reverse process of triplet fusion. Understanding this is integral for understanding how singlet fission works from a spin viewpoint.

Chapter 4 detailed how the theory presented in Chapter 3 can be applied to the three different systems of tetracene, rubrene, and diphenylhexatriene. In tetracene, we were able to model the magnetic field effect on a single crystal and a polycrystalline film. Theory corroborated the results seen the in the time-resolved fluorescence data of tetracene single crystals where the magnetic field was used to change the presence of oscillations within the fluorescence decay. The three oscillation frequencies were reduced to one oscillation frequency as a magnetic field was applied as a result of going from three triplet pair states with singlet character to two triplet pair states with singlet character. Theory matched experiment quantitatively as we studied the affect of the angle of the applied magnetic field on the **ab** plane of the crystal which altered the frequency of the oscillation seen in the fluorescence decay. The Merrifield kinetic model was also expanded by including spatially separated pairs and spin-lattice relaxation into the model which allowed for a better description of the early time kinetics. We calculated the singlet character for random orientations of molecules in the case of amorphous rubrene. This allowed us to interpret the data we saw in experiment and come to the conclusion that singlet fission is most likely coming from ordered pairs and not random orientations. For diphenylhexatriene, the affect of the magnetic field on parallel molecules was studied and and the kinetic model developed for tetracene

was used. We found the traditional transition from 3 triplet pair states with singlet character to 2 triplet pair states with singlet character. It was also found that we needed to reduce the spin-lattice relaxation rate by a factor of 10 in the presence of a magnetic field to better fit the data. While progress was made in discovering a model which fit the data more quantitatively, more work is needed in describing the diffusive nature of the triplets to better fit the experiment fluorescence decays.

After doing these experiments, it was noticed that it may be possible that even if singlet fission occurs, there may not be a magnetic field effect on rate of the fluorescence decay, but only the frequency of the oscillations. In single crystal tetracene, it is known that the excited singlet state fissions into the triplet pair superposition of $\frac{1}{\sqrt{3}}(|xx\rangle + |yy\rangle + |zz\rangle)$ which is a singlet state and therefore has a $|C_S^l|^2$ value of 1. At high field, we also see the presence of the oscillations which are due to the superposition state of $\frac{1}{\sqrt{3}}(|00\rangle - |T_+T_-\rangle - |T_-T_+\rangle)$ which also has a $|C_S^l|^2$ value of 1 since it is a singlet state. Therefore, before the superposition decoheres, there should be no magnetic field effect in single crystal tetracene as you go from one state with $|C_S^l|^2 = 1$ to 1 state at high field with $|C_S^l|^2 = 1$. In this way, you would only see a change in the oscillation frequency, but the average rate of triplet-triplet annihilation should be the same. It would be a fairly simple test to see if this holds true and would be a useful check to ensure the oscillations and the magnetic field effects arise from the parameters we think they do.

In Chapter 5 we discovered that there are qualitative differences between the sin-

glet fission behavior in polycrystalline tetracene and single crystal tetracene. Polycrystalline tetracene had a measured singlet fission time of 70 ps while the single crystal tetracene had a fission time of 170 ps. The singlet fission rate in the single crystal was found to be thermally activated while the polycrystalline samples displayed very weak temperature dependent behavior. When a polycrystalline tetracene film is annealed, the single crystal singlet fission properties are recovered. Polarized light microscopy images showed that annealing the film increased the crystal grain sizes within the film, more closely matching the single crystal size. The differences in fluorescence dynamics between the two systems can be ascribed to singlet excitons diffusing either to grain boundaries or defects in the polycrystalline film where the local geometry between two chromophores could be more preferential for singlet fission. Annealing the film removes these defects and/or creates larger areas of bulk crystal for the excitons to diffuse through. The energy of some singlet fission intermediate state may also be lowered at these locations which would result in this lack of activation energy in the polycrystalline case. Also there were large variations in the fluorescence dynamics between the single crystals themselves which could be attributed to defects or impurities within the crystals.

It would be useful to confirm this hypothesis with further experiments. Careful evaporation and annealing techniques followed by characterization of the film would allow us to monitor the singlet fission rate as a function of the crystal grain size. Single crystal to single crystal variations could be analyzed by fluorescence and atomic

force microscopy to find a correlation between crystal defects and fluorescence rates and give a better idea of how defects affect singlet fission in the solid state and to get an idea of how to manipulate these defects for our benefit. For fundamental studies of singlet fission in tetracene, a preparation which yields reproducible single crystals needs to be discovered. As of now, the drop cast method out of saturated toluene shows a high variation in the quality of crystal for meaningful results to be taken from the experiments done on them, especially when it comes to the 'quantum beating' behavior exhibited by some single crystals of tetracene.

Finally, in Chapter 6, evaporated thin films of tetracene on n-type Si were studied to investigate triplet energy transfer from the tetracene to Si. Distance dependent fluorescence quenching was observed as there was a $\sim$30% increase in the prompt fluorescence time as we increased the thickness of a LiF blocker layer. This quenching was attributed to the singlet energy transfer from the tetracene to Si. There was a counterintuitive change in the prompt fluorescence lifetime as the tetracene thickness was increased on bare Si, but this could potentially be explained by the work shown in Chapter 5, where it was shown that variables such as the crystal grain size of a polycrystalline film could alter the singlet fission rate.

While energy transfer of triplet excitons into silicon should be energetically possible, it may be possible that geometry of the system was prohibitive for a Dexter type non-radiative energy transfer which requires wavefunction overlap.[144] Triplets would generally transfer through this mechanism as it would allow the triplet state

tetracene to reach a ground state singlet while still conserving spin. A study done by Tersigni et al. shows that tetracene tends to stand up on the surface of H-terminated Si with the long axis of tetracene normal to the Si surface.[142] If this were the case in our samples, the bulk of the π system would not be interacting with the surface and would make it difficult for Dexter transfer to occur. Work should be done to find molecules to passivate Si with that would allow tetracene to lay flat on the surface to enable greater interaction between the two materials.

In this dissertation, new kinetic models have been developed to better understand the dynamics of singlet fission systems. These kinetic models help build a physical picture of singlet fission dynamics for systems with varying geometries and give us a better idea of the spin characteristics and diffusive nature of the triplet states after the singlet fission event. In the case of tetracene and most likely other molecules, variations in the crystal packing structure in the form of defects can play a role in determining singlet fission efficiency and triplet-triplet annihilation dynamics and therefore we know now that crystal quality is also an important factor in determining what makes a good singlet fission material. We have yet to see how the interfacial geometry between SF materials and inorganic semiconductors plays a role in photovoltaic devices, but SF remains a promising avenue for advanced solar cell applications.

Bibliography

[1] K. N. Liou. *Introduction to Atmospheric Radiation (2nd Edition)*. Elsevier, 2002.

[2] Energy Information Administration. Int. Energy Stat., 2013.

[3] William Shockley and Hans J. Queisser. *J. Appl. Phys.*, 32(3):510, 1961.

[4] Zhiyuan Huang, Xin Li, Benjamin D. Yip, Justin M. Rubalcava, Christopher J. Bardeen, and Ming L. Tang. *Chem. Mater.*, 27(21):7503–7507, nov 2015.

[5] Zhiyuan Huang, Duane E. Simpson, Melika Mahboub, Xin Li, and Ming L. Tang. *Chem. Sci.*, 2016.

[6] Geoffrey B. Piland, Zhiyuan Huang, Ming Lee Tang, and Christopher J. Bardeen. *J. Phys. Chem. C*, 120(11):5883–5889, mar 2016.

[7] Keisuke Okumura, Kazuma Mase, Nobuhiro Yanai, and Nobuo Kimizuka. *Chem. - A Eur. J.*, 22(23):7721–7726, jun 2016.

[8] René T. Wegh, Harry Donker, Koenraad D. Oskam, Andries Meijerink, C. R. Ronda, F. Vollkommer, L. Hitzschke, A. W. de Jager, D. A. Doughty, W. W. Beers, R. Pappalardo, F. Auzel, R. T. Wegh, H. Donker, A. Meijerink, R. J. Lamminmäki, J. Hölsä, J. P. M. van Vliet, D. van der Voort, G. Blasse, C. Görller-Walrand, K. Binnemans, and L. Fluyt. *Science*, 283(5402):663–6, jan 1999.

[9] De-Chao Yu, Rosa Martín-Rodríguez, Qin-Yuan Zhang, Andries Meijerink, and Freddy T Rabouw. *Light Sci. Appl.*, 4(10):e344, oct 2015.

[10] Arthur J. Nozik. *Chem. Phys. Lett.*, 457(1):3–11, 2008.

[11] Millicent B Smith and Josef Michl. *Chem. Rev.*, 110(11):6891–6936, 2010.

[12] Millicent B Smith and Josef. Michl. *Annu. Rev. Phys. Chem.*, 64:361–386, 2013.

[13] M C Hanna and A J Nozik. *J. Appl. Phys.*, 100(7):074510/1–074510/8, 2006.

[14] S. Singh, W. J. Jones, W. Siebrand, B. P. Stoicheff, and W. G. Schneider. *J. Chem. Phys.*, 42(1):330, 1965.

[15] R. C. Johnson, R. E. Merrifield, P. Avakian, and R. B. Flippen. *Phys. Rev. Lett.*, 19(6):285–287, aug 1967.

[16] R.C. Johnson and R.E. Merrifield. *Phys. Rev. B*, 1:896–902, 1970.

[17] R.E. Merrifield, P. Avakian, and R.P. Groff. *Chem. Phys. Lett.*, 3(3):155–157, mar 1969.

[18] Nicholas Geacintov, Martin Pope, F. Vogel, and Frank E Vogel III. *Phys. Rev. Lett.*, 22(12):593–596, mar 1969.

[19] C.E. Swenberg and W.T. Stacy. *Chem. Phys. Lett.*, 2(5):327–328, sep 1968.

[20] Y. Tomkiewicz, R. P. Groff, and P. Avakian. *J. Chem. Phys.*, 54(10):4504, 1971.

[21] Martin Pope, Nicholas E. Geacintov, and Frank Vogel. *Mol. Cryst.*, 6(1):83–104, aug 1969.

[22] Mark W B Wilson, Akshay Rao, Kerr Johnson, Simon Glinas, Riccardo Di Pietro, Jenny Clark, and Richard H. Friend. *J. Am. Chem. Soc.*, 135(44):16680–16688, 2013.

[23] Wai-Lun Chan, Manuel Ligges, and X-Y. Zhu. *Nat. Chem.*, 4(10):840–845, 2012.

[24] Jonathan J Burdett, David Gosztola, and Christopher J Bardeen. *J. Chem. Phys.*, 135(21):214508/1–214508/10, 2011.

[25] Jonathan J Burdett and Christopher J Bardeen. *J. Am. Chem. Soc.*, 134(20):8597–607, may 2012.

[26] Jonathan J Burdett, Geoffrey B Piland, and Christopher J Bardeen. *Chem. Phys. Lett.*, 585:1–10, 2013.

[27] Jonathan J Burdett and Christopher J Bardeen. *Acc. Chem. Res.*, 46(6):1312–1320, 2013.

[28] Mark W B Wilson, Akshay Rao, Jenny Clark, R Sai Santosh Kumar, Daniele Brida, Giulio Cerullo, and Richard H Friend. *J. Am. Chem. Soc.*, 133(31):11830–11833, 2011.

[29] Paul M. Zimmerman, Zhiyong Zhang, and Charles B. Musgrave. *Nat. Chem.*, 2(8):648–652, aug 2010.

[30] N.E. Geacintov, J. Burgos, M. Pope, and C. Strom. *Chem. Phys. Lett.*, 11(4):504–508, nov 1971.

[31] Nicholas J Thompson, Eric Hontz, Wendi Chang, Troy Van Voorhis, and Marc Baldo. *Philos. Trans. A. Math. Phys. Eng. Sci.*, 373(2044):20140323–, jun 2015.

[32] Geoffrey B. Piland, Jonathan J. Burdett, Dharmalingam Kurunthu, and Christopher J. Bardeen. *J. Phys. Chem. C*, 117(3):1224–1236, jan 2013.

[33] Sean T Roberts, R Eric McAnally, Joseph N Mastron, David H Webber, Matthew T Whited, Richard L Brutchey, Mark E Thompson, and Stephen E Bradforth. *J. Am. Chem. Soc.*, 134(14):6388–6400, 2012.

[34] Ivan Biaggio and Pavel Irkhin. *Appl. Phys. Lett.*, 103(26):263301, dec 2013.

[35] Andrew J. Musser, Margherita Maiuri, Daniele Brida, Giulio Cerullo, Richard H. Friend, and Jenny Clark. *J. Am. Chem. Soc.*, 137(15):5130–5139, apr 2015.

[36] Chen Wang and Michael J. Tauber. *J. Am. Chem. Soc.*, 132(40):13988–13991, oct 2010.

[37] Chen Wang, Diana E. Schlamadinger, Varsha Desai, and Michael J. Tauber. *ChemPhysChem*, 12(16):2891–2894, nov 2011.

[38] Andrew J. Musser, Mohammed Al-Hashimi, Margherita Maiuri, Daniele Brida, Martin Heeney, Giulio Cerullo, Richard H. Friend, and Jenny Clark. *J. Am. Chem. Soc.*, 135(34):12747–12754, aug 2013.

[39] Joel N Schrauben, Joseph L Ryerson, Josef Michl, and Justin C Johnson. *J. Am. Chem. Soc.*, 136(20):7363–7373, 2014.

[40] Samuel W Eaton, Leah E Shoer, Steven D Karlen, Scott M Dyar, Eric A Margulies, Brad S Veldkamp, Charusheela Ramanan, Daniel A Hartzler, Sergei Savikhin, Tobin J Marks, and Michael R Wasielewski. *J. Am. Chem. Soc.*, 135(39):14701–14712, 2013.

[41] Tony C. Wu, Nicholas J. Thompson, Daniel N. Congreve, Eric Hontz, Shane R. Yost, Troy Van Voorhis, and Marc A. Baldo. *Appl. Phys. Lett.*, 104(19):193901, may 2014.

[42] Maxim Tabachnyk, Bruno Ehrler, Simon Gélinas, Marcus L. Böhm, Brian J. Walker, Kevin P. Musselman, Neil C. Greenham, Richard H. Friend, and Akshay Rao. *Nat. Mater.*, 13(11):1033–1038, oct 2014.

[43] Nicholas J. Thompson, Mark W. B. Wilson, Daniel N. Congreve, Patrick R. Brown, Jennifer M. Scherer, Thomas S. Bischof, Mengfei Wu, Nadav Geva, Matthew Welborn, Troy Van Voorhis, Vladimir Bulović, Moungi G. Bawendi, and Marc A. Baldo. *Nat. Mater.*, 13(11):1039–1043, oct 2014.

[44] M. Chabr, U.P. Wild, J. Fünfschilling, and I. Zschokke-Gränacher. *Chem. Phys.*, 57(3):425–430, may 1981.

[45] S Arnold. *J. Chem. Phys.*, 75(3):1166, 1981.

[46] Murad J Y Tayebjee, Raphaël G C R Clady, and Timothy W Schmidt. *Phys. Chem. Chem. Phys.*, 15(35):14797–805, 2013.

[47] D.L. Dexter. *J. Lumin.*, 18-19:779–784, jan 1979.

[48] T Hayashi, T G Castner, and Robert W Boyd. *Chem. Phys. Lett.*, 94(5):461–466, 1983.

[49] D Aureau, Y Varin, K Roodenko, O Seitz, O Pluchery, and Y J Chabal. *J. Phys. Chem. C*, 114(33):14180–14186, 2010.

[50] G S Higashi, Y J Chabal, G W Trucks, and Krishnan. Raghavachari. *Appl. Phys. Lett.*, 56(7):656–658, 1990.

[51] Tien-Lung Chiu, Wei-Fu Chang, Cheng-Che Wu, Chi-Feng Lin, Jiunn-Yih Lee, Shun-Wei Liu, Chin-Ti Chen, and Jiun-Haw. Lee. *J. Disp. Technol.*, 9(10):787–793, 2013.

[52] R.E. Merrifield. *J. Chem. Phys.*, 48:4318–4319, 1968.

[53] V.I. Lesin, A.I. Pristupa, and E.L. Frankevich. *Op. Spect.*, 51:477–480, 1981.

[54] S. M. Rumyantsev, V. I. Lesin, and E. L. Frankevich. *Opt. Spectrosc.*, 38:49–50, 1975.

[55] M. Pope and C.E. Swenberg. *Electronic Processes in Organic Crystals and Polymers*. Oxford University Press, New York, 1999.

[56] C E Swenberg and N E Geacintov. Exciton interactions in organic solids. In *Org. Mol. Photophysics, vol. 1*, pages 489–564. Wiley & Sons, Bristol, 1973.

[57] R. P. Groff, P. Avakian, and R. E. Merrifield. *Phys. Rev. B*, 1(2):815–817, jan 1970.

[58] H. Bouchriha, V. Ern, J.L. Fave, C. Guthmann, M. Schott, and M. Schott. *J. Phys.*, 39(3):257–271, 1978.

[59] E.L. Frankevich, A.I. Pristupa, and V.I. Lesin. *Chem. Phys. Lett.*, 47(2):304–308, apr 1977.

[60] A. Suna. *Phys. Rev. B1*, 1:1716, 1970.

[61] N.F. Berk. *Phys. Rev. B*, 18:4535, 1978.

[62] L. Hachani, A. Benfredj, S. Romdhane, M. Mejatty, J.L. Monge, and H. Bouchriha. *Phys. Rev. B*, 77:035212/1–035212/7, 2008.

[63] T. Barhoumi, J. L. Monge, M. Mejatty, and H. Bouchriha. *Eur. Phys. J. B*, 59(2):167–172, sep 2007.

[64] K.v. Burg, L. Altwegg, and I. Zschokke-Granacher. *Phys. Rev. B*, 22:2037–2049, 1980.

[65] L. Yarmus, J. Rosenthal, and M. Chopp. *Chem. Phys. Lett.*, 16:477–481, 1972.

[66] A Wappelt, A Bergmann, A Napiwotzki, H J Eichler, H J Jupner, A Kummrow, A Lau, and S Woggon. *J. Appl. Phys.*, 78(8):5192–5194, 1995.

[67] Sang-Hyun Lim, Thomas G Bjorklund, Frank C Spano, and Christopher J Bardeen. *Phys. Rev. Lett.*, 92(10):107402/1–107402/4, 2004.

[68] M Voigt, A Langner, P Schouwink, J M Lupton, R F Mahrt, and M Sokolowski. *J. Chem. Phys.*, 127(11):114705/1–114705/8, 2007.

[69] Jonathan J Burdett, Astrid M Muller, David Gosztola, and Christopher J Bardeen. *J. Chem. Phys.*, 133(14):144506, 2010.

[70] C. C. Gradinaru, J. T. M. Kennis, E. Papagiannakis, I. H. M. van Stokkum, R. J. Cogdell, G. R. Fleming, R. A. Niederman, and R. van Grondelle. *Proc. Natl. Acad. Sci.*, 98(5):2364–2369, feb 2001.

[71] Sadayuki Watanabe, Akihiro Furube, and Ryuzi Katoh. *J. Phys. Chem. A*, 110(34):10173–10178, aug 2006.

[72] G. Lanzani, G. Cerullo, M. Zavelani-Rossi, S. De Silvestri, Davide Comoretto, Gianfranco Musso, and Giovanna Dellepiane. *Phys. Rev. Lett.*, 87(18):187402, oct 2001.

[73] Jiamo Guo, Hideo Ohkita, Hiroaki Benten, and Shinzaburo Ito. *J. Am. Chem. Soc.*, 131(46):16869–16880, nov 2009.

[74] V K Thorsmolle, R D Averitt, J Demsar, D L Smith, S Tretiak, R L Martin, X Chi, B K Crone, A P Ramirez, and A J Taylor. *Phys. Rev. Lett.*, 102(1):017401/1–017401/4, 2009.

[75] Erik M Grumstrup, Justin C Johnson, and Niels H Damrauer. *Phys. Rev. Lett.*, 105(25):257403/1–257403/4, 2010.

[76] G. Peter and H. Bässler. *Chem. Phys.*, 49(1):9–16, jun 1980.

[77] S L.; Carmichael Murov I.; Hug, G.L. *Handbook of Photochemistry*. Marcel Dekker, Inc., New York, 2nd ed. edition, 1993.

[78] H. Najafov, B. Lee, Q. Zhou, L. C. Feldman, and V. Podzorov. *Nat. Mater.*, 9(11):938–943, nov 2010.

[79] Lin Ma, Keke Zhang, Christian Kloc, Handong Sun, Maria E Michel-Beyerle, and Gagik G Gurzadyan. *Phys. Chem. Chem. Phys.*, 14(23):8307–8312, 2012.

[80] V.V. Tarasov, G.E. Zorianiants, A.I. Shushin, and M.M. Triebel. *Chem. Phys. Lett.1*, 267:58–64, 1997.

[81] Pavel Irkhin and Ivan Biaggio. *Phys. Rev. Lett.*, 107(1):017402, jul 2011.

[82] Aleksandr Ryasnyanskiy and Ivan Biaggio. *Phys. Rev. B*, 84(19):193203, nov 2011.

[83] B. Stevens and B. E. Algar. *J. Phys. Chem.*, 72(7):2582–2587, jul 1968.

[84] W.G. Herkstroeter and P.B. Merkel. *J. Photochem.*, 16(4):331–341, 1981.

[85] F. Lewitzka and H. G. Lohmannsroben. *Zeit. Phys. Chem.*, 150:69–86, 1986.

[86] K. Lendi, P. Berber, and H. Labhart. *Chem. Phys.*, 18:449–468, 1976.

[87] K. Yokoyama, Y. Wakikawa, T. Miura, J. Fujimori, F. Ito, and T. Ikoma. *J. Phys. Chem. B*, 119:15901–15908, 2015.

[88] A.M. Muller, Y.S. Avlasevich, K Mullen, and C.J. Bardeen. *Chem. Phys. Lett.*, 421:518–522, 2006.

[89] A.M. Muller, Y.S. Avlasevich, W.W. Schoeller, K Mullen, and C.J. Bardeen. *J. Am. Chem. Soc.*, 129:14240–14250, 2007.

[90] J.M. Shim, K.V. Raman, Y.J. Park, T.S. Santos, G.X. Miao, B. Satpati, and J.S. Moodera. *Phys. Rev. Lett.*, 100:226603/1–226603/4, 2008.

[91] L. Altwegg. *Chem. Phys. Lett.*, 63:97–99, 1979.

[92] V.I. Lesin and V.P. Sakun. *Phys. Status Solidi B*, 98:411–417, 1980.

[93] D. Beljonne, H. Yamagata, J. L. Brédas, F. C. Spano, and Y. Olivier. *Phys. Rev. Lett.*, 110(22):226402, may 2013.

[94] Timothy C. Berkelbach, Mark S. Hybertsen, and David R. Reichman. *J. Chem. Phys.*, 138(11):114102, 2013.

[95] Eric C. Greyson, Brian R. Stepp, Xudong Chen, Andrew F. Schwerin, Irina Paci, Millicent B. Smith, Akin Akdag, Justin C. Johnson, Arthur J. Nozik, Josef Michl, and Mark A. Ratner. *J. Phys. Chem. B*, 114(45):14223–14232, nov 2010.

[96] Paul M. Zimmerman, Charles B. Musgrave, and Martin Head-Gordon. *Acc. Chem. Res.*, 46(6):1339–1347, jun 2013.

[97] Justin C. Johnson, Arthur J. Nozik, and Josef Michl. *Acc. Chem. Res.*, 46:1290–1299, 2013.

[98] K. Aryanpour, J. A. Muñoz, and S. Mazumdar. *J. Phys. Chem. C*, 117(10):4971–4979, 2013.

[99] Charusheela Ramanan, Amanda L Smeigh, John E Anthony, Tobin J Marks, and Michael R Wasielewski. *J. Am. Chem. Soc.*, 134(1):386–397, 2012.

[100] Wai Lun Chan, Timothy C. Berkelbach, Makenzie R. Provorse, Nicholas R. Monahan, John R. Tritsch, Mark S. Hybertsen, David R. Reichman, Jiali Gao, and X. Y. Zhu. The quantum coherent mechanism for singlet fission: Experiment and theory, 2013.

[101] Jun Harada, Mayuko Harakawa, Keiichiro Ogawa, A. Gavezzotti, M. Simonetta, K. D. M. Harris, A. E. Aliev, H. B. Bürgi, J. Harada, K. Ogawa, S. Tomoda, J. Harada, K. Ogawa, J. Harada, K. Ogawa, J. Harada, M. Harakawa, K. Ogawa, J. Harada, K. Ogawa, S. Galli, P. Mercandelli, A. Sironi, N. A. Murugan, S. Yashonath, J. Harada, H. Uekusa, Y. Ohashi, Y. Ito, H. Hosomi, S. Ohba, S. Ohba, H. Hosomi, Y. Ito, Q. Chu, D. C. Swenson, L. R. MacGillivray, R. S. H. Liu, G. S. Hammond, R. S. H. Liu, L.-Y. Yang, J. Liu, G. M. Sheldrick, J. Hengstenberg, R. Kuhn, W. Drenth, E. H. Wiebenga, T. Hall, S. M. Bachrach, C. W. Spangler, L. S. Sapochak, C. T. Lin, H. W. Guan, and R. D. Rogers. *CrystEngComm*, 10(12):1777, 2008.

[102] J. Funfschilling, L. Altwegg, I. ZschokkeGranacher, M. Chabr, and D. F. Williams. *J. Chem. Phys.*, 70(10):4622, 1979.

[103] Zhi-Qiang You, Chao-Ping Hsu, and Graham R. Fleming. *J. Chem. Phys.*, 124(4):044506, 2006.

[104] A W Smith and C Weiss. *Chem. Phys. Lett.*, 14(4):507–511, 1972.

[105] R R Alfano, S L Shapiro, and M Pope. *Opt. Commun.*, 9(4):388–391, 1973.

[106] Ricardo Lopez-Delgado, Joseph A Miehe, and Bernard. Sipp. *Opt. Commun.*, 19(1):79–82, 1976.

[107] Graham R Fleming, David P Millar, Graeme C Morris, John M Morris, and G Wilse. Robinson. *Aust. J. Chem.*, 30(11):2353–2359, 1977.

[108] G Klein. *Chem. Phys. Lett.*, 57(2):202–206, 1978.

[109] Anatoly B Kolomeisky, Xintian Feng, and Anna I Krylov. *J. Phys. Chem. C*, 118(10):5188–5195, 2014.

[110] Takao Sakurai and Sohachiro Hayakawa. *Jpn. J. Appl. Phys.*, 13(11):1733–1740, 1974.

[111] W. Hofberger. *Phys. Status Solidi*, 30(1):271–278, 1975.

[112] Zephania Birech, Markus Schwoerer, Teresa Schmeiler, Jens Pflaum, and Heinrich. Schwoerer. *J. Chem. Phys.*, 140(11):114501/1–114501/9, 2014.

[113] Bo Zhang, Chunfeng Zhang, Yanqing Xu, Rui Wang, Bin He, Yunlong Liu, Shimeng Zhang, Xiaoyong Wang, and Min. Xiao. *J. Chem. Phys.*, 141(24):244303/1–244303/7, 2014.

[114] R Jankowiak, J Kalinowski, M Konys, and J Buchert. *Chem. Phys. Lett.*, 65(3):549–553, 1979.

[115] U. Sondermann, A. Kutoglu, and H. Bassler. *J. Phys. Chem.*, 89(9):1735–1741, 1985.

[116] Elisabetta Venuti, Raffaele Guido Della Valle, Luca Farina, Aldo Brillante, Matteo Masino, and Alberto. Girlando. *Phys. Rev. B Condens. Matter Mater. Phys.*, 70(10):104106/1–104106/8, 2004.

[117] P E Fielding and Richard C Jarnagin. *J. Chem. Phys.*, 47(1):247–252, 1967.

[118] Rumiko Horiguchi, Noriko Iwasaki, and Yusei. Maruyama. *J. Phys. Chem.*, 91(19):5135–5139, 1987.

[119] Tai-Sang Ahn, Astrid M Muller, Rabih O Al-Kaysi, Frank C Spano, Joseph E Norton, David Beljonne, Jean-Luc Bredas, and Christopher J Bardeen. *J. Chem. Phys.*, 128(5):054505/1–054505/11, 2008.

[120] Yu. P Piryatinskii and M V Kurik. *Mol. Cryst. Liq. Cryst. Sci. Technol. Sect. C Mol. Mater.*, 1(1):43–64, 1992.

[121] S. Milita, C. Santato, and F. Cicoira. *Appl. Surf. Sci.*, 252(22):8022–8027, 2006.

[122] B Gompf, D Faltermeier, C Redling, M Dressel, and J Pflaum. *Eur. Phys. J. E Soft Matter*, 27(4):421–424, 2008.

[123] G Vaubel and H. Baessler. *Mol. Cryst. Liq. Cryst.*, 12(1):47–56, 1970.

[124] A J Campillo, S I Shapiro, and C E Swenburg. *Chem. Phys. Lett.*, 52(1):11–15, 1977.

[125] S H Lim, T G Bjorklund, and C J Bardeen. *J. Phys. Chem. B*, 108:4289–4295, 2004.

[126] Brian J Walker, Andrew J Musser, David Beljonne, and Richard H Friend. *Nat. Chem.*, 5(12):1019–24, 2013.

[127] Kolja Kolata, Tobias Breuer, Gregor Witte, and Sangam. Chatterjee. *ACS Nano*, 8(7):7377–7383, 2014.

[128] Samuel W. Eaton, Stephen A. Miller, Eric A. Margulies, Leah E. Shoer, Richard D. Schaller, and Michael R. Wasielewski. *J. Phys. Chem. A*, 119(18):4151–4161, 2015.

[129] Valerie M Nichols, Marco T Rodriguez, Geoffrey B Piland, Fook Tham, Vladimir N Nesterov, W Justin Youngblood, and Christopher J Bardeen. *J. Phys. Chem. C*, 117(33):16802–16810, 2013.

[130] W G Albrecht, M E Michel-Beyerle, and V Yakhot. *Chem. Phys.*, 35(1-2):193–200, 1978.

[131] V M Agranovich, Yu. N Gartstein, and M Litinskaya. *Chem. Rev. (Washington, DC, United States)*, 111(9):5179–5214, 2011.

[132] Bruno Ehrler, Kevin P Musselman, Marcus L Boehm, Richard H Friend, and Neil C Greenham. *Appl. Phys. Lett.*, 101(15):153507/1–153507/3, 2012.

[133] Nicola Beaumont, Sang Wan Cho, Paul Sullivan, David Newby, Kevin E Smith, and Tim. S Jones. *Adv. Funct. Mater.*, 22(3):561–566, 2012.

[134] A Camposeo, M Polo, S Tavazzi, L Silvestri, P Spearman, R Cingolani, and D Pisignano. *Phys. Rev. B Condens. Matter Mater. Phys.*, 81(3):033306/1–033306/4, 2010.

[135] Andreas Langner, Yang Su, and Moritz. Sokolowski. *Phys. Rev. B Condens. Matter Mater. Phys.*, 74(4):045428/1–045428/11, 2006.

[136] M. Muller, A. Langer, O. Krylova, E.L. Moal, and M. Sokolowski. *Appl. Phys. B*, 105:67, 2011.

[137] Lefteris Danos and Tomas. Markvart. *Chem. Phys. Lett.*, 490(4-6):194–199, 2010.

[138] Oakley H Crawford. *J. Chem. Phys.*, 89(10):6017–6027, 1988.

[139] T. Kim, D. Kurunthu, J.J. Burdett, and C.J. Bardeen. *J. Appl. Phys.*, 108:033114, 2010.

[140] Hue M Nguyen, Oliver Seitz, Weina Peng, Yuri N Gartstein, Yves J Chabal, and Anton V Malko. *ACS Nano*, 6(6):5574–5582, 2012.

[141] P Syed Abthagir, Young-Geun Ha, Eun-Ah You, Seon-Hwa Jeong, Hoon-Seok Seo, and Jong-Ho. Choi. *J. Phys. Chem. B*, 109(50):23918–23924, 2005.

[142] A Tersigni, J Shi, D T Jiang, and X R Qin. *Phys. Rev. B Condens. Matter Mater. Phys.*, 74(20):205326/1–205326/9, 2006.

[143] Wai-Lun Chan, Manuel Ligges, Askat Jailaubekov, Loren Kaake, Luis Miaja-Avila, and X.-Y. Zhu. *Sci. (Washington, DC, United States)*, 334(6062):1541–1545, 2011.

[144] D. L. Dexter. *J. Chem. Phys.*, 21(5):836, 1953.